



Simon Prato

# Numerical Investigation of TEM Cells and Antenna Coupling

**Master Thesis**

Studies: Electrical Engineering

submitted to

**Graz University of Technology**

Supervisor

Dr. Thomas Bauernfeind



Graz, February 2025

## Abstract

Electrically small antennas that conduct high-frequency signals often generate substantial electromagnetic emissions, presenting challenges for electromagnetic compatibility. Measurement of these emissions in a TEM cell remains a widely adopted and standardized procedure. In this thesis, a comprehensive theoretical framework is developed to explain the coupling mechanisms between the antenna and the TEM cell. The proposed framework is further supported and examined through detailed numerical analyses.

In the context of these investigations, special focus is laid on electric and magnetic dipole moments, which effectively characterize electrically small radiating sources. The magnitudes of these dipole moments accurately describe the electric and magnetic coupling independently. While established measurement-based methods with the TEM cell for determining these magnitudes exists, this thesis focuses on leveraging the finite element method to eliminate potential inaccuracies arising from the measurement setup and procedure. Furthermore, this study examines near-field shielding of the antennas and their equivalent dipole moments to determine shielding efficiency of materials with different properties.

The findings presented in this thesis contribute to a deeper understanding of how the geometrical and electrical characteristics of antennas influence their coupling behavior and, consequently, the generated dipole moments. This proves useful, for example, when aiming to increase electromagnetic compatibility of an electronic system containing electrically small conducting structures. Additionally, it demonstrates how the determination of equivalent dipole moments assist in the choice of shielding material.

# Contents

<b>1</b>	<b>Introduction</b>	<b>1</b>
<b>2</b>	<b>Dipole Theory</b>	<b>2</b>
2.1	Electric Dipoles . . . . .	2
2.1.1	Infinitesimal Electric Dipoles . . . . .	2
2.1.2	Small Electric Dipoles . . . . .	5
2.2	Magnetic Dipoles . . . . .	6
2.3	Radiated Field . . . . .	7
2.3.1	Field regions . . . . .	8
2.3.2	Energy densities and reactances . . . . .	10
<b>3</b>	<b>Guided Waves</b>	<b>11</b>
3.1	Lorentz Reciprocity Theorem . . . . .	11
3.2	Green's Function . . . . .	12
3.2.1	Scalar Green's Function . . . . .	12
3.2.2	Dyadic Green's Function . . . . .	13
3.3	Modes in Waveguides . . . . .	15
3.3.1	Rectangular Waveguides as non-TEM structures . . . . .	15
3.4	TEM mode in the TEM cell . . . . .	16
3.4.1	Higher-order modes . . . . .	18
3.4.2	Field distributions . . . . .	20
3.5	Radiating Sources in TEM Cells . . . . .	24
3.5.1	Arbitrary source . . . . .	24
3.5.2	Equivalent dipole moments . . . . .	26
3.5.3	Electrically small antennas . . . . .	28
3.6	Shielding . . . . .	30
3.6.1	Electromagnetic shielding mechanisms . . . . .	30
3.6.2	Conductivity, permeability and permittivity in shields . . . . .	32
3.6.3	Skin Effect . . . . .	33
3.6.4	ASTM ES7-83 Method . . . . .	33
3.6.5	Dual TEM cell . . . . .	34
<b>4</b>	<b>Finite Element Method</b>	<b>35</b>
4.1	General Idea . . . . .	35
4.2	Dividing a computational domain into finite elements . . . . .	35
4.3	Solving the differential equation . . . . .	37
4.4	Adaptive solution process . . . . .	39
<b>5</b>	<b>Numerical Investigations of Antennas in TEM Cells</b>	<b>39</b>
5.1	Preliminary Considerations for Numerical Analysis . . . . .	39
5.1.1	Antenna models . . . . .	39
5.1.2	TEM cell model . . . . .	40
5.1.3	Dipole moments models . . . . .	40
5.1.4	Mesh modifications . . . . .	41
5.1.5	Shielding material models . . . . .	42

5.1.6	S-parameters and derived data . . . . .	42
5.1.7	Investigation of Field Regions . . . . .	43
5.2	Monopole Antenna . . . . .	45
5.2.1	Setup . . . . .	45
5.2.2	Equivalent dipole moments . . . . .	45
5.2.3	Electrical characteristics . . . . .	46
5.2.4	Equivalent circuit model . . . . .	49
5.2.5	Current distribution on septum . . . . .	51
5.2.6	Electromagnetic energy in the TEM cell . . . . .	52
5.3	Loop antenna . . . . .	53
5.3.1	Setup . . . . .	53
5.3.2	Equivalent dipole moments . . . . .	53
5.3.3	Electrical characteristics . . . . .	55
5.3.4	Equivalent circuit model . . . . .	57
5.3.5	Current distribution on septum and higher order modes . . . . .	59
5.3.6	Influence of antenna's geometry . . . . .	61
5.4	Loop antenna with gap . . . . .	62
5.4.1	Setup and geometrical analysis . . . . .	62
5.4.2	Equivalent dipole moments . . . . .	63
5.4.3	Electrical characteristics . . . . .	63
5.5	Inverted-F and center-fed monopole antenna . . . . .	66
5.5.1	Setup and geometrical analysis . . . . .	66
5.5.2	Equivalent dipole moments . . . . .	66
<b>6</b>	<b>Application of Shielding Techniques in TEM Cells</b>	<b>67</b>
6.1	ASTM ES7-83 method . . . . .	67
6.2	Dual TEM cell . . . . .	68
6.3	Antennas in shield enclosure . . . . .	71
6.4	Dipole moments in shield enclosure . . . . .	73
<b>7</b>	<b>Conclusion</b>	<b>75</b>

## List of Figures

2.1	Geometrical arrangement of an infinitesimal electric dipole [3, p. 152]. . . . .	3
2.2	The geometry of a linear, center-fed wire antenna is depicted with the feed-point located at its center. The feedpoint is represented by a small gap through which a current $I_0$ is supplied to the antenna [15, p. 417]. . . . .	6
2.3	The current distribution along a linear wire antenna reaches its maximum at the feedpoint and decreases to zero at the endpoints, located at $d/2$ and $-d/2$ [3, p. 163]. . . . .	7
2.4	The geometry of a current loop with radius $b$ is shown, where the loop is fed with a current $I_0$ that generates a magnetic dipole moment $\mathbf{m}_m$ . Alternatively, an equivalent magnetic dipole moment can be produced by a magnetic current $I_m$ flowing perpendicular to the plane of the loop over a distance $L$ . . . . .	8
2.5	The behavior of Expression 1 and Expression 2 in (2.20) is analyzed as a function of distance $r$ . Here, $r$ is normalized to the radian distance $\lambda/2\pi$ , and the magnitudes of both expressions are scaled to unity at the radian distance to facilitate comparison [3, p. 157]. . . . .	9
2.6	Field regions of an antenna, here specifically a linear wire antenna, although they are applicable for any antenna with dimension $d$ [3, p. 34]. . . . .	10
3.1	The electric and magnetic fields corresponding to the first dominant TE and TM modes in a rectangular waveguide with perfectly conducting walls.	15
3.2	In this analysis, the Green's function determines the fields within the cross-sectional surface $S$ of the TEM cell, which is shown in light gray and bounded by $l$ . The source exciting these fields is a centrally located electric dipole moment, $\mathbf{m}_e$ . . . . .	17
3.3	Transverse electric field distributions in the cross section of the TEM cell. .	18
3.4	Geometrical arrangement of the TEM cell, demonstrated with cross sections in the $xy$ -plane and the $yz$ -plane. . . . .	19
3.5	Forward transmission coefficients $S_{12}$ of the TEM, $TE_{01}$ , and $TE_{10}$ modes in the TEM cell over frequency. . . . .	19
3.6	Electric and magnetic field distributions of the TEM, $TE_{01}$ , and $TE_{10}$ modes in the TEM cell. The magnetic fields are shown along the full length of the cell, while the electric fields are shown at the ports only. . . . .	21
3.7	Output power and $\mathbf{e}_{TEM}^{\pm}$ for different electric dipole moment positions and orientations. . . . .	23
3.8	The normalized electric field distribution $\mathbf{e}_{TEM}^{\pm}$ in the TEM cell excited with an input power of $1/2$ W at a frequency of 3 GHz. . . . .	23
3.9	TEM cell with an arbitrary current source $\mathbf{J}_1$ along the line $\tau$ . $\mathbf{E}$ and $\mathbf{H}$ are the field intensities induced by the current. $\mathbf{e}_n^+$ and $\mathbf{e}_n^-$ are outgoing fields towards both output ports of the TEM cell. $\mathbf{S}$ indicates the surface, and $V$ the volume of the domain in question. . . . .	24
3.10	Field distribution of the TEM mode highlighting the out-of-phase magnetic fields at the output ports. . . . .	27

3.11 Sketch of the surfaces $S_0, S_1$ and $S_2$ in the TEM cell with an example antenna, coupling through $S_0$ to the septum over the displacement current $\partial\mathbf{D}/\partial t$ . . . . .	29
3.12 Incident, reflected and transmitted electric field intensities at a shielding material . . . . .	31
3.13 Cross section of shielding material in TEM cell . . . . .	34
3.14 Dual TEM cell with aperture . . . . .	34
4.1 Tetrahedron with points on the edge and vertices . . . . .	36
4.2 Face of the finite element with unknowns . . . . .	37
4.3 Adaptive solution process . . . . .	39
5.1 Geometry of an antenna's feedpoint used in simulation. The antenna is fed through a round waveport of diameter 0.46 mm. The antenna consists of PEC wire with diameter of 0.2 mm. This geometry leads to a reference impedance of $Z_0 \approx 50 \Omega$ . . . . .	40
5.2 Circuit representing the TEM cell, where the capacitance and inductance is split into two separate, equal components $C_T = C_{T1} + C_{T2}$ , $L_T = L_{T1} + L_{T2}$ and $C_{T1} = C_{T2}$ , $L_{T1} = L_{T2}$ . The resistances $R_1, R_2$ at the output ports model the reference impedance $Z_w \approx 50 \Omega$ . . . . .	41
5.3 Numerical model of a TEM cell containing an electric moment $\mathbf{m}_e$ and a magnetic dipole moment $\mathbf{m}_m$ positioned at the center ( $x = 0, y = r = b/4, z = 0$ ). This setup is used to investigate the specific field regions in which coupling occurs . . . . .	44
5.4 Comparison of coupling behavior: (a) The normalized output power produced by dipole moments in the large versus the small TEM cell, and (b) the dipole moments used as the source. The congruence of the power curves demonstrates that the coupling is independent of the cell dimensions . . . . .	44
5.5 The geometrical aspects of the cylindrical monopole antenna, as implemented in the simulation model, with the respective electric near-field plot . . . . .	45
5.6 The equivalent electric and magnetic dipole moments analytically calculated with Equations (3.46a) to (3.46b). To enable direct comparison with the magnetic dipole moment, the electric dipole moment is weighted with the free space impedance $Z_0$ , as discussed in subsubsection 5.1.3 . . . . .	46
5.7 Magnitude of the voltage and current applied at the feedpoint of the monopole antenna over frequency, derived through the S-parameters with Equations (5.5) to (5.6), with the respective magnitude and phase of the antenna impedance over frequency, derived through the S-parameters with Equation 5.7 . . . . .	47
5.8 Electric field in y-direction $E_y$ at $x = 0, y = b/4, z = \pm l/2$ , and power at one output port, derived with the S-parameters in Equation 5.3. The output power produced by the monopole antenna is compared to the output power produced by the equivalent dipole moments, to demonstrate validity of the model . . . . .	48
5.9 Current distribution at 3 GHz . . . . .	48
5.10 Current distribution at 1 MHz . . . . .	48
5.11 The current distribution along the monopole antenna at 3 GHz and 1 MHz . . . . .	48
5.12 The Chu equivalent circuit for a short electric dipole models the monopole antenna's behavior . . . . .	49

5.13 Model of the monopole antenna connected to a feedpoint mounted on a PEC surface with a side length of $\lambda/2$ , where $\lambda$ corresponds to the free-space wavelength of the solution frequency. This configuration enables the investigation of the monopole antenna reactance without influence of the TEM cell. . . . .	50
5.14 Circuit representing the TEM cell and the monopole antenna, with the additional components $C_k$ and $M_{A,T1}$ , $M_{A,T2}$ modeling their near-field coupling behavior. . . . .	50
5.15 Equivalent dipole moments derived by the equivalent circuit depicted in Figure 5.2, compared to the derived dipole moments of the monopole antenna, shown in Figure 5.6. The electric dipole moment $\mathbf{m}_e$ is weighted with $\eta_0$ for comparison purposes. . . . .	51
5.16 Current surface densities at different frequencies, below and above the cut-off frequency of the $TE_{01}$ -mode. . . . .	52
5.17 Electric energy determined by integrating the electric field over the TEM cell volume, using Equation 2.24. . . . .	53
5.18 The geometry of the loop antenna assimilates a square with round edges. The height and width of the antenna equal $h = w = 1.6$ mm. The return path leads back to the PEC surface of the TEM cell. The electric near-field shows large a displacement current and voltage drop near the feed-point. It has been derived with a refined mesh on the antenna surface and near the feedpoint, according to the discussion in Section 5.1.4. . . . .	54
5.19 The equivalent dipole moments of the loop antenna are derived analytically with Equations (3.46a) to (3.46b), where the electric dipole moment $\mathbf{m}_e$ is weighted with $Z_0$ to enable comparison with $\mathbf{m}_m$ . The phases of the powers at output ports 1 and 2 are derived from the S-parameters, as discussed in Section 5.1.6. The analysis specifically focuses on the phase shift between the two ports, which provides information about the presence of $\mathbf{m}_m$ and $\mathbf{m}_e$ , as investigated in Section 3.5.2. . . . .	54
5.20 Electric field in y-direction $E_y$ at $x = 0, y = b/4, z = \pm l/2$ , and the closely related power at one of the output ports, derived with the S-parameters in Equation 5.3. The output power produced by the loop antenna is compared with that generated by the equivalent dipole moments. . . . .	55
5.21 Electric and magnetic energy produced by the loop antenna in the TEM cell, derived with Equation 2.24 in the TEM cell volume. . . . .	56
5.22 This figure demonstrates the voltage, current and impedance characteristics of the loop antenna. The difference between the current near the feedpoint and that on the return path increases with frequency, indicating a growing occurrence of displacement currents. The current on those paths are determined through magnetic near-field intensity, using Equation 5.9. The voltage across the feedpoint is obtained using Equation 5.6. Magnitude and phase of the impedance of the loop antenna are determined with Equation 5.7. . . . .	56
5.23 Equivalent circuits of the small loop antenna. . . . .	57

5.24	Model of the loop antenna connected to a feedpoint mounted on a PEC surface with a side length of $\lambda/2$ , where $\lambda$ corresponds to the free-space wavelength of the solution frequency. This configuration enables the investigation of the loop antenna reactance without influence of the TEM cell.	58
5.25	Circuit representing the TEM cell and the loop antenna, with the additional components $C_k$ and $M_{A,T1}$ , $M_{A,T2}$ modeling their near-field coupling behavior.	58
5.26	Equivalent dipole moments derived by the equivalent circuit depicted in Figure 5.25, compared to the dipole moments of the loop antenna, shown in Figure 5.19a. The electric dipole moment $\mathbf{m}_e$ is weighted with $\eta_0$ for comparison purposes.	59
5.27	Surface current density on the septum induced by the loop antenna for different frequencies and positions of the antenna.	60
5.28	Output power transmitted by the antenna to the output port through the TEM and $TE_{01}$ modes, separately over frequency, determined through the S-parameters with Equation 5.3. At a frequency of $f = 3.21$ GHz a resonance in the TEM cell occurs, leading to the visible peak in the output power produced by the $TE_{01}$ mode.	61
5.29	Dipole moments and output power comparisons of two different loop antenna configurations presented, one with $h = 2.16$ mm, $w = 1.4$ mm and the other with $h = 1.2$ mm, $w = 2.36$ mm. The electric dipole moment $\mathbf{m}_e$ is weighted with $Z_0$ for comparison purposes.	62
5.30	Geometry of the loop antenna with a gap in the return path inserted in the TEM cell. The gap height is exaggerated for demonstration purposes.	63
5.31	The equivalent dipole moments of the loop antenna with a gap, where the electric dipole moment $\mathbf{m}_e$ is weighted with $Z_0$ to enable comparison with $\mathbf{m}_m$ . The phases of the powers at output ports 1 and 2 are derived from the S-parameters, as discussed in Section 5.1.6. The analysis specifically focuses on the phase shift between the two ports, which provides information about the presence of $\mathbf{m}_m$ and $\mathbf{m}_e$ , as investigated in Section 3.5.2.	64
5.32	Comparison of dipole moments, where the electric dipole moment $\mathbf{m}_e$ is weighted with $\eta_0$ to enable comparison with $\mathbf{m}_m$ , and output power for different gap heights in the loop antenna.	65
5.33	The voltage and current across the feedpoint, together with the related impedance of the loop antenna with gap.	65
5.34	Geometries of IFA and CFM antenna, together with their equivalent dipole moments. the electric dipole moment $\mathbf{m}_e$ is weighted with the free space impedance $Z_0$ to enable comparison with the magnetic dipole moment $\mathbf{m}_m$ .	66
6.1	Shielding effectiveness of a thin sheet of ferrite, barium titanate, and silver as a function of frequency, determined using the ASTM ES7-83 method.	68
6.2	The sum $P_{\text{ref,sum}}$ and difference $P_{\text{ref,diff}}$ of the reference power, measured with an empty aperture and calculated with phase information considered.	69
6.3	The sum $P_{\text{load,sum}}$ and difference $P_{\text{load,diff}}$ of the output power measured at ports 3 and 4 with phase information considered.	70
6.4	Electric $SE_{\text{dB}}^e$ and magnetic $SE_{\text{dB}}^m$ shielding effectiveness of (a) silver and (b) barium titanate and ferrite, derived according to (3.68a) and (3.68b).	70

6.5	Investigated antennas placed inside a hollow cubic enclosure within the TEM cell. . . . .	71
6.6	Radiated power as a function of frequency for the loop and monopole antennas with and without enclosure. . . . .	72
6.7	Radiated power as a function of frequency for the loop and monopole antennas with varying enclosure wall thickness. . . . .	73
6.8	Electric near-field distribution of the loop antenna at the resonance frequency of 2.5 GHz, with a barium titanate shielding enclosure of 100 $\mu\text{m}$ wall thickness. . . . .	73
6.9	Radiated power as a function of frequency for the loop and monopole antenna equivalent dipole moments in enclosures of different materials at a constant wall thickness of 10 $\mu\text{m}$ . . . . .	74

## List of Tables

3.1	Cutoff frequencies of the TE <sub>01</sub> and TE <sub>10</sub> modes for different TEM cell dimensions, derived both through numerical simulation and analytical calculation. The results of these separate methods agree within the precision shown. As expected from (3.27), the TE <sub>10</sub> cutoff frequency depends only on $a$ and is independent of $b$ , consistent with rectangular waveguide theory. The TE <sub>01</sub> cutoff frequency varies with both $a$ and $b$ .	20
6.1	Electromagnetic properties of ferrite, barium titanate, and silver.	67

## 1 Introduction

In recent years, electronic systems have demonstrated a clear trend toward reduced physical dimensions and increased operating speeds, consequently, higher frequencies are used. As a result, these systems often contain small conducting structures that carry currents and voltages with high amplitudes and frequencies. These structures tend to radiate and are susceptible to electromagnetic radiation, behaving as antennas and causing electromagnetic compatibility (EMC) issues.

Taking EMC into account during the design of electronic systems helps to minimize additional costs and schedule delays that may arise from potential redesigns. Furthermore, it ensures that the product operates reliably when exposed to interference from external sources [29, p. 64]. Consequently, research focusing on all aspects of EMC is conducted regularly. This thesis aims to contribute to these ongoing investigations, specifically through analysis of the previously mentioned small antennas and their coupling behavior in TEM cells. TEM cells are included because they provide a standardized method for measuring electromagnetic emissions under approximate free-space conditions and have been widely used for testing small devices [10, 19, 12].

Several studies have analyzed the coupling behavior of small antennas and devices with TEM cells [32, 22]. Specifically, [21, 20, 36] implement electric and/or magnetic dipole moments to model the radiated fields of such antennas, which provide information about the electric and magnetic coupling with the TEM cell, respectively. The magnitudes of the dipole moments are found by measurements with the TEM cell [32] or numerical analysis [20]. This thesis treats the coupling behavior of small antennas modeled with dipole moments using the latter approach, namely numerical computation using the finite element method. The advantage of this approach is the absence of inaccuracies caused by the measurement setup or related uncertainties, allowing the analysis to focus on the underlying mechanics behind the coupling behavior.

This thesis aims to explain how the electric and magnetic dipole moments of antennas are created and what factors affect them. Understanding this helps design electronic devices that meet EMC requirements and achieve specific coupling behaviors. Additionally, replacing the small antennas with their equivalent dipole moments significantly reduces computational effort, which is particularly advantageous when dealing with large computational domains.

Furthermore, this thesis investigates the shielding efficiency of different materials in the presence of dipole moments. The performance of the shielding material with respect to the electric and magnetic coupling behavior of the antennas, as reflected by the dipole moments, is investigated. The results assist in the selection of appropriate shielding material to effectively reduce emissions produced by the antennas.

To achieve these objectives, this thesis first presents the theoretical foundations of electric and magnetic dipole moments in Section 2. The behavior of electromagnetic waves generated by arbitrary sources in waveguides, specifically the TEM cell, is then discussed in Section 3. Further, background information of electromagnetic shielding and methods to determine shielding effectiveness using the TEM cell are presented. A brief overview of

the finite element method is provided in Section 4.

Subsequently, Section 5 addresses the numerical modeling of antennas and the TEM cell and investigates the generation of electric and magnetic dipole moments for monopole and loop antennas using the theoretical framework developed earlier. This knowledge is applied to three additional antennas, whose analysis delivers results closely related to that of the monopole and loop antennas due to their shared predominantly inductive or capacitive characteristics, which emerge as the primary distinction in the antenna coupling behavior. Equivalent circuits to model capacitive and inductive antennas, together with the TEM cell and their coupling paths, are developed, from which the dipole moments can be investigated in more detail.

Section 6 demonstrates the application of shielding materials in numerical simulations involving dipole moments and electrically small antennas. Lastly, section 7 presents the conclusions and discussion derived from this thesis, along with potential directions for future research.

## 2 Dipole Theory

### 2.1 Electric Dipoles

#### 2.1.1 Infinitesimal Electric Dipoles

An electric dipole can be modeled as two tiny charged metal spheres [11, p. 467], or alternatively two capacitor-plates [3, p. 151], connected with a linear wire of length  $d$  and diameter  $a$ . The charges accelerate along the wire and radiate. In case of an ideal, infinitesimal dipole, the wire is very thin ( $a \ll \lambda$ ) and very small ( $d \ll \lambda$ ) compared to the wavelength  $\lambda$  [3, p. 151, 11, p. 468]. For an antenna to be accurately modeled as an infinitesimal electric dipole, its length must be smaller than a fiftieth of the wavelength ( $d < \lambda/50$ ) [3, p. 156]. They are not very practical, but serve as a basic building block for more complex geometries, or as an excitation source in numerical investigations.

An infinitesimal electric dipole, illustrated in Figure 2.1, is analyzed in detail below. The dipole is aligned with the  $z$ -axis, which simplifies the following mathematical investigations. Time variation according to  $e^{-j\omega t}$  is assumed and therefore omitted in this thesis. A current flows in the wire, which is spatially uniform throughout the wire. This is expressed as [3, p. 151]

$$\mathbf{I}(z) = \hat{\mathbf{a}}_z I_0. \quad (2.1)$$

To permit a constant current across the wire, which is otherwise physically impossible, capacitor plates are modeled at its ends. The electric dipole moment can be expressed as

$$\mathbf{m}_e = I_0 d \cdot \hat{\mathbf{a}}_z. \quad (2.2)$$

Next, the vector potential  $\mathbf{A}$  is determined through

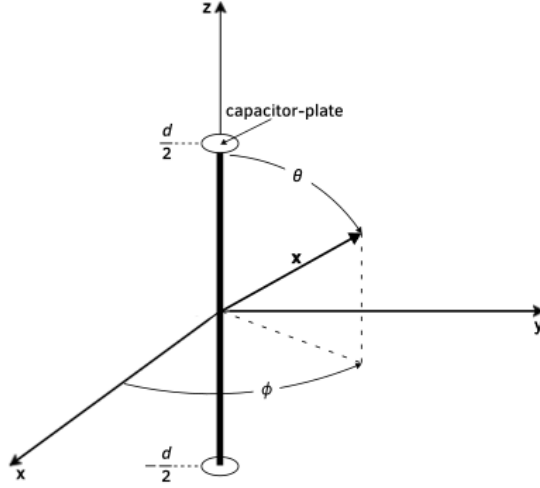


**Figure 2.1** Geometrical arrangement of an infinitesimal electric dipole [3, p. 152].

$$\mathbf{A}(\mathbf{x}) = \frac{\mu}{4\pi} \frac{e^{-jkr}}{r} \iiint_V \mathbf{J}(\mathbf{x}') dv', \quad (2.3)$$

where

$\mathbf{x}$	observation point coordinates $\hat{\mathbf{a}}_x x + \hat{\mathbf{a}}_y y + \hat{\mathbf{a}}_z z$ ,
$\mathbf{x}'$	source point coordinates $\hat{\mathbf{a}}_x x' + \hat{\mathbf{a}}_y y' + \hat{\mathbf{a}}_z z'$ ,
$\mathbf{J}$	current density in the source region,
$r$	distance from source to observation point $ \mathbf{x} - \mathbf{x}' $ ,
$\mu$	permeability of the medium,
$k = 2\pi/\lambda$	wavenumber,
$e^{-jkr}$	phase factor describing the wave propagation with distance.

For the infinitesimal dipole, the source is located at the origin, so  $\mathbf{x}' = \mathbf{0}$  [3, p. 152]. Since the wire is assumed very thin, the volume integral in (2.3) reduces to a line integral along the dipole axis. With the constant current distribution given in (2.12),  $I_0$  can be pulled out of the integral. Evaluating the remaining integral over the dipole length  $d$  yields [3, p. 153]

$$\begin{aligned} \mathbf{A}(\mathbf{x}) &= \hat{\mathbf{a}}_z \frac{\mu I_0}{4\pi r} e^{-jkr} \int_{-d/2}^{+d/2} dz' \\ &= \hat{\mathbf{a}}_z \frac{\mu I_0 d}{4\pi r} e^{-jkr}. \end{aligned} \quad (2.4)$$

All other field quantities can be derived from the vector potential  $\mathbf{A}$ , such as the electric field intensity  $\mathbf{E}$  and magnetic field intensity  $\mathbf{H}$ . To simplify this process, the Cartesian components of  $\mathbf{A}$  are first transformed into spherical ones. This transformation is given in matrix form as [3, p. 153]

$$\begin{bmatrix} A_r \\ A_\theta \\ A_\phi \end{bmatrix} = \begin{bmatrix} \sin \theta \cos \phi & \sin \theta \sin \phi & \cos \theta \\ \cos \theta \cos \phi & \cos \theta \sin \phi & -\sin \theta \\ -\sin \phi & \cos \phi & 0 \end{bmatrix} \begin{bmatrix} A_x \\ A_y \\ A_z \end{bmatrix}, \quad (2.5)$$

where  $\theta$  is the polar angle and  $\phi$  is the azimuthal angle of the observation point  $\mathbf{x}$ .  $\mathbf{E}$  and  $\mathbf{H}$  are then expressed by [3, p. 153],

$$\mathbf{H} = \frac{1}{\mu r} \left[ \frac{\partial}{\partial r} (r A_\theta) - \frac{\partial A_r}{\partial \theta} \right] \hat{\mathbf{a}}_\phi, \quad (2.6a)$$

$$\mathbf{E} = -j\omega \mathbf{A} - j \frac{1}{\omega \mu \epsilon} \nabla (\nabla \cdot \mathbf{A}). \quad (2.6b)$$

Substituting (2.4) into (2.6a) yields

$$H_r = H_\theta = 0, \quad (2.7a)$$

$$H_\phi = j \frac{k I_0 d \sin \theta}{4\pi r} \left[ 1 + \frac{1}{jkr} \right] e^{-jkr}, \quad (2.7b)$$

and substituting into Equation (2.6b) yields

$$E_r = \eta \frac{I_0 d \cos \theta}{2\pi r^2} \left[ 1 + \frac{1}{jkr} \right] e^{-jkr}, \quad (2.8a)$$

$$E_\theta = j\eta \frac{k I_0 d \sin \theta}{4\pi r} \left[ 1 + \frac{1}{jkr} - \frac{1}{(kr)^2} \right] e^{-jkr}, \quad (2.8b)$$

$$E_\phi = 0, \quad (2.8c)$$

where  $\eta = \sqrt{\frac{\mu}{\epsilon}}$  is the wave impedance of the medium in which the waves travel.

The total radiated power of the dipole is obtained by integrating the complex Poynting vector  $\mathbf{S}$  over a closed surface surrounding the dipole [3, p. 154]. The real part of the total radiated power provides information about energy transferred by radiation, while the imaginary part about the antenna's reactive behavior.  $\mathbf{S}$  is defined by

$$\mathbf{S} = \frac{1}{2} (\mathbf{E} \times \mathbf{H}^*). \quad (2.9)$$

The real power transfer is derived through the time-averaged Poynting vector  $\mathbf{S}_{av}$  [3, p. 160], which is calculated by

$$\mathbf{S}_{av} = \frac{1}{2} \Re \{ \mathbf{E} \times \mathbf{H}^* \}. \quad (2.10)$$

The complex power  $P$  is derived by integrating  $\mathbf{S}$  over a closed surface around the dipole, which leads to [3, p. 154]

$$P_r = \eta \frac{\pi}{3} \frac{|I_0 l|^2}{\lambda} \left[ 1 - j \frac{1}{(kr)^3} \right]. \quad (2.11)$$

The imaginary part of the power radiated by the infinitesimal electric dipole shows capacitive behavior, as demonstrated by Equation 2.11.

### 2.1.2 Small Electric Dipoles

Wires that are too long to be modeled as infinitesimal dipoles, but short enough to be considered electrically small ( $\lambda/50 < l \leq \lambda/10$ ), are classified as small physical dipoles [3, pp. 162-163]. These dipoles provide a more accurate and practical representation of linear wire antennas, and are examined in greater detail below.

A current  $I_0$  is fed into the short, center-fed, linear antenna shown in Figure 2.1. The current along the antenna arms  $I(z)$  linearly drops to zero [15, p. 412], as visualized in Figure 2.3. Mathematically, it is described by,

$$\mathbf{I}(z) = I_0 \left( 1 - \frac{2|z|}{d} \right) \cdot \hat{\mathbf{a}}_z. \quad (2.12)$$

This current distribution differs from that of the infinitesimal dipole, and as a result, the capacitor plates are not required in this model. Additionally, charge accumulates along the antenna due to the linear decrease in current  $\mathbf{I}$ . This accumulation is characterized by the charge per unit length,  $\rho'$ , which is appropriate for a thin wire. The relationship is derived from the continuity equation,  $\partial\rho/\partial t = -\nabla \cdot \mathbf{J}$ . In the frequency domain, this becomes  $j\omega\rho = -\nabla \cdot \mathbf{J}$ . Substituting this into Equation 2.12 yields [15, pp. 410-412].

$$\rho' = \pm \frac{d}{dz} j \frac{I(z)}{\omega} = \pm j \frac{2I_0}{\omega d}. \quad (2.13)$$

$\rho'$  is uniformly distributed along each antenna arm.

Next, the vector potential  $\mathbf{A}$  is determined using Equation 2.3. The calculations of  $\mathbf{A}$  simplify to [15, p. 410],

$$\mathbf{A}(\mathbf{x}) = \hat{\mathbf{a}}_z \frac{\mu I_0 d}{8\pi r} e^{-jkr} \quad (2.14)$$

The formulation of  $\mathbf{A}$  now includes an additional factor of 1/2 compared to the previously derived expression for infinitesimal dipoles in Equation 2.4. This factor arises from the integration of  $\mathbf{I}$ : when integrated over the interval  $[-d/2, d/2]$ , a linearly decreasing  $\mathbf{I}$  yields half the value obtained from a constant  $\mathbf{I}$ . For the same reason, the electric dipole moment  $\mathbf{m}_e$  is also reduced to half of that in Equation 2.2.

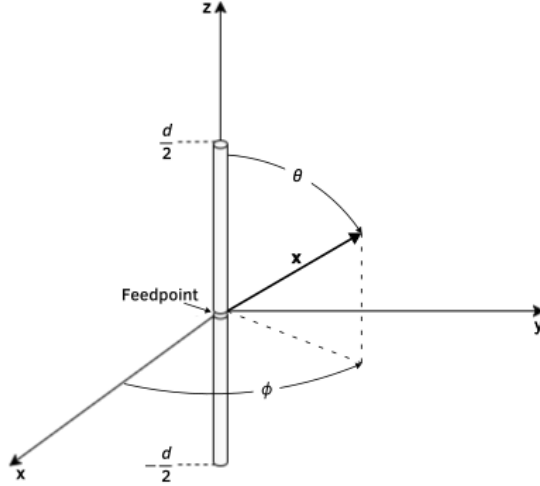


**Figure 2.2** The geometry of a linear, center-fed wire antenna is depicted with the feedpoint located at its center. The feedpoint is represented by a small gap through which a current  $I_0$  is supplied to the antenna [15, p. 417].

Furthermore, for the sake of simplicity, it is reasonable to set  $\mathbf{x}' = \mathbf{0}$ . This approximation has been shown to be sufficient for large  $r$ , with the resulting amplitude error remaining negligible even for small  $r$  [15, p. 409, 3, pp. 164-168].

The short physical electric dipole described in this section serves as an approximation for the behavior of electrically short antennas. Particular attention must be paid to the excitation method and physical shape, as these factors significantly influence antenna behavior [15, p. 413]. Furthermore, any antenna analyzed using this approach should remain much smaller than the wavelength  $\lambda$  to minimize analytical approximation errors.

## 2.2 Magnetic Dipoles

The magnetic dipole moment characterizes the strength of a magnetic source. An electrically small current loop fed with a current  $I_0$  can be used to model the magnetic dipole, as demonstrated in Figure 2.4. This approximation is valid provided the overall loop circumference satisfies  $2\pi b < \lambda/10$  and the wire is assumed very thin [3, p. 231]. Furthermore, the radiation pattern of the magnetic dipole is equal to that of the electric dipole, with the role of the electric and magnetic fields interchanged [11, p. 254].

The magnetic dipole moment  $\mathbf{m}_m$  is given by

$$\mathbf{m}_m = I_m L \cdot \hat{\mathbf{a}}_z. \quad (2.15)$$

Furthermore, the magnetic current  $I_m$  and the electric current  $I_0$  in the loop are related with [3, p. 237]

$$I_m L = j A \omega \mu_0 I_0 \quad (2.16)$$

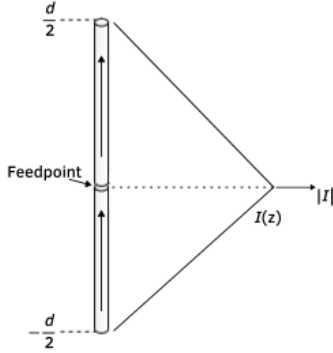


**Figure 2.3** The current distribution along a linear wire antenna reaches its maximum at the feedpoint and decreases to zero at the endpoints, located at  $d/2$  and  $-d/2$  [3, p. 163].

with  $A = \pi b^2$  denoting the area of the current loop. Analogous to the separation distance  $d$  in the electric dipole,  $L$  is the length of the magnetic dipole. The electric and magnetic field intensities  $\mathbf{E}$  and  $\mathbf{H}$  produced by the dipole and current loop are the same. Thus, the infinitesimal magnetic dipole  $I_m L$  and the electrically small current loop  $jA\omega\mu_0 I_0$  are equivalent representations [3, p. 237]. The electric field intensity  $\mathbf{E}$  of the magnetic dipole is given by

$$E_r = E_\theta = 0, \quad (2.17a)$$

$$E_\phi = -j \frac{k I_m L \sin \theta}{4\pi r} \left[ 1 + \frac{1}{jkr} \right] e^{-jkr}, \quad (2.17b)$$

and the magnetic field intensity by [3, p. 237]

$$H_r = \frac{I_m L \cos \theta}{2\pi r^2 \eta} \left[ 1 + \frac{1}{jkr} \right] e^{-jkr}, \quad (2.18a)$$

$$H_\theta = j \frac{k I_m L \sin \theta}{4\pi r \eta} \left[ 1 + \frac{1}{jkr} - \frac{1}{(kr)^2} \right] e^{-jkr}, \quad (2.18b)$$

$$H_\phi = 0. \quad (2.18c)$$

The complex power density  $\mathbf{S}$  can be derived following the same approach as for the electric dipole (see Equation 2.9). For the magnetic dipole, the imaginary part of  $\mathbf{S}$  has the opposite sign compared to the electric dipole. This is the result of the near-field power being inductive in case of the magnetic dipole, while it is capacitive for the electric dipole. The complex power equals [3, p. 238]

$$P_r = \eta \left( \frac{\pi}{12} \right) (kb)^4 |I_0|^2 \left[ 1 + j \frac{1}{(kr)^3} \right]. \quad (2.19)$$

### 2.3 Radiated Field

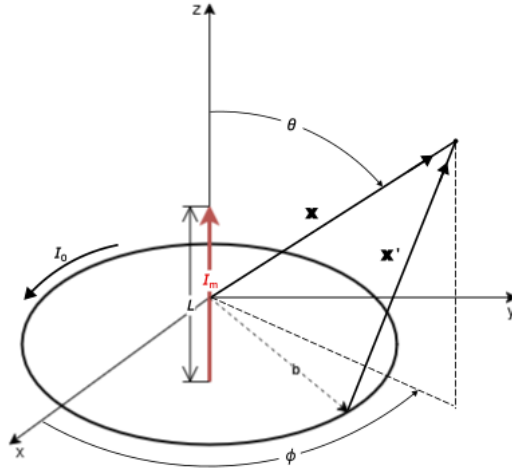


**Figure 2.4** The geometry of a current loop with radius  $b$  is shown, where the loop is fed with a current  $I_0$  that generates a magnetic dipole moment  $\mathbf{m}_m$ . Alternatively, an equivalent magnetic dipole moment can be produced by a magnetic current  $I_m$  flowing perpendicular to the plane of the loop over a distance  $L$ .

### 2.3.1 Field regions

This section investigates the field regions of the radiated fields, beginning with the infinitesimal electric dipole, from which the analysis extends analogously to magnetic dipoles. The field quantities  $\mathbf{E}$  and  $\mathbf{H}$  derived in (2.7) and (2.8) demonstrate that the behavior of the fields depends on the distance  $r$  from the dipole [3, p. 156]. This dependence is governed by the terms  $1/(jkr)$  and  $1/(kr)^2$ , which are highlighted for clarity in the expression for  $E_\theta$ :

$$E_\theta = j\eta \frac{kI_0 d \sin \theta}{4\pi r} \left[ 1 + \underbrace{\frac{1}{jkr}}_{\text{Expression 1}} - \underbrace{\frac{1}{(kr)^2}}_{\text{Expression 2}} \right] e^{-jkr}, \quad (2.20)$$

where  $1/(jkr)$  also appears in  $E_r$  and  $H_\phi$ , while  $1/(kr)^2$  appears only in  $E_\theta$ . The variation of Expression 1 and Expression 2 with distance is shown in Figure 2.5.

If the distance  $r < \lambda/2\pi$  (or equivalently,  $kr < 1$ ), then Expression 2 dominates over the other terms. Consequently, the energy stored in this region is predominantly imaginary. This region is referred to as the near-field region [3, pp. 156-157].

At distances  $r > \lambda/2\pi$  ( $kr > 1$ ), Expression 1 exceeds Expression 2 in magnitude, such that the real part of the energy exceeds the imaginary part. This region is referred to as the intermediate-field region [3, p. 157].

At large distances  $r \gg \lambda/2\pi$  ( $kr \gg 1$ ) the energy is predominantly real, reflecting radiated energy propagating outward. This region is referred to as the far-field region [3, p. 157].

At  $r = \lambda/2\pi$  ( $kr = 1$ ), Expression 1 and Expression 2 attain equal magnitudes, a distance referred to as the radian distance [3, pp. 156-160]. The radian distance thus represents a critical transition between field regions, as shown in Figure 2.5.

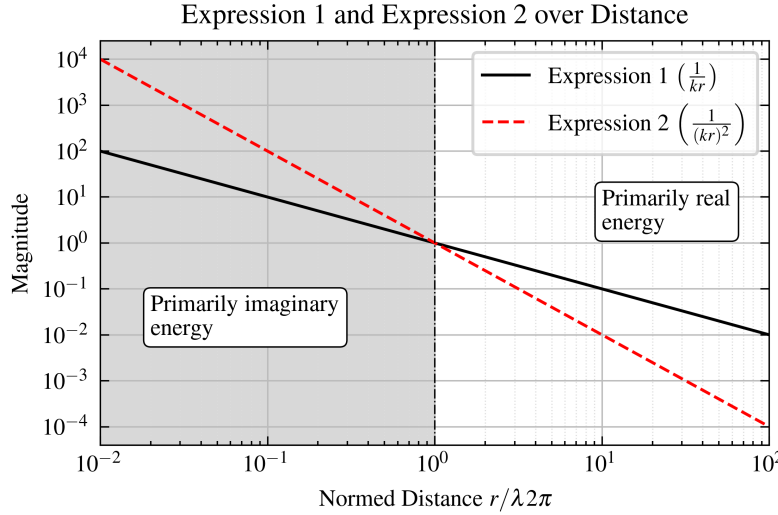


**Figure 2.5** The behavior of Expression 1 and Expression 2 in (2.20) is analyzed as a function of distance  $r$ . Here,  $r$  is normalized to the radian distance  $\lambda/2\pi$ , and the magnitudes of both expressions are scaled to unity at the radian distance to facilitate comparison [3, p. 157].

For antennas that cannot be approximated as electrically small, the field region boundaries depend on the antenna's physical dimensions rather than the wavelength alone. The regions for such an antenna are shown in Figure 2.6.

The radiating near-field occurs at distances larger than approximately  $r_1$  and the far-field region at approximately  $r_2$ , which are defined as [3, p. 34]

$$r_1 = 0.62\sqrt{d^3/\lambda}, \quad (2.21a)$$

$$r_2 = 2d^2/\lambda, \quad (2.21b)$$

where  $d$  is the largest dimension of the antenna.

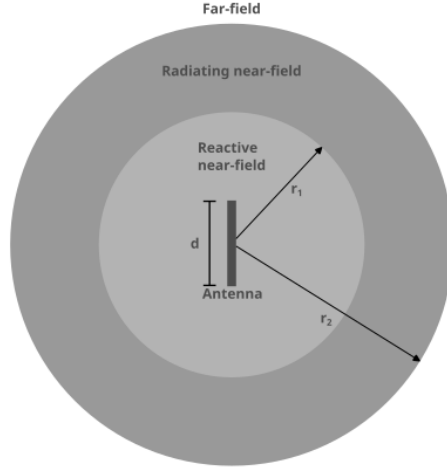


**Figure 2.6** Field regions of an antenna, here specifically a linear wire antenna, although they are applicable for any antenna with dimension  $d$  [3, p. 34].

### 2.3.2 Energy densities and reactances

The electric energy density  $w_e$  is defined as

$$w_e = \frac{1}{2} \mathbf{E} \cdot \mathbf{D}, \quad (2.22)$$

while the magnetic energy density  $w_m$  is given by

$$w_m = \frac{1}{2} \mathbf{B} \cdot \mathbf{H}. \quad (2.23)$$

By applying the constitutive relations  $\mathbf{D} = \epsilon \mathbf{E}$  and  $\mathbf{B} = \mu \mathbf{H}$ , and summing the contributions from (2.22) and (2.23), the total electromagnetic energy density  $w_{\text{em}}$  is obtained with [11, p. 330]

$$w_{\text{em}} = \frac{1}{2} \left( \underbrace{\epsilon E^2}_{\text{Electric energy } w_e} + \underbrace{\frac{1}{\mu} B^2}_{\text{Magnetic energy } w_m} \right). \quad (2.24)$$

Integrating  $w_{\text{em}}$  over a given volume yields the total electromagnetic energy  $W_{\text{em}}$  contained within that region. Similarly, integrating  $w_e$  provides the total electric energy  $W_e$ , and integrating  $w_m$  gives the total magnetic energy  $W_m$ .

The reactance of an electrically short antenna is directly related to the electric and magnetic energy densities,  $w_e$  and  $w_m$ . Therefore, the electric and magnetic energy stored can be represented by a lumped capacitor and inductor, respectively. This antenna's equivalent inductance and capacitance can be determined using the relationships [11, pp. 107, 328]

$$L = 2 \frac{W_m}{I^2}, \quad (2.25a)$$

$$C = 2 \frac{W_e}{V^2}, \quad (2.25b)$$

where  $V$  and  $I$  denote the terminal voltage and current.

### 3 Guided Waves

#### 3.1 Lorentz Reciprocity Theorem<sup>1</sup>

Let two source pairs  $\mathbf{J}_1, \mathbf{M}_1$  and  $\mathbf{J}_2, \mathbf{M}_2$  exist in a volume  $V$ , bounded by the closed surface  $S$ . The medium in  $V$  is linear and isotropic. The source pairs generate fields  $\mathbf{E}_1, \mathbf{H}_1$  and  $\mathbf{E}_2, \mathbf{H}_2$ , respectively, with the same frequency. The fields and source pairs can then be related with [3, p. 145, 8, p. 49]

$$-\nabla \cdot (\mathbf{E}_1 \times \mathbf{H}_2 - \mathbf{E}_2 \times \mathbf{H}_1) = \mathbf{E}_1 \cdot \mathbf{J}_2 + \mathbf{H}_2 \cdot \mathbf{M}_1 - \mathbf{E}_2 \cdot \mathbf{J}_1 - \mathbf{H}_1 \cdot \mathbf{M}_2. \quad (3.1)$$

Integrating Equation 3.1 over  $V$ , and converting the volume integral to a surface integral with the divergence theorem, leads to [3, p. 145, 8, p. 50]

$$\begin{aligned} & -\oint\int_S (\mathbf{E}_1 \times \mathbf{H}_2 - \mathbf{E}_2 \times \mathbf{H}_1) \cdot d\mathbf{s}' \\ &= \iiint_V (\mathbf{E}_1 \cdot \mathbf{J}_2 + \mathbf{H}_2 \cdot \mathbf{M}_1 - \mathbf{E}_2 \cdot \mathbf{J}_1 - \mathbf{H}_1 \cdot \mathbf{M}_2) \cdot dv'. \end{aligned} \quad (3.2)$$

This integral equation relates the coupling of different source points. Additionally, if one of these sources is set to zero, the respective source point can serve as an observation point. Setting all sources to zero allows investigation of the coupling of modal fields in a waveguide to other modes, as the following example shows. Suppose the volume  $V$  does not contain sources  $\mathbf{J}_1 = \mathbf{M}_1 = \mathbf{J}_2 = \mathbf{M}_2 = \mathbf{0}$ . Then, the source-free Lorentz Reciprocity theorem reduces to the condition that the modes in the waveguide must fulfill [3, pp. 145-146]:

$$\nabla \cdot (\mathbf{E}_1 \times \mathbf{H}_2 - \mathbf{E}_2 \times \mathbf{H}_1) = 0, \quad (3.3a)$$

$$\oint\int_S (\mathbf{E}_1 \times \mathbf{H}_2 - \mathbf{E}_2 \times \mathbf{H}_1) \cdot d\mathbf{s}' = 0. \quad (3.3b)$$

Another application arises when investigating a volume  $V$  confined by a perfectly conducting surface  $S$ , in which the linear current densities  $\mathbf{J}_1$  and  $\mathbf{J}_2$  flow. Because  $\mathbf{n} \times \mathbf{E}_1 = \mathbf{n} \times \mathbf{E}_2 = 0$  along the surface  $S$ , the surface integral in Equation 3.2 vanishes, leading to

---

<sup>1</sup>This section follows closely the treatment in: Robert E. Collin, *Field Theory of Guided Waves*, IEEE Press, 2015 and Constantine A. Balanis, *Antenna theory: Analysis and design*, Wiley, 1997.

$$\mathbf{E}_1 \cdot \mathbf{J}_2 = \mathbf{E}_2 \cdot \mathbf{J}_1. \quad (3.4)$$

This is the Rayleigh-Carson form of the Lorentz reciprocity theorem [8, p. 50]. It states that the component of  $\mathbf{E}_1$  along  $\mathbf{J}_2$  is equal to the component of  $\mathbf{E}_2$  along  $\mathbf{J}_1$ , and vice versa [8, p. 50].

In summary, the Lorentz Reciprocity theorem is useful for deriving reciprocal aspects of waveguides, finding orthogonal properties of modes, investigating fields generated by currents and dipole moments in waveguides [8, p. 50], among several other examples. This theorem will be employed often throughout the remainder of this thesis.

### 3.2 Green's Function<sup>2</sup>

#### 3.2.1 Scalar Green's Function

The Green's function describes the response of a linear differential operator  $L$  to a point source of unit strength. It is briefly introduced here through an example of solving Poisson's equation with boundary conditions, as this concept will be applied in later analysis. The general form for a Green's function of a given problem is [1, p. 512]

$$LG(\mathbf{x}, \mathbf{x}') = -\delta(\mathbf{x} - \mathbf{x}'). \quad (3.5)$$

A point source of unit strength is generally modeled with a delta function  $\delta$  at a certain point in one-dimensional space. In multi-dimensional space, a product of delta functions is used.

Once (3.5) is solved for a point source of unit strength and the corresponding Green's function  $G$  is determined for the specific problem,  $u$  can be solved for any given source distribution  $f$  [1, p. 512].

$$Lu(\mathbf{x}) = f(\mathbf{x}). \quad (3.6)$$

This is accomplished by superposing the responses to point sources of unit strength, as in [1, p. 512]

$$u(\mathbf{x}) = \iiint_V G(\mathbf{x}, \mathbf{x}') f(\mathbf{x}') dv', \quad (3.7)$$

where integration is performed over the source point variables  $x', y', z'$ .

One application of the Green's function is solving Poisson's equation. The scalar potential  $\phi$  can be calculated from a density of charge distribution  $\rho$  by using the Green's function of this specific problem. If there are no boundaries present, it takes the form [1, pp. 510-511, 8, p. 56]

---

<sup>2</sup>This section follows closely the treatment in: R. E. Collin, *Field Theory of Guided Waves*, IEEE Press, 2015 and G. B. Arfken and H. J. Weber, *Mathematical Methods for Physicists*, Academic Press, 2013

$$\nabla^2 \phi(\mathbf{x}) = -\frac{\rho(\mathbf{x})}{\epsilon}, \quad (3.8a)$$

$$\phi(\mathbf{x}) = \frac{1}{4\pi\epsilon} \iiint_V \frac{\rho(\mathbf{x}')}{|\mathbf{x} - \mathbf{x}'|} dv'. \quad (3.8b)$$

The Green's function for this problem is given by

$$G(\mathbf{x}, \mathbf{x}') = \frac{1}{4\pi|\mathbf{x} - \mathbf{x}'|}, \quad (3.9)$$

which represents the potential at position  $\mathbf{x}$  due to a unit point charge located at  $\mathbf{x}'$ . In this context, the input function is  $u = \phi$  and the source function is  $f = -\rho/\epsilon$  [1, pp. 510-511].

Solutions in different volumes of interest  $V_1, V_2, \dots, V_n$  can be matched across their shared surfaces  $S_1, S_2, \dots, S_n$  by imposing appropriate boundary conditions on the shared surfaces. This fact is useful when later investigating field propagation in the TEM cell, where a separation of regions significantly simplifies the analysis. Applying Green's second identity to Poisson's equation provides a means of enforcing such a boundary condition upon the surrounding surface  $S$  of a volume  $V$  [1, p. 511, 8, p. 57],

$$\iiint_V (\phi \nabla_{\mathbf{x}'}^2 G - G \nabla_{\mathbf{x}'}^2 \phi) dv' = \oint_S \left( \phi \frac{\partial G}{\partial n} - G \frac{\partial \phi}{\partial n} \right) d\mathbf{s}'. \quad (3.10)$$

Let  $\mathbf{n}$  denote the unit outward normal vector to the surface  $S$ , and let  $\frac{\partial}{\partial n}$  denote the corresponding normal derivative  $\nabla G \cdot \mathbf{n} = \frac{\partial G}{\partial n}$ . The operator  $\nabla_{\mathbf{x}'}^2$  differentiates with respect to the source vector  $\mathbf{x}'$  due to  $x', y', z'$  being the integrands. Inserting  $\nabla^2 \phi = -\rho/\epsilon$  from (3.8a) and  $\nabla^2 G = -\delta$  from (3.5) leads to [8, p. 58]

$$\phi = \frac{1}{\epsilon} \iiint_V \rho(\mathbf{x}') G(\mathbf{x}, \mathbf{x}') dv' + \oint_S \left( G \frac{\partial \phi}{\partial n} - \phi \frac{\partial G}{\partial n} \right) d\mathbf{s}'. \quad (3.11)$$

The scalar potential  $\phi$  or its normal derivative to the surface,  $\partial\phi/\partial n$ , can be specified on the boundary. If only one of these quantities is known on the boundary surface, the Green's function can be adapted so that the unknown quantity vanishes. When  $\phi$  is defined over the entire boundary, Dirichlet boundary conditions are satisfied. Conversely, when  $\partial\phi/\partial n$  is defined over the entire boundary, Neumann boundary conditions apply [8, pp. 55-59].

### 3.2.2 Dyadic Green's Function

While the scalar Green's function is effective for solving one-dimensional differential equations, the dyadic Green's function  $\bar{\mathbf{G}}$  is more appropriate for addressing three-dimensional problems. In general, the dyadic Green's function relates a vector source to a vector response. This is demonstrated when solving the vector Helmholtz equation, as shown in [8, p. 91]

$$\nabla^2 \mathbf{A} + k^2 \mathbf{A} = -\mu \mathbf{J}. \quad (3.12)$$

When  $\mu \mathbf{J}$  is replaced by a unit vector source  $(\hat{\mathbf{a}}_x + \hat{\mathbf{a}}_y + \hat{\mathbf{a}}_z) \delta(\mathbf{x} - \mathbf{x}')$ , the solution for  $\mathbf{A}$  in (3.12) in free space is

$$(\hat{\mathbf{a}}_x + \hat{\mathbf{a}}_y + \hat{\mathbf{a}}_z) \frac{e^{-jk|\mathbf{x}-\mathbf{x}'|}}{4\pi|\mathbf{x}-\mathbf{x}'|}. \quad (3.13)$$

By definition, this constitutes a vector Green's function [8, pp. 91-92].

Each component of the current distribution  $\mathbf{J}$  generates fields through a linear relation. This relationship can effectively be represented by dyadics, which are linear mappings between vectors. The dyadic Green's function is therefore introduced and defined as

$$\begin{aligned} \bar{\mathbf{G}} = & G_{xx} \hat{\mathbf{a}}_x \hat{\mathbf{a}}_x + G_{xy} \hat{\mathbf{a}}_x \hat{\mathbf{a}}_y + G_{xz} \hat{\mathbf{a}}_x \hat{\mathbf{a}}_z + \\ & G_{yx} \hat{\mathbf{a}}_y \hat{\mathbf{a}}_x + G_{yy} \hat{\mathbf{a}}_y \hat{\mathbf{a}}_y + G_{yz} \hat{\mathbf{a}}_y \hat{\mathbf{a}}_z + \\ & G_{zx} \hat{\mathbf{a}}_z \hat{\mathbf{a}}_x + G_{zy} \hat{\mathbf{a}}_z \hat{\mathbf{a}}_y + G_{zz} \hat{\mathbf{a}}_z \hat{\mathbf{a}}_z. \end{aligned}$$

Each component of the current vector  $\mathbf{J}$  is associated with one unit vector of the Green's function, i.e.  $J_x$  with  $\hat{\mathbf{a}}_x$ ,  $J_y$  with  $\hat{\mathbf{a}}_y$  and  $J_z$  with  $\hat{\mathbf{a}}_z$  [8, p. 92]. Consequently, the field generated by a current component in a given direction is determined by the corresponding column of the dyadic Green's function. For example, if only a current component  $J_x$  is present, the field components  $A_x$ ,  $A_y$ , and  $A_z$  are obtained from the Green's function's elements  $G_{xx}$ ,  $G_{yx}$  and  $G_{zx}$ .

The dyadic Green's function is defined as the solution of

$$\nabla^2 \bar{\mathbf{G}}(\mathbf{x}, \mathbf{x}') + k^2 \bar{\mathbf{G}} = -\bar{\mathbf{I}} \delta(\mathbf{x} - \mathbf{x}'). \quad (3.14)$$

In free space, a commonly used form of the dyadic Green's function is given by [8, p. 92]

$$\bar{\mathbf{G}}(\mathbf{x}, \mathbf{x}') = \bar{\mathbf{I}} \frac{e^{-jk|\mathbf{x}-\mathbf{x}'|}}{4\pi|\mathbf{x}-\mathbf{x}'|}, \quad (3.15)$$

where  $\bar{\mathbf{I}}$  is a unit dyadic. The free-space case is presented here to provide an overview. Dyadic Green's functions can also be derived for bounded geometries, such as waveguides, by implementing appropriate boundary conditions.

The fields  $\mathbf{A}$  generated by arbitrary  $\mathbf{J}$  can be expressed with the dyadic Green's function as

$$\mathbf{A}(\mathbf{x}) = \mu \iiint_V \bar{\mathbf{G}}(\mathbf{x}, \mathbf{x}') \mathbf{J}(\mathbf{x}') d\mathbf{x}'. \quad (3.16)$$

Each component of  $\mathbf{J}$  drives a combination of components in  $\mathbf{A}$ . Dyadics capture this component-wise coupling and simplify the notation [8, p. 92].

### 3.3 Modes in Waveguides

### 3.3.1 Rectangular Waveguides as non-TEM structures

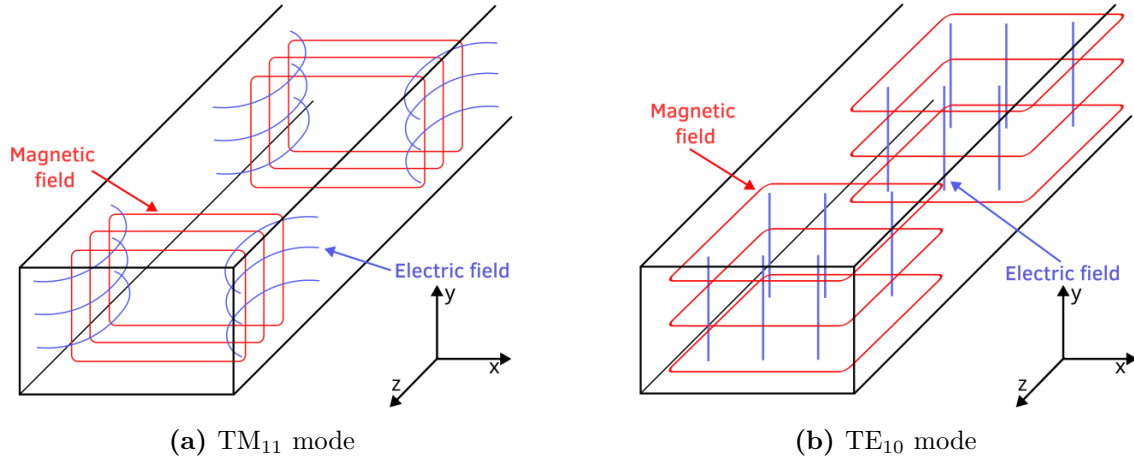


**Figure 3.1** The electric and magnetic fields corresponding to the first dominant TE and TM modes in a rectangular waveguide with perfectly conducting walls.

Waveguides with perfectly conducting walls support only TE and TM modes. The field distributions for the two primary dominant modes are depicted in Figure 3.1.

The physical impossibility of TEM propagation within these structures is a direct consequence of Maxwell's equations. Following the analytical framework established in [11, pp. 425-427], we demonstrate this by first decomposing the electric field intensity  $\mathbf{E}$  and magnetic field intensity  $\mathbf{H}$  into their longitudinal and transverse components, assuming wave propagation in the  $z$ -direction:

$$\mathbf{E} = (E_x \cdot \hat{\mathbf{a}}_x + E_y \cdot \hat{\mathbf{a}}_y + E_z \cdot \hat{\mathbf{a}}_z) e^{-jkz}, \quad (3.17a)$$

$$\mathbf{H} = (H_x \cdot \hat{\mathbf{a}}_x + H_y \cdot \hat{\mathbf{a}}_y + H_z \cdot \hat{\mathbf{a}}_z) e^{-jkz}. \quad (3.17b)$$

Next, applying Faraday's and Ampère-Maxwell law to (3.17a) and (3.17b) yields [11, p. 426]

$$\nabla \times \mathbf{E} = \begin{pmatrix} \frac{\partial}{\partial y} E_z - jk E_y \\ jk E_x - \frac{\partial}{\partial x} E_z \\ \frac{\partial}{\partial x} E_y - \frac{\partial}{\partial y} E_x \end{pmatrix} = \begin{pmatrix} -j\omega B_x \\ -j\omega B_y \\ -j\omega B_z \end{pmatrix}, \quad (3.18a)$$

$$\nabla \times \mathbf{B} = \begin{pmatrix} \frac{\partial}{\partial y} B_z - jk B_y \\ jk B_x - \frac{\partial}{\partial x} B_z \\ \frac{\partial}{\partial x} B_y - \frac{\partial}{\partial y} B_x \end{pmatrix} = \begin{pmatrix} \frac{j\omega}{\mu\epsilon} E_x \\ \frac{j\omega}{\mu\epsilon} E_y \\ \frac{j\omega}{\mu\epsilon} E_z \end{pmatrix}. \quad (3.18b)$$

For a TEM mode, the longitudinal field components vanish  $E_z = H_z = 0$ . Consequently, (3.18a) and (3.18b) reduce to the following conditions for the transverse electric field components:

$$\frac{\partial}{\partial x} E_x + \frac{\partial}{\partial y} E_y = 0 \quad \text{Derived from Gauss' law,} \quad (3.19)$$

$$\frac{\partial}{\partial y} E_x - \frac{\partial}{\partial x} E_y = 0 \quad \text{Derived from Faraday's law.} \quad (3.20)$$

Since the solutions in (3.19) and (3.20) cannot satisfy the rectangular waveguide's boundary conditions, a TEM mode cannot propagate.

### 3.4 TEM mode in the TEM cell<sup>3</sup>

In contrast to the rectangular waveguide, a TEM cell supports the propagation of TEM waves. Moreover, the TEM mode is inherently excited by the geometry of the TEM cell, and is therefore referred to as the essential mode. Higher-order TE and TM modes, which arise only due to non-uniformities in the TEM cell, are termed non-essential modes [17].

The TEM mode in the TEM cell is derived using a procedure presented in [34, 36]. This approach involves determining the Green's function for the longitudinal field components,  $H_z$  and  $E_z$ , of both the TE and TM modes in a rectangular waveguide. The Green's function satisfies the wave equations and boundary conditions of the waveguide, and is constructed as described in Section 3.2.1, with

$$(\nabla^2 + k_t^2)G_j(\mathbf{x}_t, \mathbf{x}'_t) = -\delta(\mathbf{x}_t - \mathbf{x}'_t), \quad (3.21a)$$

$$\frac{\partial G_j(\mathbf{x}_t, \mathbf{x}'_t)}{\partial n} = 0. \quad (3.21b)$$

The wave number is separated into transverse and longitudinal components,  $k^2 = k_t^2 + k_z^2$ . Equation (3.21b) specifies the boundary conditions on the perfectly conducting walls and septum of the TEM cell, as well as on the gaps, as illustrated in Figure 3.2. The index  $j$  indicates the chamber to which the Green's function applies ( $j = 1$  for the upper chamber,  $j = 2$  for the lower chamber). The source points are denoted by  $\mathbf{x}'_t = (\hat{\mathbf{a}}_x x' + \hat{\mathbf{a}}_y y')$ , and the observation points by  $\mathbf{x}_t = (\hat{\mathbf{a}}_x x + \hat{\mathbf{a}}_y y)$ . These coordinates are transformed to depend on the wave number  $k$  instead of the  $z$ -coordinate, which significantly simplifies the derivation of the Green's function, as only a two-dimensional surface must be considered.

The waveguide is excited by an infinitesimal electric dipole moment, centrally located and oriented along the  $y$ -axis. Solving for  $H_z$  and applying Green's second identity yields [36, p. 5]

---

<sup>3</sup>This section follows closely the treatment in: P. F. Wilson et al., *Excitation of a TEM cell by a Vertical Electric Hertzian Dipole*, National Bureau of Standards, 1981

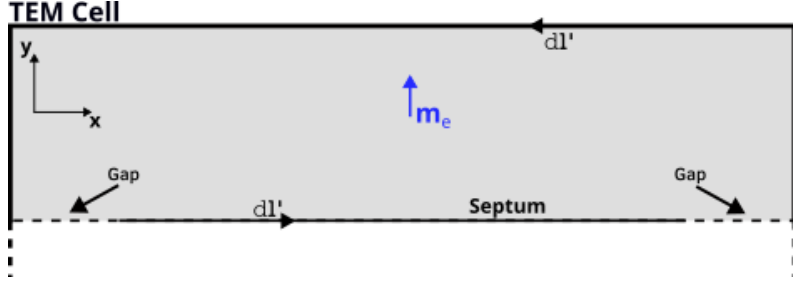


**Figure 3.2** In this analysis, the Green's function determines the fields within the cross-sectional surface  $S$  of the TEM cell, which is shown in light gray and bounded by  $l$ . The source exciting these fields is a centrally located electric dipole moment,  $\mathbf{m}_e$ .

$$\int_l \left( G_j(\mathbf{x}_t, \mathbf{x}'_t) \frac{\partial H_z(\mathbf{x}_t)}{\partial n} - H_z(\mathbf{x}'_t) \frac{\partial G_j(\mathbf{x}_t, \mathbf{x}'_t)}{\partial n} \right) d\mathbf{l}' = \quad (3.22)$$

$$= H_z(\mathbf{x}_t) - \int_S G_j(\mathbf{x}_t, \mathbf{x}'_t) \frac{\partial J_y(\mathbf{x}'_t)}{\partial x'} d\mathbf{s}', \quad (3.23)$$

Here,  $S$  denotes the waveguide cross-section and  $l$  its boundary. Applying the boundary condition (3.21b) to the perfectly conducting septum and walls reduces the boundary integrals to those over the gaps. The electric dipole is then substituted into (3.23), and continuity of  $H_z$  and  $\partial H_z / \partial y$  across these gaps is enforced. The normal vector in the gap region is oriented along the  $y$ -direction,  $n = \pm \mathbf{y}$ . Accordingly, the line element in the integrand becomes  $d\mathbf{l}' = dx'$ . The right-hand side of (3.23) is integrated by parts. Finally, assuming that the electric dipole moment is located in the upper chamber, only  $G_1$  needs to be considered. For the boundary, a combined Green's function accounts for field continuity between the chambers  $G(x, x') = G_1(x, 0, x', 0) + G_2(x, 0, x', 0)$ . Altogether, this yields [36, pp. 5-6]

$$\int_{\text{gaps}} G(x, x') \frac{\partial H_z(x', 0)}{\partial y'} dx' = -\mathbf{m}_e \frac{\partial G_1(x, 0, \mathbf{x}'_t)}{\partial x'}. \quad (3.24)$$

Solving for the Green's function  $G$  provides a solution for the longitudinal magnetic field intensity  $H_z$  of the TE mode. An analogous procedure can be used to determine the longitudinal electric field intensity  $E_z$  of the TM mode. As shown in [36], the total field distribution is then given by the superposition of the TE and TM mode fields, thereby demonstrating the excitation of the TEM mode. The transverse fields  $\mathbf{E}_t$  and  $\mathbf{H}_t$  can then be derived from the longitudinal field components  $H_z$  and  $E_z$ . They are related to  $H_z$  by [36, p. 3]

$$\mathbf{E}_t(\mathbf{x}_t) = \frac{j\omega\mu_0}{k_t^2} \nabla_t H_z(\mathbf{x}_t) \times \hat{\mathbf{a}}_z, \quad (3.25a)$$

$$\mathbf{H}_t(\mathbf{x}_t) = -\frac{jk_z}{k_t^2} \nabla_t H_z(\mathbf{x}_t), \quad (3.25b)$$

and to  $E_z$  by

$$\mathbf{E}_t(\mathbf{x}_t) = -\frac{jk_z}{k_t^2} \nabla_t E_z(\mathbf{x}_t), \quad (3.26a)$$

$$\mathbf{H}_t(\mathbf{x}_t) = \frac{-j\omega\epsilon_0}{k_t^2} \nabla_t E_z(\mathbf{x}_t) \times \hat{\mathbf{a}}_z, \quad (3.26b)$$

where  $\nabla_t = \hat{\mathbf{a}}_x \partial/\partial x + \hat{\mathbf{a}}_y \partial/\partial y$  denotes the transverse gradient operator.

### 3.4.1 Higher-order modes

To determine the usable frequency range of the TEM cell shown in Figure 3.4, the cutoff frequencies of its higher-order modes are examined. Among these, the TE<sub>10</sub> and TE<sub>01</sub> modes are of primary interest as they exhibit the lowest cutoff frequencies. Their transverse electric field distributions are illustrated in Figure 3.3, while Figure 3.6 shows the electric and magnetic field distributions along the TEM cell for each mode. As shown there, the TEM mode exhibits the highest phase velocity, reflected in the large number of periods along the cell, and its magnetic field has no longitudinal component. In contrast, the TE<sub>01</sub> and TE<sub>10</sub> modes possess longitudinal magnetic field components. For the TE<sub>01</sub> mode, these are concentrated near the side walls and are therefore not directly shown in Figure 3.6. For a thin septum ( $t/b \ll 0.1$ ), the cutoff frequencies of modes with even  $n$

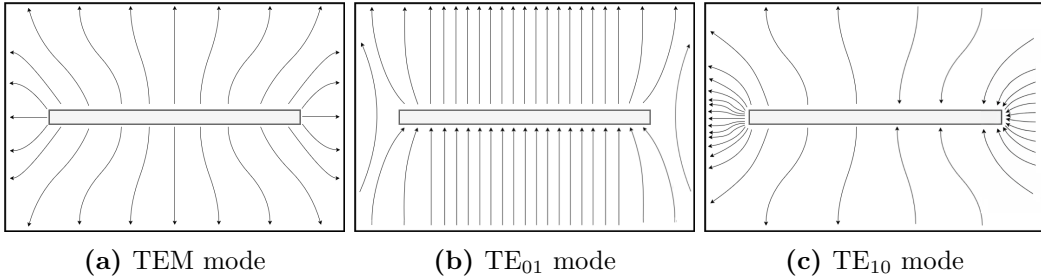


**Figure 3.3** Transverse electric field distributions in the cross section of the TEM cell.

subscripts, i.e. TE<sub>m,2n</sub> and TM<sub>m,2n</sub> modes, can be approximated by the cutoff frequency expression for rectangular waveguides [35]

$$f_c = \frac{c}{2} \sqrt{\left(\frac{m}{a}\right)^2 + \left(\frac{n}{b}\right)^2}, \quad (3.27)$$

where  $c$  is the speed of light, and  $m \geq 0$  and  $n \geq 0$  are the integer mode indices along the  $a$ - and  $b$ -directions, respectively. Applying (3.27) to a TEM cell with  $a = 40$  mm,  $b = 24$  mm,  $g = 5$  mm, and  $t = 0.1$  mm yields the cutoff frequency of the TE<sub>10</sub> mode of  $f_{c,10} = 3.75$  GHz. For modes with odd  $n$  subscripts, such as the TE<sub>01</sub> mode, analytical approximations are given in [39]. Although omitted here due to their complexity, these expressions yield  $f_{c,01} = 3.12$  GHz for the TE<sub>01</sub> mode.

To validate the analytically derived cutoff frequencies, the forward transmission coefficients  $S_{12}$  between the output ports of the TEM cell are computed numerically over frequency and shown in Figure 3.5. The cutoff frequency  $f_c$  is identified as the lowest frequency at which undisturbed mode propagation occurs, corresponding to  $S_{12} = 0$  dB. The numerically

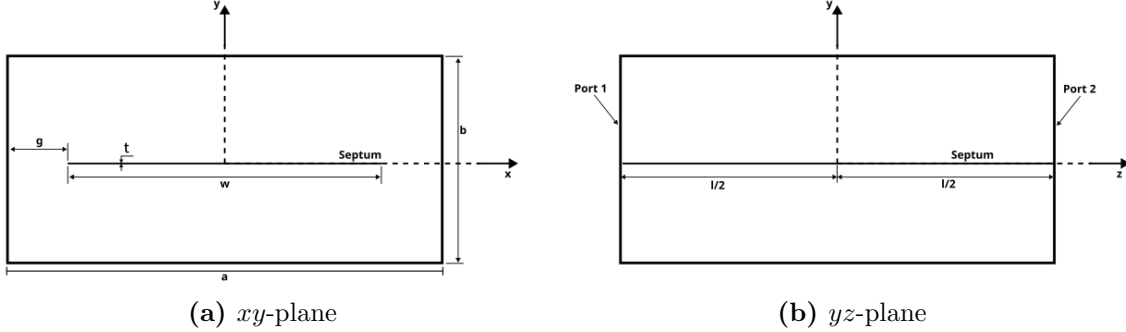


**Figure 3.4** Geometrical arrangement of the TEM cell, demonstrated with cross sections in the  $xy$ -plane and the  $yz$ -plane.

determined cutoff frequencies of the  $TE_{10}$  and  $TE_{01}$  modes,  $f_{c,10} = 3.75$  GHz and  $f_{c,01} = 3.12$  GHz, agree well with the analytical values obtained from (3.27) and [39], respectively.

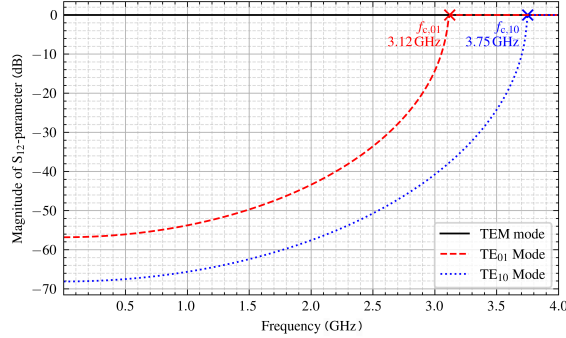


**Figure 3.5** Forward transmission coefficients  $S_{12}$  of the TEM,  $TE_{01}$ , and  $TE_{10}$  modes in the TEM cell over frequency.

Once these higher-order modes are excited, their behavior is governed by the tapered sections at the output ports of the TEM cell. While the TEM mode propagates through these transitions with negligible reflection, higher-order TE and TM modes are reflected at the tapers. Consequently, the TEM cell acts as a high- $Q$  cavity resonator for these modes, with resonances occurring at electrical lengths of  $\frac{\lambda}{2}$  and its integer multiples [35]. Numerical investigations of TEM cell models including tapered sections are presented in [17], while analytical approximations of the resulting resonance frequencies are given in [35]. As the further investigations in this thesis focus on mode propagation independent of the tapered sections, the latter are omitted from the simulation models and Figure 3.4.

In a physical TEM cell, wave propagation in the TEM mode may excite higher-order TE and TM modes due to material discontinuities or finite conductivity of the conducting plates [18]. Such discontinuities force the electric and magnetic fields to develop a component in the direction of propagation, thereby exciting TE and TM modes and introducing measurement uncertainties. These uncertainties are absent in numerical analysis, which

is one of the key reasons why simulation is preferred over measurements with a physical TEM cell in this thesis.

Table 3.1 lists the cutoff frequencies of the TE<sub>01</sub> and TE<sub>10</sub> modes determined numerically and analytically for different TEM cell dimensions. The remainder of this thesis focuses on a TEM cell with  $a = 40$  mm and  $b = 24$  mm, for which the cutoff frequencies are  $f_{c,01} = 3.12$  GHz and  $f_{c,10} = 3.75$  GHz, respectively.

$a$ (mm)	$b$ (mm)	TE <sub>01</sub> $f_c$ (GHz)	TE <sub>10</sub> $f_c$ (GHz)
80	24	1.89	2.05
40	24	3.12	3.75
40	48	2.10	3.75

**Table 3.1** Cutoff frequencies of the TE<sub>01</sub> and TE<sub>10</sub> modes for different TEM cell dimensions, derived both through numerical simulation and analytical calculation. The results of these separate methods agree within the precision shown. As expected from (3.27), the TE<sub>10</sub> cutoff frequency depends only on  $a$  and is independent of  $b$ , consistent with rectangular waveguide theory. The TE<sub>01</sub> cutoff frequency varies with both  $a$  and  $b$ .

### 3.4.2 Field distributions

The normalized electric field intensity of the TEM mode is given as  $\mathbf{e}_{\text{TEM}}^{\pm} = e_{\text{TEM},x}^{\pm} \hat{\mathbf{a}}_x + e_{\text{TEM},y}^{\pm} \hat{\mathbf{a}}_y + e_{\text{TEM},z}^{\pm} \hat{\mathbf{a}}_z$  and normalized to  $\sqrt{W}$ . The  $x$ - and  $y$ -component of  $\mathbf{e}_{\text{TEM}}^{\pm}$  are analytically approximated by

$$e_{\text{TEM},x}^{\pm} = \frac{4}{a} Z_w^{1/2} \sum_{m_o=1}^{\infty} \frac{\sinh M(b/2 - py)}{\sinh Mb/2} \cdot \sin Mx \sin Ma/2 J_0(Mg), \quad (3.28a)$$

$$e_{\text{TEM},y}^{\pm} = p \frac{4}{a} Z_w^{1/2} \sum_{m_o=1}^{\infty} \frac{\cosh M(b/2 - py)}{\sinh Mb/2} \cdot \cos Mx \sin Ma/2 J_0(Mg). \quad (3.28b)$$

$Z_w$  denotes the characteristic impedance of the TEM cell output port,  $a$  its width and  $b$  its height. The sign-function is defined as  $p = 1$  above the septum and  $p = -1$  below it. The parameter  $M = m_o \pi / 2a$ , and  $g$  denotes the gap width between the septum and the conducting wall. The index  $m_o = 1, 3, 5, \dots$  iterates over odd integers. Both expressions are derived in [36] using the procedure described in Section 3.4. Analytical expressions for higher-order modes are provided in [34] and not investigated further in this thesis.

In case of higher-order modes propagating, the analysis of the field distribution is conducted with the following assumptions. Each of the propagating modes is assumed to be orthogonal to each other,

$$\iint \mathbf{e}_n^{\pm} \times \mathbf{h}_m^{\pm} d\mathbf{s}' = 0 \quad \text{if } n \neq m, \quad (3.29)$$

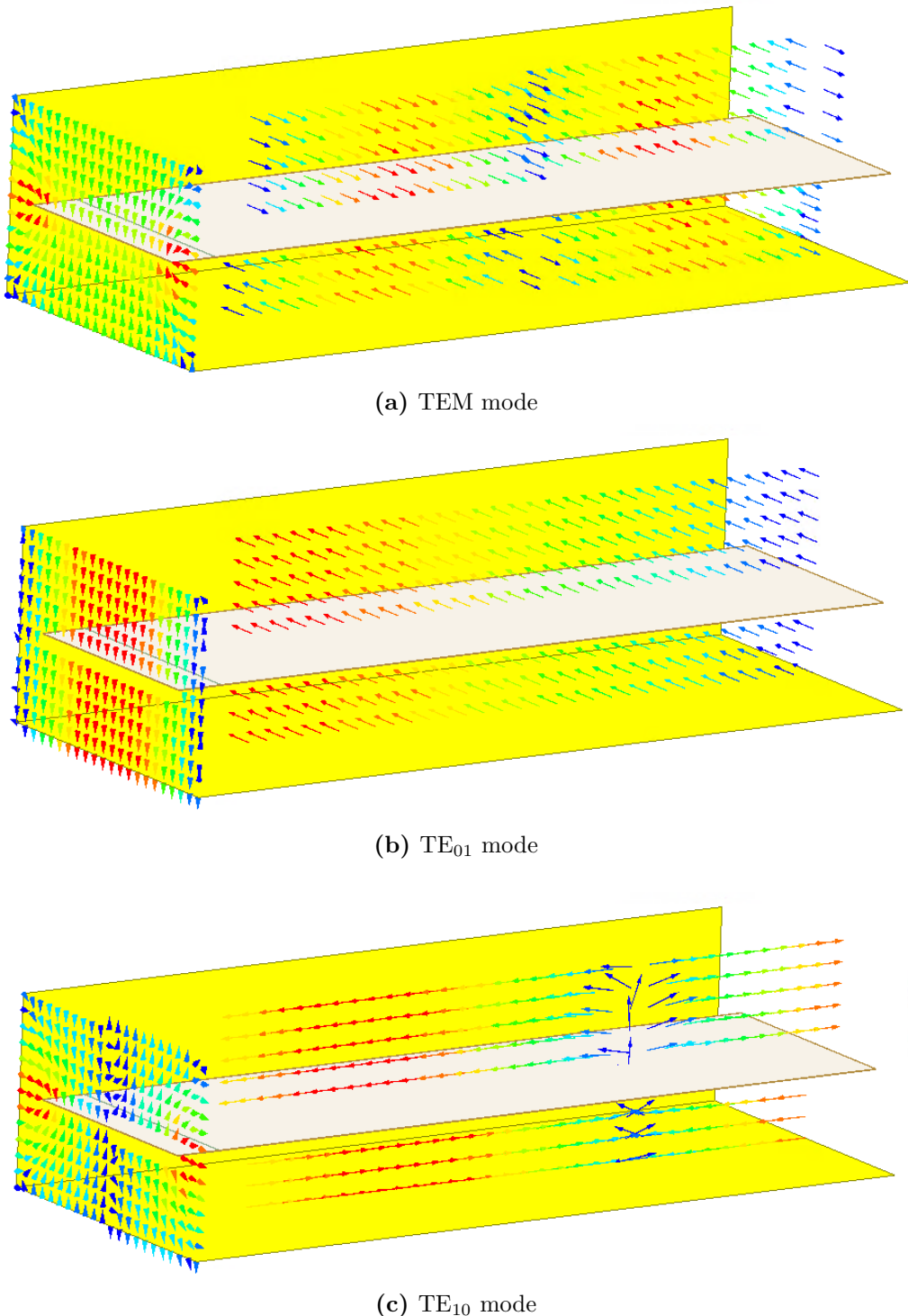


**Figure 3.6** Electric and magnetic field distributions of the TEM, TE<sub>01</sub>, and TE<sub>10</sub> modes in the TEM cell. The magnetic fields are shown along the full length of the cell, while the electric fields are shown at the ports only.

with  $\mathbf{e}_n^\pm$  and  $\mathbf{h}_n^\pm$  being the function vectors of the normalized electric and magnetic field intensities of the  $n$ -th mode in transverse direction [8, p. 359]. This indicates that the modes do not couple with each other, which is the case in a uniform waveguide with perfectly conducting walls, as discussed in Section 3.4.1. Furthermore, each mode is normalized to  $\sqrt{W}$  as shown by

$$\iint \mathbf{e}_n^\pm \times \mathbf{h}_n^\pm ds' = 1. \quad (3.30)$$

Throughout, the superscripts ‘+’ and ‘−’ denote propagation along the positive and negative  $z$ -direction, respectively. The radiated fields along the positive  $z$ -direction can be described by a summation of normal modes, as in [8, p. 360]

$$\mathbf{E}^+ = \sum_n a_n \mathbf{e}_n^+, \quad (3.31a)$$

$$\mathbf{H}^+ = \sum_n a_n \mathbf{h}_n^+. \quad (3.31b)$$

The fields propagating along the negative  $z$ -direction are expressed by [8, p. 360]

$$\mathbf{E}^- = \sum_n b_n \mathbf{e}_n^-, \quad (3.32a)$$

$$\mathbf{H}^- = \sum_n b_n \mathbf{h}_n^-, \quad (3.32b)$$

where  $\mathbf{h}_n^\pm$  is the normalized magnetic field intensity. The model expansion coefficients for the forward and backward propagating waves,  $a_n$  and  $b_n$ , have units of  $\sqrt{W}$  and weight  $\mathbf{e}_n^\pm$  and  $\mathbf{h}_n^\pm$  of the corresponding mode. The field intensities at the outputs  $\mathbf{E}^\pm$  and  $\mathbf{H}^\pm$  are therefore decomposed into several propagating mode fields, each weighted with the corresponding coefficients. The derivation of  $a_n$  and  $b_n$  is discussed in Section 3.5.

The normalized magnetic field intensity  $\mathbf{h}_n^\pm$  is derived in an analogous manner to  $\mathbf{e}_n^\pm$ . For the TEM mode,  $\mathbf{h}_{\text{TEM}}^\pm$  can also be directly obtained from  $\mathbf{e}_{\text{TEM}}^\pm$  with

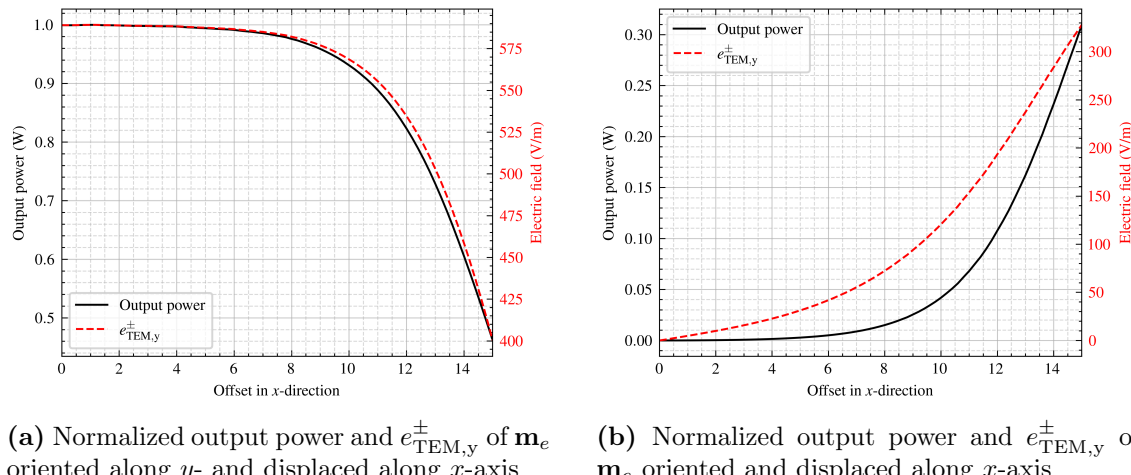
$$\mathbf{h}_{\text{TEM}}^\pm = \pm \frac{1}{\eta_0} \hat{\mathbf{a}}_z \times \mathbf{e}_{\text{TEM}}^\pm, \quad (3.33)$$

where  $\eta_0 \approx 377 \Omega$  is the free-space wave impedance.

The normalized electric field intensity  $\mathbf{e}_{\text{TEM}}^\pm$  of the TEM mode is a key parameter for determining the coupling between a source and the output ports of the TEM cell, as derived using the Lorentz reciprocity theorem discussed in Section 3.1. For example, Figure 3.7a shows the output power generated by an electric dipole moment  $\mathbf{m}_e$  oriented along the  $y$ -direction. The dipole is displaced along the  $x$ -axis at the center height between

the septum and the upper wall of the TEM cell, which has a width of  $a = 40$  mm and a height of  $b = 24$  mm.

The normalized electric field component in the  $y$ -direction  $e_{\text{TEM},y}^{\pm}$  reaches its maximum magnitude at the center of the TEM cell, according to (3.28b). The integral form of the Lorentz reciprocity theorem in (3.2) states that this results in the largest output power. This behavior is confirmed by the results shown in Figure 3.7a. Analogously, the output power shown in Figure 3.7b is largest close to the TEM cell wall if the dipole moment is oriented in the  $x$ -direction. Analysis of the field distribution is therefore useful to explain coupling behavior of electrically small antennas or dipole moments displaced within the TEM cell.



(a) Normalized output power and  $e_{\text{TEM},y}^{\pm}$  of  $\mathbf{m}_e$  oriented along  $y$ - and displaced along  $x$ -axis

(b) Normalized output power and  $e_{\text{TEM},y}^{\pm}$  of  $\mathbf{m}_e$  oriented and displaced along  $x$ -axis

**Figure 3.7** Output power and  $e_{\text{TEM}}^{\pm}$  for different electric dipole moment positions and orientations.

For this reason, Figure 3.8 shows the normalized electric field intensity in the TEM cell for both the  $x$ - and  $y$ -direction.

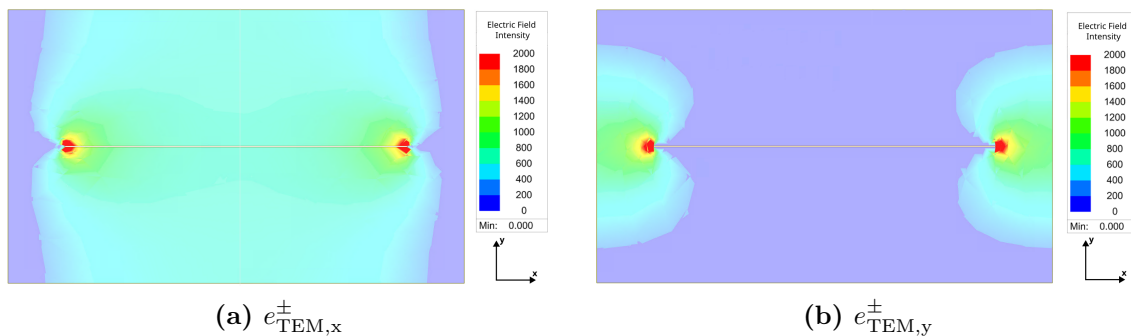


**Figure 3.8** The normalized electric field distribution  $e_{\text{TEM}}^{\pm}$  in the TEM cell excited with an input power of  $1/2$  W at a frequency of 3 GHz.

The normalized electric field of the TEM mode at  $x = 0$  is constant along the  $y$ -axis, as confirmed by both the analytical result of (3.28b) and numerical simulation. For a TEM

cell width  $a = 40$  mm and height  $b = 24$  mm, this field equals  $\mathbf{e}_{\text{TEM}}^{\pm} = 589.25 \text{ V/m } \hat{\mathbf{a}}_y$ .

### 3.5 Radiating Sources in TEM Cells

#### 3.5.1 Arbitrary source

Suppose a current  $\mathbf{J}_1$  excites the TEM cell, as shown in Figure 3.9. Normally, such a current would require external fields to drive it, however, these are neglected here. Only the fields  $\mathbf{E}$  and  $\mathbf{H}$  radiated by  $\mathbf{J}_1$  are considered. These fields satisfy Maxwell's equations [8, p. 360]:

$$\nabla \times \mathbf{E} = -j\omega\mu_0 \mathbf{H}, \quad (3.34a)$$

$$\nabla \times \mathbf{H} = j\omega\epsilon_0 \mathbf{E} + \mathbf{J}_1. \quad (3.34b)$$

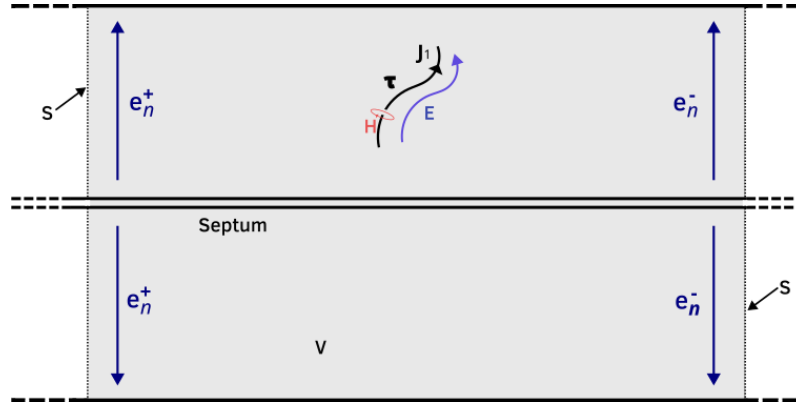


**Figure 3.9** TEM cell with an arbitrary current source  $\mathbf{J}_1$  along the line  $\tau$ .  $\mathbf{E}$  and  $\mathbf{H}$  are the field intensities induced by the current.  $\mathbf{e}_n^+$  and  $\mathbf{e}_n^-$  are outgoing fields towards both output ports of the TEM cell.  $\mathbf{S}$  indicates the surface, and  $V$  the volume of the domain in question.

Applying the integral form of the Lorentz reciprocity theorem in (3.2) with  $\mathbf{J}_2 = \mathbf{M}_1 = \mathbf{M}_2 = 0$  yields

$$\iint_S (\mathbf{e}_n^{\pm} \times \mathbf{H} - \mathbf{E} \times \mathbf{h}_n^{\pm}) d\mathbf{s}' = \iiint V \mathbf{J}_1 \cdot \mathbf{e}_n^{\pm} dv'. \quad (3.35)$$

Using the modal expansions (3.31a) to (3.32b) for the fields  $\mathbf{E}$  and  $\mathbf{H}$  radiated by  $\mathbf{J}_1$  leads to

$$\begin{aligned}
& \iint_S (\mathbf{e}_n^+ \times \mathbf{H} - \mathbf{E} \times \mathbf{h}_n^+) d\mathbf{s}' = \\
&= \iint_S (\mathbf{e}_n^+ \times \sum_m a_m \mathbf{h}_m^+ - \sum_m a_m \mathbf{e}_m^+ \times \mathbf{h}_n^+) d\mathbf{s}' \\
&= \sum_m a_m \iint_S (\mathbf{e}_n^+ \times \mathbf{h}_m^+ - \mathbf{e}_m^+ \times \mathbf{h}_n^+) d\mathbf{s}'.
\end{aligned} \tag{3.36}$$

Due to the orthogonality condition in (3.29) and the normalization in (3.30), the coefficients of each mode can be evaluated separately with

$$\begin{aligned}
& \iint_S (\mathbf{e}_n^+ \times \mathbf{H} - \mathbf{E} \times \mathbf{h}_n^+) d\mathbf{s}' = \\
&= a_n \iint_S (\mathbf{e}_n^+ \times \mathbf{h}_n^+ - \mathbf{e}_n^+ \times \mathbf{h}_n^+) d\mathbf{s}' = -2a_n.
\end{aligned} \tag{3.37}$$

The coefficient  $b_n$  of the fields  $\mathbf{e}_n^-$  and  $\mathbf{h}_n^-$  is evaluated in the same manner:

$$b_n = -\frac{1}{2} \iiint \mathbf{J}_1 \cdot \mathbf{e}_n^- dv' \tag{3.38}$$

Assuming only the TEM mode can propagate, combining (3.30) with the fields  $\mathbf{e}_{\text{TEM}}$  and  $\mathbf{h}_{\text{TEM}}$  with their respective coefficients  $a_{\text{TEM}}$ ,  $b_{\text{TEM}}$  leads to [38]

$$P_{\text{out1}} = \iint_S \langle \mathbf{S} \rangle d\mathbf{s}' = \iint_S \frac{1}{2} \Re \{ (a \cdot \mathbf{e}_{\text{TEM}}^\pm) \times (a \cdot \mathbf{h}_{\text{TEM}}^\pm)^* \} d\mathbf{s}' = \frac{|a_{\text{TEM}}|^2}{2}, \tag{3.39a}$$

$$P_{\text{out2}} = \iint_S \langle \mathbf{S} \rangle d\mathbf{s}' = \iint_S \frac{1}{2} \Re \{ (b \cdot \mathbf{e}_{\text{TEM}}^\pm) \times (b \cdot \mathbf{h}_{\text{TEM}}^\pm)^* \} d\mathbf{s}' = \frac{|b_{\text{TEM}}|^2}{2}. \tag{3.39b}$$

The Poynting vector  $\langle \mathbf{S} \rangle$  of the TEM mode in Equations (3.39a) to (3.39b) does not have an imaginary component,

$$\langle \mathbf{S} \rangle = \mathbf{e}_{\text{TEM}}^\pm \times \mathbf{h}_{\text{TEM}}^\pm = \Re \{ \mathbf{e}_{\text{TEM}}^\pm \times (\mathbf{h}_{\text{TEM}}^\pm)^* \}. \tag{3.40}$$

Equations (3.39a) to (3.39b) demonstrate that the coefficients  $a_{\text{TEM}}$  and  $b_{\text{TEM}}$  are directly related to the output power. Consequently, the output power can be directly linked to the electric and magnetic field distribution of the TEM mode, and vice versa.

### 3.5.2 Equivalent dipole moments

Equations (2.2) and (3.35) relate the electric dipole moment  $\mathbf{m}_e$  with a given source current  $\mathbf{J}_1$  flowing through an infinitesimal wire, yielding [32]

$$\begin{pmatrix} a_n \\ b_n \end{pmatrix} = -\frac{1}{2} \mathbf{m}_e \cdot \mathbf{e}_n^\pm. \quad (3.41)$$

If this arbitrary current distribution forms an infinitesimal loop, the source can be represented by a magnetic dipole moment  $\mathbf{m}_m$ . This leads to [8]

$$\begin{aligned} \begin{pmatrix} a_n \\ b_n \end{pmatrix} &= - \oint_C \mathbf{e}_n^\pm d\mathbf{l} \\ &= - \iint_S \nabla \times \mathbf{e}_n^\pm ds' \\ &= j\omega\mu_0 \iint_S \mathbf{h}_n^\pm ds' \\ &= j\omega\mu_0 \mathbf{m}_m \cdot \mathbf{h}_n^\pm \end{aligned} \quad (3.42)$$

This formulation assumes that the magnetic field strength  $\mathbf{h}^\pm$  does not change over the loop area. This is the case for electrically small loops. Otherwise, the magnetic field strength  $\mathbf{h}^\pm$  must be considered in the integration process of (3.42) [8].

If several modes are propagating, it is useful to determine the coefficients  $a_n$  and  $b_n$  weighting the modes in (3.31a) and (3.32b). In this case, the orthogonality property in (3.29) can be used to derive [8]

$$2a_n = - \int_C \boldsymbol{\tau} \cdot \mathbf{e}_n^- dl, \quad (3.43a)$$

$$2b_n = \int_C \boldsymbol{\tau} \cdot \mathbf{e}_n^+ dl. \quad (3.43b)$$

The wire follows the curve  $C$ , and  $\boldsymbol{\tau}$  is the tangential vector along that curve.

In the presence of both a magnetic and an electric dipole moment, their contributions can be summed, resulting in [32]

$$\begin{pmatrix} a_n \\ b_n \end{pmatrix} = \frac{1}{2} (-\mathbf{m}_e \cdot \mathbf{e}_n^\pm + j\omega\mu_0 \mathbf{m}_m \cdot \mathbf{h}_n^\pm). \quad (3.44)$$

For the TEM mode, the relation between  $\mathbf{e}_{\text{TEM}}^\pm$  and  $\mathbf{h}_{\text{TEM}}^\pm$  expressed in (3.33) yields a simplified form of (3.44), written as [32]

$$\begin{pmatrix} a_{\text{TEM}} \\ b_{\text{TEM}} \end{pmatrix} = -\frac{1}{2} (\mathbf{m}_e \pm jk\mathbf{m}_m \times \mathbf{z}) \cdot \mathbf{e}_{\text{TEM}}^\pm. \quad (3.45)$$

Equation (3.45) proves useful in later investigations, as it requires knowledge of only  $\mathbf{e}_{\text{TEM}}^{\pm}$  to determine the dipole moments. The complex magnitude of the dipole moments  $m_e$  and  $m_m$  is separately derived by

$$m_e = \frac{a_{\text{TEM}} + b_{\text{TEM}}}{e_{\text{TEM}}^{\pm}}, \quad (3.46a)$$

$$m_m = j \frac{a_{\text{TEM}} - b_{\text{TEM}}}{k_0 e_{\text{TEM}}^{\pm}}. \quad (3.46b)$$

The individual components of the electric field for a given mode  $\mathbf{e}_n^{\pm} = e_{n,x}^{\pm} \cdot \hat{\mathbf{a}}_x + e_{n,y}^{\pm} \cdot \hat{\mathbf{a}}_y + e_{n,z}^{\pm} \cdot \hat{\mathbf{a}}_z$  can be analyzed separately by examining the output power of the TEM cell. For example, the components of  $\mathbf{m}_e$  are derived with

$$m_{ex} = \frac{2\sqrt{P_x}}{e_{n,x}^{\pm}}, \quad (3.47a)$$

$$m_{ey} = \frac{2\sqrt{P_y}}{e_{n,y}^{\pm}}. \quad (3.47b)$$

$P_x$  and  $P_y$  describe the power measured at one output port induced by the respective component of the dipole moment [32].

For the TEM mode, an electric dipole placed in the TEM cell leads to output power with the same phase at both ports. This directly results from the symmetric field distribution of the TEM mode leading to the same  $\mathbf{e}_{\text{TEM}}^{\pm}$  component at the output ports. In contrast, a magnetic dipole results in a phase shift of  $\pm\pi$ . This difference arises from the phase shift of the magnetic fields at the output ports,  $\mathbf{h}_{\text{TEM}}^+$  and  $\mathbf{h}_{\text{TEM}}^-$ , as illustrated in Figure 3.10.

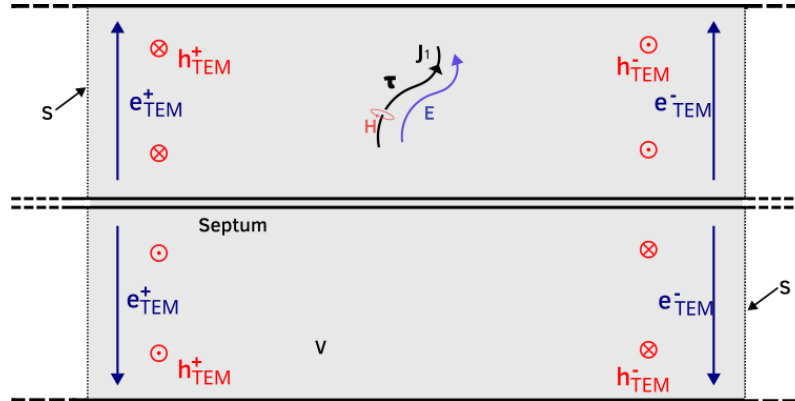


**Figure 3.10** Field distribution of the TEM mode highlighting the out-of-phase magnetic fields at the output ports.

For the next higher-order mode  $\text{TE}_{01}$ , the situation is reversed. An electric dipole moment leads to a phase shift of  $\pm\pi$ , while a magnetic dipole moment produces no phase shift. This behavior is again due to the phase shift occurring now between the electric field

intensities at the output ports,  $\mathbf{e}_{\text{TE01}}^+$  and  $\mathbf{e}_{\text{TE01}}^-$ , while there is no phase shift between the magnetic field intensities,  $\mathbf{h}_{\text{TE01}}^+$  and  $\mathbf{h}_{\text{TE01}}^-$ .

It is assumed that the dipole moments are positioned halfway along the septum in  $z$ -direction. A shift in  $z$ -direction introduces a phase shift between the output port powers, consequently altering the results derived above.

### 3.5.3 Electrically small antennas

The electric field coupling with an electrically small antenna can be expressed as [8, p. 361]

$$2a_n = - \int_C \boldsymbol{\tau} I(l) \cdot \mathbf{e}_n^+ dl. \quad (3.48a)$$

$$2b_n = - \int_C \boldsymbol{\tau} I(l) \cdot \mathbf{e}_n^- dl. \quad (3.48b)$$

Since the antenna is electrically small, the electric field  $\mathbf{e}_n^\pm$  is assumed to be constant in  $C$ . Furthermore, if the current  $I$  is constant along  $C$ , it does not have to be considered in the integration. Integrating over the closed loop simplifies to [8, p. 361]

$$2a_n = - \oint_C \mathbf{e}_n^+ \cdot \boldsymbol{\tau} dl = j\omega\mu_0 \iint_S \mathbf{h}_n^+ d\mathbf{s}' = V_n^+, \quad (3.49a)$$

$$2b_n = - \oint_C \mathbf{e}_n^- \cdot \boldsymbol{\tau} dl = j\omega\mu_0 \iint_S \mathbf{h}_n^- d\mathbf{s}' = V_n^-. \quad (3.49b)$$

The induced voltage  $V_n^+$  is related to the fields  $\mathbf{e}_n^+$  and  $\mathbf{h}_n^+$  at the output port located in positive  $z$ -direction, while the induced voltage  $V_n^-$  is related to the fields at the other output port  $\mathbf{e}_n^-$  and  $\mathbf{h}_n^-$ . For the TEM mode, the total induced voltage equals  $V_{\text{TEM}} = V_{\text{TEM}}^- - V_{\text{TEM}}^+$ . The relation to the magnitude of the magnetic dipole moment  $m_m$  is expressed as

$$m_m = \frac{a_{\text{TEM}} - b_{\text{TEM}}}{e_{\text{TEM}}^\pm \cdot k_0} = \frac{V_{\text{TEM}}}{e_{\text{TEM}}^\pm \cdot k_0}. \quad (3.50)$$

For the TE<sub>01</sub> mode, the total induced voltage equals  $V_{\text{TE01}} = V_{\text{TE01}}^- + V_{\text{TE01}}^+$ .

In the general case, a magnetic dipole moment  $\mathbf{m}_m$  producing fields characterized with coefficients  $a_n$  and  $b_n$  models the magnetic coupling behavior of any electrically small antenna yielding the same coefficients. Consequently, deriving an equivalent magnetic dipole moment  $\mathbf{m}_m$  of an electrically small antenna is possible by measuring  $a_n$  and  $b_n$  at the output ports.

In a similar manner to Equations (3.48a) and (3.48b), a constant magnetic field  $\mathbf{h}_n^\pm$  along a magnetic current  $I_m$  following a curve  $C$  makes the following expression possible:

$$2a_n = - \int_C \boldsymbol{\tau} I_m(l) \cdot \mathbf{h}_n^+ dl, \quad (3.51a)$$

$$2b_n = - \int_C \boldsymbol{\tau} I_m(l) \cdot \mathbf{h}_n^- dl. \quad (3.51b)$$

Analogous to Equations (3.49a) and (3.49b),  $I_m$  is assumed to be constant and  $C$  to form a closed loop, leading to

$$2a_n = - \oint_C \mathbf{h}_n^- \cdot \boldsymbol{\tau} dl = -j\omega\epsilon_0 \iint_{S_0} \mathbf{e}_n^+ d\mathbf{s}', \quad (3.52a)$$

$$2b_n = - \oint_C \mathbf{h}_n^+ \cdot \boldsymbol{\tau} dl = -j\omega\epsilon_0 \iint_{S_0} \mathbf{e}_n^- d\mathbf{s}'. \quad (3.52b)$$

Now, the surfaces  $S_1$  and  $S_2$  are defined, which are depicted in Figure 3.11. Surface  $S_1$  starts from  $S_0$  and runs parallel to the electric field  $\mathbf{e}_n^\pm$ , extending infinitely. A total surface is defined as  $S = S_0 + S_1 + S_2$ , where  $S_2$  closes the total surface around  $S_1$  at infinity.

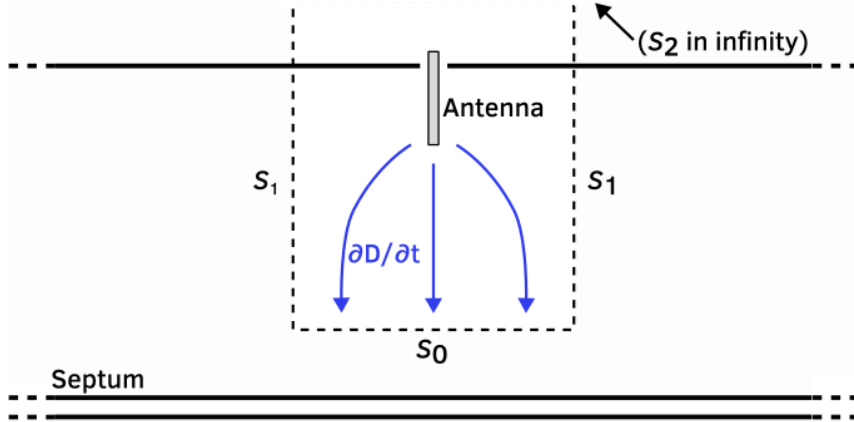


**Figure 3.11** Sketch of the surfaces  $S_0$ ,  $S_1$  and  $S_2$  in the TEM cell with an example antenna, coupling through  $S_0$  to the septum over the displacement current  $\partial\mathbf{D}/\partial t$ .

Consequently, Equations (3.52a) and (3.52b) can be written with the newly defined closed surface  $S$  as

$$j\omega\epsilon_0 \iint_S \mathbf{e}_n^\pm \cdot d\mathbf{s}' = j\omega\epsilon_0 \iint_{S_0} \mathbf{e}_n^\pm \cdot d\mathbf{s}' + \underbrace{j\omega\epsilon_0 \iint_{S_1} \mathbf{e}_n^\pm \cdot d\mathbf{s}'}_{=0} + \underbrace{j\omega\epsilon_0 \iint_{S_2} \mathbf{e}_n^\pm \cdot d\mathbf{S}}_{=0}. \quad (3.53)$$

Inserting Gauss' law  $\nabla \cdot \mathbf{E} = \frac{\rho}{\epsilon_0}$  leads to

$$-j\omega\epsilon_0 \iint_S \mathbf{e}_n^\pm \cdot d\mathbf{s}' = -j\omega\epsilon_0 \iiint_V \nabla \cdot \mathbf{e}_n^\pm \cdot dv' = -j\omega \iiint_V \rho_n^\pm \cdot dv'. \quad (3.54)$$

With the continuity equation  $j\omega\rho = -\nabla \cdot \mathbf{J}$  this yields

$$2a_n = -j\omega \iiint_V \rho_n^+ \cdot dv' = \iiint_V \nabla \cdot \mathbf{J}_n^+ \cdot dv' = \oint_S \mathbf{J}_n^+ \cdot d\mathbf{s}' = I_n^+, \quad (3.55a)$$

$$2b_n = -j\omega \iiint_V \rho_n^- \cdot dv' = \iiint_V \nabla \cdot \mathbf{J}_n^- \cdot dv' = \oint_S \mathbf{J}_n^- \cdot d\mathbf{s}' = I_n^-. \quad (3.55b)$$

For the TEM mode, the electric dipole moment magnitude  $m_e$  can be expressed in terms of the total current  $I_{\text{TEM}} = I_{\text{TEM}}^+ + I_{\text{TEM}}^-$  by substituting (3.55a) and (3.55b) into (3.46a), yielding

$$m_e = \frac{a_{\text{TEM}} + b_{\text{TEM}}}{e_{\text{TEM}}^\pm} = \frac{I_{\text{TEM}}}{e_{\text{TEM}}^\pm}. \quad (3.56)$$

An electric dipole moment  $\mathbf{m}_e$  producing fields characterized with coefficients  $a_n$  and  $b_n$  models the electric coupling behavior of any electrically small antenna yielding the same coefficients. Consequently, deriving an equivalent  $\mathbf{m}_e$  of an electrically small antenna is possible by measuring  $a_n$  and  $b_n$  at the output port, analogous to the case of  $\mathbf{m}_m$ .

The physical meaning of  $I_n$  is the electrical current passing between the septum and the dipole via capacitive coupling, representing the displacement current. In summary, the magnetic dipole moment arises from the induced voltage on the septum, whereas the electric dipole moment results from the coupling displacement current.

## 3.6 Shielding

### 3.6.1 Electromagnetic shielding mechanisms

The following section outlines the fundamental theory of electromagnetic shielding. Throughout this thesis, all materials are assumed to be linear and isotropic.

A commonly used figure of merit for quantifying the shielding capability of a material is the electromagnetic shielding effectiveness  $SE$ . It is defined as the ratio of the incident to the transmitted electric field amplitude, expressed on a logarithmic scale in decibels as in [9, 16, p. 63]

$$SE_{\text{dB}} = 20 \log_{10} \left( \frac{E_i}{E_t} \right), \quad (3.57)$$

where  $E_i$  and  $E_t$  denote the magnitudes of the incident and transmitted electric field, respectively, as shown in Figure 3.12. An analogous expression holds for the magnetic field components. Higher values of  $SE_{\text{dB}}$  indicate greater attenuation of the electromagnetic field.

An electromagnetic wave incident on a shielding material may be partially reflected at the surface, partially absorbed within the material, and reflected multiple times internally before the remainder is transmitted. The total shielding effectiveness is determined by [16, p. 63]

$$SE_{\text{dB}} = R_{\text{dB}} + A_{\text{dB}} + B_{\text{dB}}, \quad (3.58)$$

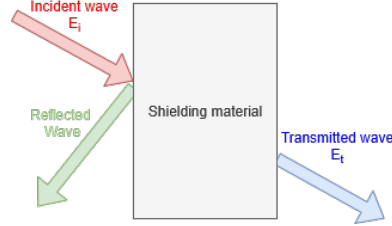


**Figure 3.12** Incident, reflected and transmitted electric field intensities at a shielding material.

according to Schelkunoff's approach to shielding [30]. Absorption losses  $A_{dB}$  arise from waves propagating through the shield,  $R_{dB}$  denotes reflections at the material's surface, and  $B_{dB}$  is a correction factor that accounts for multiple reflections within the shield [9].

Reflections contribute most significantly to a material's shielding effectiveness [16, p. 1]. They are characterized by the reflection coefficient  $R$ . For a material to reflect incident fields, it must possess free charge carriers. For this reason, highly conductive materials, such as metals, reflect the majority of incident electromagnetic waves.

Reflections are caused by wave impedance mismatch between two materials. It is common practice to use the normalized wave impedance  $Z$  to free-space wave impedance  $Z_0$  when determining the reflection coefficient  $R$ . At the interface between free space and a shielding material, this yields [8, p. 183]

$$R = \frac{Z - 1}{Z + 1}. \quad (3.59)$$

The normalized wave impedance is given by

$$Z = \frac{1}{Z_0} \sqrt{\frac{j\omega\mu}{\sigma + j\omega\epsilon}}. \quad (3.60)$$

Electric fields dominate in the near-field region of electric dipoles, as discussed in Section 2.1 and demonstrated with (2.11). Consequently, the wave impedance in this region is very high. For effective shielding by reflection, the shielding material should possess high permittivity and high conductivity to achieve a low impedance (see Equation 3.60), creating the necessary impedance mismatch for reflection [16, p. 67].

In contrast, magnetic fields are predominant in the near-field region of magnetic dipoles, as demonstrated with Section 2.2, specifically with (2.19). A high conductivity shields well against high-frequency magnetic fields due to creation of counter-acting eddy currents [16, p. 112]. Low-frequency magnetic fields are difficult to shield, and the most common approach is the redirection of magnetic flux lines due to high permeability of the shielding material [16, pp. 112-113].

The portion of the electromagnetic wave that is not reflected is subject to absorption within the shielding material. This phenomenon is described by  $A_{dB}$  and accounts for

an exponentially decreasing amplitude of an electromagnetic wave in a lossy medium. In conductive materials, this phenomenon is closely related to the skin depth.

The skin effect describes the interaction of electromagnetic waves with conductors, causing eddy currents to form on the surface. To investigate this phenomenon, the complex wavenumber is introduced  $\tilde{k} = k + j\kappa$ , which assists in mathematically describing waves propagating in lossy materials. The imaginary part  $\kappa$  is expressed as

$$\kappa = \omega \sqrt{\frac{\epsilon\mu}{2}} \left[ \sqrt{1 + \left( \frac{\sigma}{\epsilon\omega} \right)^2} - 1 \right]^{1/2}. \quad (3.61)$$

The skin depth  $d$  is described by

$$d = 1/\kappa. \quad (3.62)$$

For highly conductive materials ( $\sigma \gg \epsilon\omega$ ) the skin depth is  $d \propto 1/\sqrt{\omega}$ . Therefore, high-frequency electromagnetic waves do not penetrate deeply into conductive materials, due to the free electrons associated with high conductivity absorbing the waves with eddy currents on the material's surface and transforming the energy into heat. A material's permeability further reduces the skin depth due to the increased susceptibility to eddy currents [16, p. 104].

For non-conductive materials, absorption depends on the electric loss factor [16, pp. 102-103], as further described in Section 3.6.2.

Upon reaching the far end of the shielding material, re-reflections can occur. When the material thickness is greater than the skin depth, the correction factor for this effect  $B_{dB}$  can be neglected. When the material thickness is smaller than the skin depth, however, the internal reflections reduce the shielding effectiveness by destructively interfering with the reflected waves, and the value of  $B_{dB}$  is negative [16, p. 1].

### 3.6.2 Conductivity, permeability and permittivity in shields

When molecules in a material are exposed to an electric field, they become polarized. This property is characterized by the material's permittivity  $\epsilon$ . Exposure to a magnetic field causes the spins of electrons within atoms to align with the field, described by the material's permeability  $\mu$ . When these electric and magnetic fields vary with time, the molecules continuously move and realign, resulting in the movement of charges, which is quantified by the conductivity  $\sigma$ . The energy lost in this dynamic process is dissipated as heat [2, p. 68].

The electric field pushes charges in polarizable molecules apart. This separation of charges may be described as an electric dipole, depending on the separation distance and the charge. Under alternating electric fields, the movement of charges contributes to  $\sigma$ . This phenomenon is called dielectric hysteresis. It is quantified by the loss tangent  $\tan \delta_e$ , and defined as [2, pp. 73-74]

$$\tan \delta_e = \frac{\sigma_s}{\omega \epsilon'} + \frac{\epsilon''}{\epsilon'}. \quad (3.63)$$

There,  $\sigma_s$  is the static conductivity, indicating the conductivity of the material for constant fields over time. The complex part of the permittivity  $\epsilon''$  describes the lossy part of the dielectric material, specifically relevant for alternating fields over time. The real part of the permittivity is lossless and is noted by  $\epsilon'$ , and corresponds to the material's ability to store electric energy [23]. The overall complex permittivity is therefore  $\epsilon = \epsilon' + j\epsilon''$ .

The loss tangent therefore relates the conductivity of a material to the real permittivity. A dielectric with low losses has a much larger displacement current than conduction current density ( $\tan \delta_e \ll 1$ ). The opposite is true for a good conductor ( $\tan \delta_e \gg 1$ ) [2].

Analogous to polarizable materials, there are also magnetizable lossy materials, which are characterized by a complex permeability  $\mu = \mu' + j\mu''$ . The real part of the permeability  $\mu'$  describes the material's ability to store magnetic energy, while  $\mu''$  describes the magnetic losses [23]. The complex permeability can also be described by a magnetic loss tangent  $\tan \delta_m$ , as shown in

$$\tan \delta_m = \frac{\mu''}{\mu'}. \quad (3.64)$$

The loss tangent is very low for the majority of materials. Ferrites are a notable exception and are commonly used to attenuate high-frequency signals [2, p. 80].

### 3.6.3 ASTM ES7-83 Method

The ASTM ES7-83 method is used to determine the shielding effectiveness of shielding materials in far-field conditions. The shielding material is inserted into a coaxial TEM cell around the septum. Ideally, they form a continuous connection [27].

In this method, two measurements are performed at the output ports of the TEM cell. In the first measurement, an empty TEM cell is excited and a reference output voltage  $U_{\text{ref}}$  is measured. In the second, the TEM cell is loaded with the shielding material, and the output voltage  $U_{\text{load}}$  is again noted. The shielding effectiveness  $SE_{\text{dB}}$  is then derived with the obtained measurement values by [27]

$$SE_{\text{dB}} = 20 \cdot \log \left( \frac{U_{\text{ref}}}{U_{\text{load}}} \right). \quad (3.65)$$

When applying numerical analysis in combination with this method, it is more convenient to define a reference output power  $P_{\text{ref}}$  for an unloaded TEM cell, and an output power for the loaded case  $P_{\text{load}}$ . This leads to similar expression,

$$SE_{\text{dB}} = 10 \cdot \log \left( \frac{P_{\text{ref}}}{P_{\text{load}}} \right). \quad (3.66)$$

Figure 3.13b shows the cross section of this shielding material, which is inserted into the TEM cell. In Figure 3.13a the shielding material can be seen wrapped around the septum.

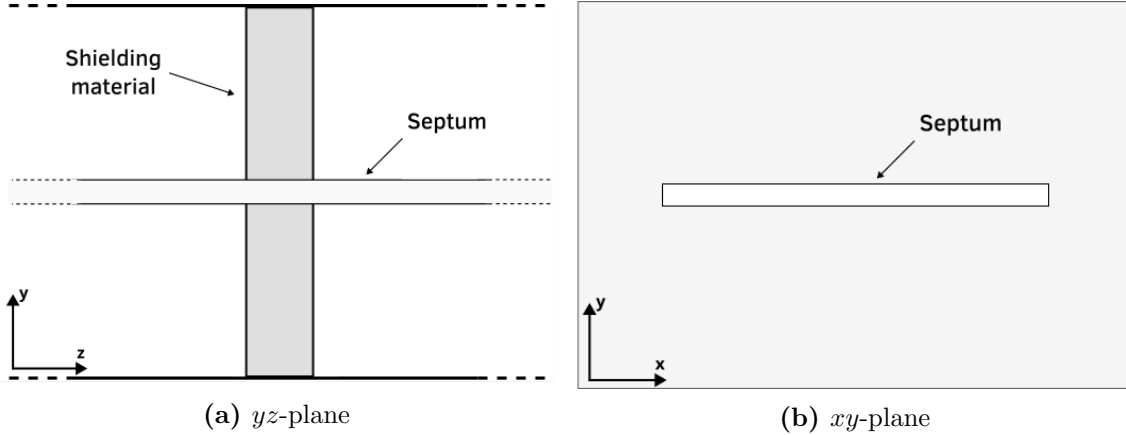


**Figure 3.13** Cross section of shielding material in TEM cell

Then, the S-parameters derived in the simulations are used to determine the output powers  $P_{\text{ref}}$  and  $P_{\text{load}}$ . By exciting the TEM cell with a power of 1 W, the reference power  $P_{\text{ref}} = 1 \text{ W}$ . The measured power is then derived through

$$P_{\text{load}} = P_{\text{ref}} \cdot 10^{S_{12,\text{dB}}/10}. \quad (3.67)$$

### 3.6.4 Dual TEM cell

The shielding effectiveness of a material may also be determined using a dual TEM cell shown in Figure 3.14. The two cells are connected through an aperture, which can be filled with the shielding material or left empty. The upper TEM cell is excited through port 1, and acts as a driving cell, transmitting power through the aperture. Port 2 is loaded with the reference impedance  $Z_w \approx 50 \Omega$ . The second TEM cell functions as a receiver, collecting power at its output ports [27].

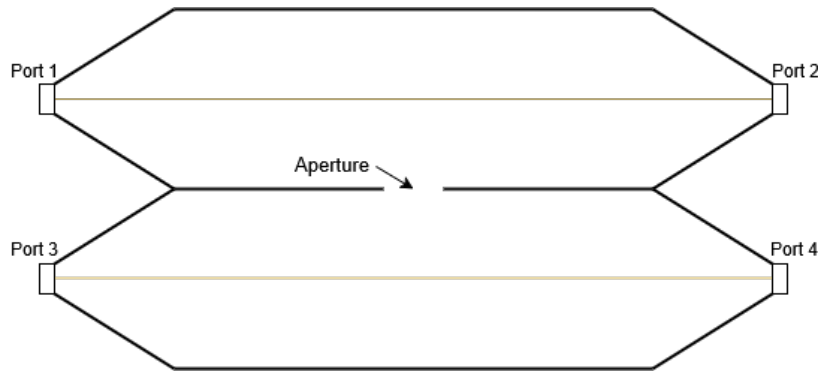


**Figure 3.14** Dual TEM cell with aperture

If the aperture is electrically small, its coupling may be described by an electric and a

magnetic dipole moment. Their magnitude is related to the electric and magnetic coupling between the TEM cells over the aperture. Therefore, the electric and magnetic coupling can be determined separately by adding or subtracting the output powers of the receiving TEM cell [27, 38]. Consequently, an electric shielding effectiveness  $SE_{dB}^e$  and a magnetic shielding effectiveness  $SE_{dB}^m$  can be calculated with

$$SE_{dB}^e = 10 \log \left( \frac{P_{ref,sum}}{P_{load,sum}} \right), \quad (3.68a)$$

$$SE_{dB}^m = 10 \log \left( \frac{P_{ref,diff}}{P_{load,diff}} \right). \quad (3.68b)$$

Separating the electric and magnetic shielding effectiveness is useful when applying shielding materials in the near field of electric or magnetic dipole moments. For shielding a magnetic dipole moment, the  $SE_{dB}^m$  value is considered significant [38], whereas for an electric dipole moment, the  $SE_{dB}^e$  value is relevant.

## 4 Finite Element Method

### 4.1 General Idea

Problems involving the calculations of electromagnetic fields are often cumbersome and difficult to solve. This is due to the need of solving differential equations describing these fields over a computational domain, which is not possible with a computer in this sense. The simulation software Ansys HFSS (High Frequency Simulation Software) aims to provide a solution. This software is used for the simulations in section 4, hence it is described in this following, dedicated section.

HFSS uses a numerical technique, namely the Finite Element Method (FEM). The general idea of FEM after Rayleigh-Ritz-Galerkin is to choose a number of basis functions. The goal is to find a linear combination of these basis functions, so that the differential equation is satisfied as closely as possible. This turns the problem of solving a differential equation into a system of algebraic equations, which the computer can process. There is always a set of basis functions which enable the calculation to converge to the real solution. However, the number of basis functions used in the domain is limited, due to reasons of computability [33].

FEM therefore divides the domain into finite elements, i.e. smaller pieces. Then, within each piece, such a basis function is assigned. A linear combination of these basis functions are found, which satisfy the differential equations. In region where the approximating solution has a high degree of error, the accuracy may be increased by further subdividing the finite elements. This is repeated, until the error falls below a certain threshold, and a precise solution is derived.

### 4.2 Dividing a computational domain into finite elements

The differential equation to be solved is expressed as

$$\nabla \times \left( \frac{1}{\mu_r} \nabla \times \mathbf{E} \right) - k_0^2 \epsilon_r \mathbf{E} = 0 \quad \text{in } \Omega, \quad (4.1)$$

where  $\epsilon_r$  is the relative permeability and  $\mu_r$  is the relative permeability of the material. The variable  $k_0$  is the wave number of free space and equals  $k_0 = \omega \sqrt{\epsilon_0 \mu_0}$ . [7, 24, 6].

This equation is solved in a computational domain  $\Omega$ . This computational domain is divided into finite elements, called a mesh. Each node in this mesh has polynomial functions assigned, which are weighted to approximate the real solution. It has been proven that tetrahedral finite elements are best suited for this task, as they are geometrically flexible and make the definition of complete polynomial approximation functions possible [31]. Ansys HFSS uses a adaptive finite element mesh generator, which automatically provides a mesh for a given 3-dimensional construction. The Delaunay tesselation for three-dimensions is used for generating a mesh. It efficiently creates a mesh from objects of arbitrary shapes. Any boundary condition can be added recursively to the mesh. At the heart of this algorithm lies the property, that the circumsphere of an tetrahedra's vertices may not contain other tetrahedra's vertices.

Figure 4.1 shows one of such tetrahedrons. At the edge points, the components of the field which are normal to the respective edge and tangential to the face of the element is stored. At the vertex points, the component of a field which are tangential to the edges are stored. The value of the field at any midpoint is derived through interpolation from the node values. The basis function is used for interpolation.

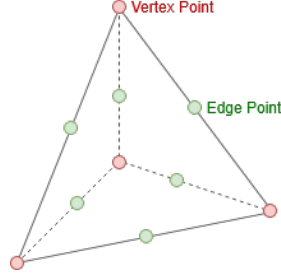


**Figure 4.1** Tetrahedron with points on the edge and vertices.

Because of the way how the fields are stored in the tetrahedra, they are called tangential vector finite elements. Their advantage is that tangential components of fields can be forced to be equal among adjacent tetrahedra at the boundary. For example, an electric field stored at a vertex point must point in the direction along one of the edges, therefore it is tangential to the element. An adjacent element then has the same tangential electric field imposed at this node, leading to a continuous tangential electric field, therefore satisfying the boundary conditions implied by the Maxwell equation automatically. Furthermore, any Dirichlet boundary conditions can easily be set along the edges. [24].

The finite element is described as

$$H_1^{(\dim=3)}(\text{curl}) = \left\{ \mathbf{u} \mid \mathbf{u} \in [L_2(\Omega)]^3, \nabla \times \mathbf{u} \in [P_1(\Omega)]^3 \cap D(\Omega) \right\}, \quad (4.2)$$

where  $L_2(\Omega)$  is a set of square integrable functions and  $P_1$  a set of piecewise linear functions in the discretized domain  $\Omega$  [25]. The vector fields at the vertices are given as  $u$ .  $D(\Omega)$  is a set of divergence free functions. The vectors  $u$  used in the finite element therefore

- are continuous in the normal direction.
- are square integrable.
- have a curl describable by piecewise linear functions.

Figure 4.2 shows the finite element with the unknowns marked at each point. For reasons of simplicity, only the face is shown. The variables  $u_i^j$  and  $u_j^i$  are imposed across element boundaries, therefore guaranteeing tangential continuity at boundaries. Additionally, they inherently defined a linear polynomial, meaning that they describe a gradient of the field along this edge. This relation is mathematically described as

$$\mathbf{u} \cdot \mathbf{t}_{ij} = \frac{1}{l_{ij}} (u_i^j - u_j^i), \quad (4.3)$$

where  $\mathbf{t}_{ij}$  is the unit vector tangentially to the edge from node i to node j and  $l_{ij}$  is the length of this edge.

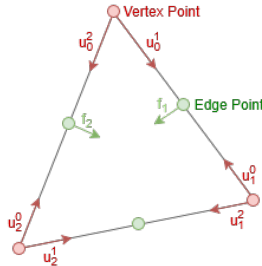


**Figure 4.2** Face of the finite element with unknowns

Two facial unknowns  $f_1$  and  $f_2$  are added to two of the three edge points at one face. Contrary to the variables  $u_i^j$ , the facial unknowns  $f_i$  are only assigned locally at each element and do not cross boundaries. The purpose of the facial unknowns  $f$  is to provide a quadratic polynomial for the field component normal to the edges. This will lead to a linear approximation for the curl of the unknown vector field  $\nabla \times \mathbf{u}$ , providing sufficient accuracy. The overall vector field of this element is then calculated by a superposition of all nodes' vector attributions.

### 4.3 Solving the differential equation

A testing function  $\mathbf{W}_n$  is defined, which is multiplied to Equation 4.1. Integrating over the whole test volume then leads to

$$\int_{\Omega} \left( \mathbf{W}_n \cdot \nabla \times \left( \frac{1}{\mu_r} \nabla \times \mathbf{E} \right) - k_0^2 \epsilon_r \mathbf{W}_n \cdot \mathbf{E} \right) dV = 0. \quad (4.4)$$

This yields  $N$  equations, with  $n = 1, 2, \dots, N$ , for each finite element in the domain  $\Omega$ . This is a common procedure in FEM, and it works through orthogonalization of the residual of Equation 4.1 with respect to the function  $\mathbf{W}_n$ . This means the new goal of the solution is to minimize the residual by making  $\mathbf{W}_n$  as orthogonal as possible [26].

Using the vector identity  $\nabla \cdot (\mathbf{a} \times \mathbf{b}) = (\nabla \times \mathbf{a}) \cdot \mathbf{b} - \mathbf{a} \cdot (\nabla \times \mathbf{b})$  on Equation 4.4 provides a weak form of the equation, meaning a form of the original partial differential equation, which does not contain all original derivatives [7, 6]. Additionally, boundary terms come into play, as seen in the right hand side of the resulting

$$\int_{\Omega} \left[ (\nabla \times \mathbf{W}_n) \cdot \frac{1}{\mu_r} \nabla \times \mathbf{E} - k_0^2 \epsilon_r \mathbf{W}_n \cdot \mathbf{E} \right] dV = \underbrace{\oint_{\partial\Omega} \left( \mathbf{W}_n \times \frac{1}{\mu_r} \nabla \times \mathbf{E} \right) \cdot d\mathbf{S}}_{\text{Boundary term}}. \quad (4.5)$$

The usefulness in this step has been described as lowering the highest-order derivative, therefore the approximating functions need to guarantee continuity of value, not of slope [14]. Another explanation is the possibility of incorporation of Neumann boundary conditions [26].

Next, the electric field  $\mathbf{E}$  is represented by a superposition of basis functions. When applying Galerkin's method, the basis functions are equal to the test functions  $W_n$ . The sum of the basis functions is

$$\mathbf{E} = \sum_m^N x_m \mathbf{W}_n, \quad (4.6)$$

which are weighted with the variable  $x_m$ . These variables  $x$  for all elements have to be solved, to find the electric field  $\mathbf{E}$  over the whole domain. The FEM has therefore reduced the initial wave equation in Equation 4.1 to a simple linear matrix equation  $Ax = b$ , where  $A$  is a known  $N \times N$  matrix,  $b$  contains port excitations and  $x$  is the unknown. Ideally, the basis functions are defined to be zero outside of their adjacent elements. This will result to zero for all entries in the matrix, where the test and basis function do not overlap. Therefore, the matrix is sparse, and will be solved much faster. In the end, other electromagnetic quantities can all be derived through the electric field.

The matrix then is expressed as

$$A_{ij} = \int_{\Omega} \nabla \times \mathbf{W}_i \cdot \frac{1}{\mu_r} \nabla \times \mathbf{W}_j dV - k_0^2 \int_{\Omega} \mathbf{W}_i \cdot \epsilon_r \mathbf{W}_j dV + ik_0 \left( \frac{\eta_0}{Z_s} \right) \oint_{\partial\Omega} \mathbf{n} \times \mathbf{W}_i \cdot \mathbf{n} \times \mathbf{W}_j d\mathbf{S}. \quad (4.7)$$

Some manipulation on the boundary term have been made, so that it contains the surface impedance  $Z_s$ . The surface impedance defines the ratio of the electric field to the magnetic field on the boundary region. Furthermore, it contains the free space, which equals  $\eta_0 \approx 377 \Omega$ .

#### 4.4 Adaptive solution process

Each finite element therefore has a solved electric field assigned, which should approximate the real solution as closely as possible. To determine the error for each element, Equation 4.1 is evaluated. The elements with the highest residuals contain the largest deviation from the real result, meaning they have a large degree of error, as described in

$$\nabla \times \left( \frac{1}{\mu_r} \nabla \times \mathbf{E}_{\text{solved}} \right) - k_0^2 \epsilon_r \mathbf{E}_{\text{solved}} = \text{residual}. \quad (4.8)$$

Regions in the mesh with large degrees of errors are refined, i.e. the tetrahedral finite elements are split into smaller ones. This allows the FEM solver to recalculate the fields in this region with higher precision, leading to a smaller residual. Consequently, the finite elements represent the fields more accurately, due to a smaller element size and higher resolution [5]. An additional method is increasing the order of the polynomial basis functions of elements with low degree of accuracy.

To determine when the iterative refinement process is done and the solution good enough, some kind of threshold must be defined. One possibility is the Max  $\Delta S$  parameter. It is compared to the difference of S-parameters of the defined excitation ports over two iterations. If, after a mesh refinement, the S-parameters of the ports do not significantly change anymore, meaning change less than Max  $\Delta S$ , then the iterative process can be considered done. This described iterative process is shown in Figure 4.3.

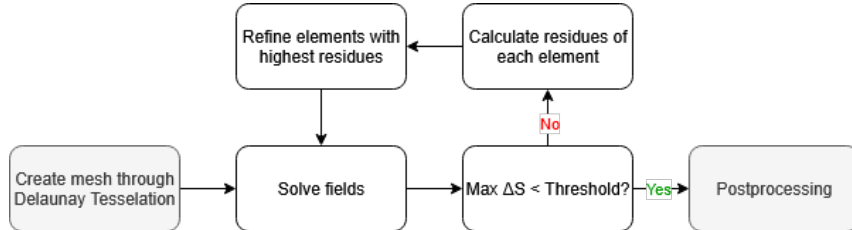


**Figure 4.3** Adaptive solution process

## 5 Numerical Investigations of Antennas in TEM Cells

### 5.1 Preliminary Considerations for Numerical Analysis

#### 5.1.1 Antenna models

Every antenna is fed with a round feedpoint, shown in Figure 5.1. They provide an incident wave of unit power (1 W). The antenna wires are modeled as PECs with a diameter of 0.2 mm. The geometry is intentionally kept simple, with the cylindrical wires pointing either in  $x$ -,  $y$ - or  $z$ -direction, without combining multiple orientations.

The investigations in this thesis focus on the coupling behavior of antennas. All conducting surfaces in the simulation models are perfect electric conductors (PEC) to remove the

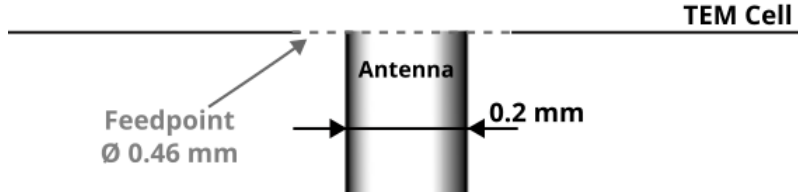


**Figure 5.1** Geometry of an antenna's feedpoint used in simulation. The antenna is fed through a round waveport of diameter 0.46 mm. The antenna consists of PEC wire with diameter of 0.2 mm. This geometry leads to a reference impedance of  $Z_0 \approx 50 \Omega$ .

influence of lossy conductors, which are especially significant due to the Skin-effect. Conductor losses contribute to the power consumption of the small loop antenna, for example, and is significantly larger than radiation power [3, p. 231].

The first two antennas investigated are the monopole (Section 5.2) and the loop antenna (Section 5.3), which represent the most basic antennas producing electric and magnetic dipole moments, respectively. Other electrically small antennas deliver similar results, depending on whether they are capacitive or inductive. Capacitive antennas are analogous to monopole antennas, and inductive ones to the loop antenna, both including their equivalent circuits. This applies even for electrically small antennas with high Q-factor.

### 5.1.2 TEM cell model

The TEM cell model used, shown in Figure 3.4, has a width of  $a = 40$  mm, a height of  $b = 24$  mm and a length of  $l = 100$  mm. The cut-off frequencies of higher-order modes are demonstrated in Figure 3.5. In following investigations focusing on the TEM mode, the frequency range of interest spans from 1 MHz to 3 GHz. If the TE<sub>01</sub> mode is included in the investigations, the upper limit of the frequency range is extended to 3.3 GHz.

The cell walls and septum are modeled as PECs. In the TEM cell simulation model, the tapered transition sections at the ports are omitted. As discussed in Section 3.4.1, this simplification allows unrestricted propagation of higher-order modes, facilitating investigations of their coupling behavior with antennas. The reference impedances of the output ports equal  $Z_w \approx 50 \Omega$ .

Upon exciting the output ports, the electric and magnetic energy  $W_e$  and  $W_m$  stored in the TEM cell is derived by Equation 2.24. The current and voltage at the output ports is found with Equations (5.5) to (5.6). The capacitance and inductance of the TEM cell are given by Equations (2.25a) to (2.25b). The TEM cell has a constant capacitance and inductance of  $C_T = 6.74$  pF and  $L_T = 16.25$  nH.

### 5.1.3 Dipole moments models

A magnetic dipole moment can be expressed equivalently as either an electric current  $I_0$  in a loop, or a magnetic current  $I_m$  in a line, as described in Equation 2.16. All dipole moments used in the simulations are assumed to be of infinitesimal length, as discussed in subsubsection 2.1.1 and subsection 2.2. For infinitesimal magnetic dipoles, Equation 2.16 simplifies to

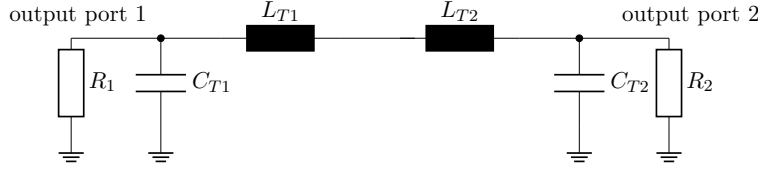


**Figure 5.2** Circuit representing the TEM cell, where the capacitance and inductance is split into two separate, equal components  $C_T = C_{T1} + C_{T2}$ ,  $L_T = L_{T1} + L_{T2}$  and  $C_{T1} = C_{T2}$ ,  $L_{T1} = L_{T2}$ . The resistances  $R_1, R_2$  at the output ports model the reference impedance  $Z_w \approx 50 \Omega$ .

$$|\mathbf{m}_m| = j\omega\mu_0|\mathbf{m}_0|, \quad (5.1)$$

where  $\mathbf{m}_m$  with the unit Vm denotes the magnetic dipole moment in the magnetic current representation, and  $\mathbf{m}_0$  with the unit Am<sup>2</sup> the moment in the electric current representation [20]. The simulation models represent magnetic dipole moments with  $\mathbf{m}_m$ , which will be used in further investigations.

The electric and magnetic dipole moments are placed at the center of the TEM cell at  $x = 0, y = b/2, z = 0$ . As discussed in subsubsection 3.4.2,  $\mathbf{e}_{\text{TEM}}^{\pm}(x = 0, y = b/2, z = 0)$  has only a y-component at this location, while  $\mathbf{h}_{\text{TEM}}^{\pm}(x = 0, y = b/2, z = 0)$  has only an x-component. Consequently, the equivalent dipole moment  $\mathbf{m}_e$  is oriented along the y-direction, and  $\mathbf{m}_m$  along the x-direction.

Placing  $\mathbf{m}_m$  and  $\mathbf{m}_e$  in the center of the TEM cell therefore significantly simplifies modeling electrically small antennas with equivalent dipole moments. This assumption is valid for the TEM mode. This configuration is assumed for all numerical investigations following in this thesis, unless otherwise stated.

When normalizing to the free-space wave impedance  $\eta_0$ ,  $\mathbf{m}_e$  can be interchanged with an equivalent  $\mathbf{m}_m$  and vice-versa [15, p. 414]. Therefore, normalizing either  $\mathbf{m}_e$  or  $\mathbf{m}_m$  to the free-space wave impedance  $Z_0$  enables a meaningful comparison between them.

All simulation results are counterchecked by inserting the equivalent dipole moments into the TEM cell and comparing the power and phase at the output ports with the antenna's results.

#### 5.1.4 Mesh modifications

The mesh determines the resolution of the field quantities over the computational domain. Since electrically small conductors are involved, implementing small mesh elements in their proximity is necessary for accurate modeling of near-fields. Adaptive meshing algorithms may neglect this task, due to the low impact of these near-fields on the solution of the overall computational domain. Consequently, adjusting mesh element sizes does not significantly influence the overall solution of the model, but greatly improves the accuracy of near-field investigations.

The maximum mesh element length in error-prone volumes are adjusted, until the obtained results show a reasonably low amount of numerical artifacts. Such volumes are commonly located adjacent to feedpoints and along edges of small conductors, where large field intensities occur within small spatial regions. The simulation models used in this thesis use roughly 15 elements on the surfaces of such critical volumes to achieve a reasonable representation of these regions while avoiding excessively large meshes.

Lastly, it is best practice to select the upper limit of the investigated frequency range as the solution frequency. This choice produces the largest spatial field changes, forcing the adaptive mesh process to generate a high-resolution mesh. Results in the frequency range below the solution frequency benefit from a reusable mesh that is finer than required. This procedure is applied for every numerically derived frequency-dependent result presented in this thesis.

### 5.1.5 Shielding material models

The numerical investigation of large computational domains containing thin shielding material requires large mesh sizes for accurate representation of fields around the shield. Especially in the analysis of the ASTM ES7-83 method in Section 6.1, the shielding material leads to high computational effort. A solution is the implementation of boundary conditions on the shielding material's surface, as described in [4].

In this solution process, the shielding material is removed from the computational domain. Instead, the boundary conditions imposed on its surface are considered, and plane wave propagation normal to the surface is assumed.

### 5.1.6 S-parameters and derived data

The TEM cell with an antenna is modeled as a three-port network. The two output ports of the TEM cell are denoted as ports 1 and 2, while the antenna feedpoint is marked as port A. The behavior of this system is fully characterized by its scattering matrix, given as

$$[S] = \begin{bmatrix} S_{11} & S_{12} & S_{1A} \\ S_{21} & S_{22} & S_{2A} \\ S_{A1} & S_{A2} & S_{AA} \end{bmatrix}. \quad (5.2)$$

The coupling between the antenna and the two ports of the TEM cell are described by S-parameters, specifically the forward transmission coefficients  $S_{A1}$  and  $S_{A2}$ . The phases of the forward transmission coefficients  $\Phi_{A1}$  and  $\Phi_{A2}$  provide information on the phase shift between the incident wave at port A, and the transmitted wave at output ports 1 and 2. The magnitude of this coefficient is the same for the antenna to both ports  $|S_{A1}| = |S_{A2}|$ , given that the antenna is placed far from the output ports. The power transferred from the antenna  $P_A$  to the output ports  $P_1$  and  $P_2$  is derived through

$$P_A = \frac{P_1}{10^{|S_{A1}|/10}} = \frac{P_2}{10^{|S_{A2}|/10}}. \quad (5.3)$$

Consequently, if the normalized electric field distribution of the TEM mode  $\mathbf{e}_{\text{TEM}}^{\pm}$  is unknown, it may be derived by setting the output power of a waveport to  $P_1 = P_2 = 1/2 \text{ W}$ . For example, the uniformly distributed, normalized electric field of the TEM mode along the y-axis at the center of the TEM cell ( $z = 0, x = 0$ ) is derived by

$$|a_{\text{TEM}}| \cdot \mathbf{e}_{\text{TEM}}^+(x = 0, y, z = 0) = \frac{\sqrt{P_1 Z_0}}{b/2}. \quad (5.4)$$

The difference in phase of  $S_{A1}$  and  $S_{A2}$  influences the magnitude of magnetic dipole moments and electric dipole moments, as discussed in subsubsection 3.5.2. The peak value of the current through the feedpoint of the antennas is calculated with the S-parameters,

$$I_A = \sqrt{2P_A} \frac{(1 - S_{AA})}{\sqrt{Z_0}}. \quad (5.5)$$

$P_A$  is the incident power wave applied to the port. The peak voltage at the feedpoint is calculated in a similar fashion as

$$V_A = \sqrt{2P_A}(1 - S_{AA})\sqrt{Z_0}. \quad (5.6)$$

Another method to derive voltages and currents is by integration of field intensities. Special care has to be taken at mesh refinement in the area of integration to reduce numerical errors.

The impedance seen from the antenna feedpoint is

$$Z_A = Z_0 \frac{1 + S_{AA}}{1 - S_{AA}}. \quad (5.7)$$

All values are peak values, unless otherwise stated.

### 5.1.7 Investigation of Field Regions

This section investigates whether the frequency-dependent non-linear behavior observed in output power measurements is intrinsic to the antenna's geometry or influenced by the dominant coupling field region discussed in Section 2.3 within the TEM cell.

To isolate these effects, a numerical analysis was conducted using two TEM cells of significantly different sizes, as shown in Figure 5.3. By scaling the cell geometry while maintaining a constant characteristic impedance, the physical distance  $r$  between the source and the septum changes, thereby shifting the  $k \cdot r$  factor across the frequency spectrum. If the normalized output power remains consistent between the two configurations, it confirms that the coupling mechanism is invariant to the specific field region and is primarily defined by the source's dipole moments.

The investigation compares a large TEM cell ( $a = 40 \text{ mm}, b = 24 \text{ mm}$ ) against a small TEM cell ( $a = 10 \text{ mm}, b = 6 \text{ mm}$ ). Both configurations are designed to maintain a

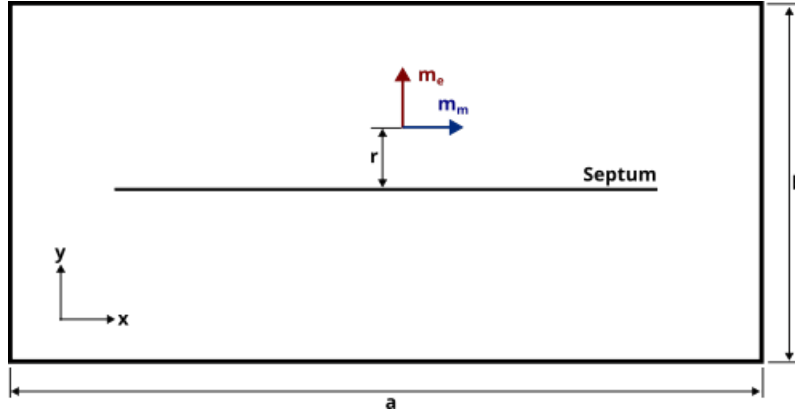


**Figure 5.3** Numerical model of a TEM cell containing an electric moment  $\mathbf{m}_e$  and a magnetic dipole moment  $\mathbf{m}_m$  positioned at the center ( $x = 0, y = r = b/4, z = 0$ ). This setup is used to investigate the specific field regions in which coupling occurs.

characteristic impedance of  $Z_0 \approx 50 \Omega$ . Identical electric and magnetic dipole moments were placed in both cells, exhibiting the behavior shown in Figure 5.4b.

The resulting output power, normalized to unity for comparison, is presented in Figure 5.4a. The close agreement between the power curves of the small and large cells indicates that the varying field regions have a negligible impact on the output power shape. Consequently, it can be concluded that the coupling occurs predominantly in the near-field region, and the influence of changes in field regions with frequency can be neglected in subsequent investigations.

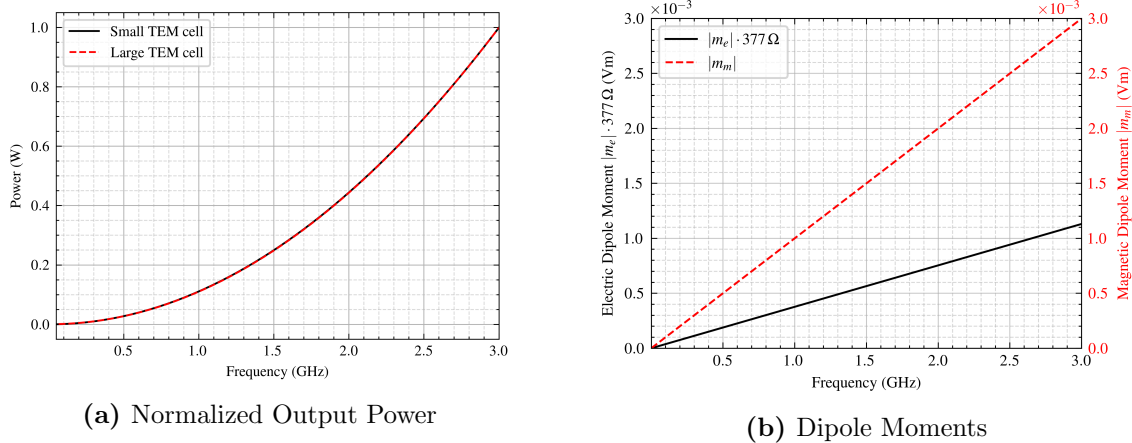


**Figure 5.4** Comparison of coupling behavior: (a) The normalized output power produced by dipole moments in the large versus the small TEM cell, and (b) the dipole moments used as the source. The congruence of the power curves demonstrates that the coupling is independent of the cell dimensions.

## 5.2 Monopole Antenna

### 5.2.1 Setup

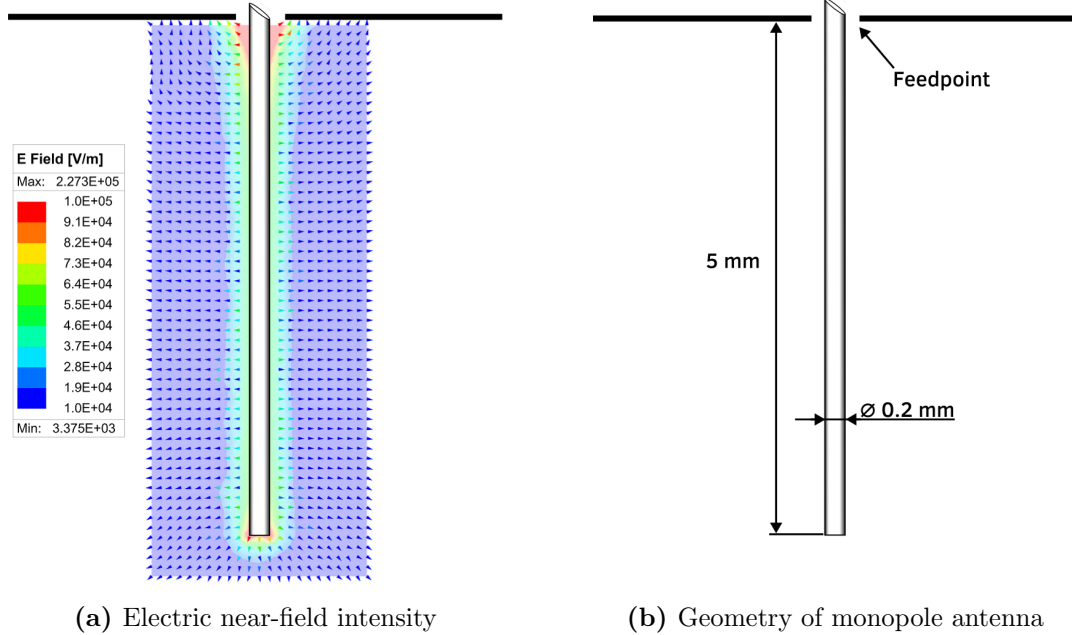


**Figure 5.5** The geometrical aspects of the cylindrical monopole antenna, as implemented in the simulation model, with the respective electric near-field plot.

The monopole antenna is the most basic antenna generating an electric dipole moment. It is shown in Figure 5.5b, installed in the TEM cell and connected to a feed point located on the top wall. The numerically derived near-field plot of the monopole antenna shows strong displacement currents near the feedpoint and at the wire end. Simulation results are improved by decreasing mesh element lengths in these regions. The current flowing through it is aligned with the TEM mode and produces an electric dipole moment.

The antenna has a physical length of 5 mm, making it electrically short for frequencies up to 6 GHz. For frequencies up to 1.25 GHz, it can be accurately approximated as an infinitesimal electric dipole, as discussed in subsubsection 2.1.1. At higher frequencies, up to 6 GHz, it behaves as a small electric dipole, as explained in subsubsection 2.1.2.

### 5.2.2 Equivalent dipole moments

The corresponding equivalent electric and magnetic dipole moments,  $\mathbf{m}_e$  and  $\mathbf{m}_m$ , are analytically derived using Equations (3.46a) to (3.46b). The resulting  $\mathbf{m}_e$  shown in Figure 5.6 increases approximately linearly over frequency, while the magnetic dipole moment is negligible over the whole frequency range.

Furthermore, the phase difference between the power at the two output ports is zero across the entire frequency range. This observation is consistent with the assumption that a pure electric dipole moment introduces no phase shift between the output port powers,

as discussed in subsubsection 3.5.2.

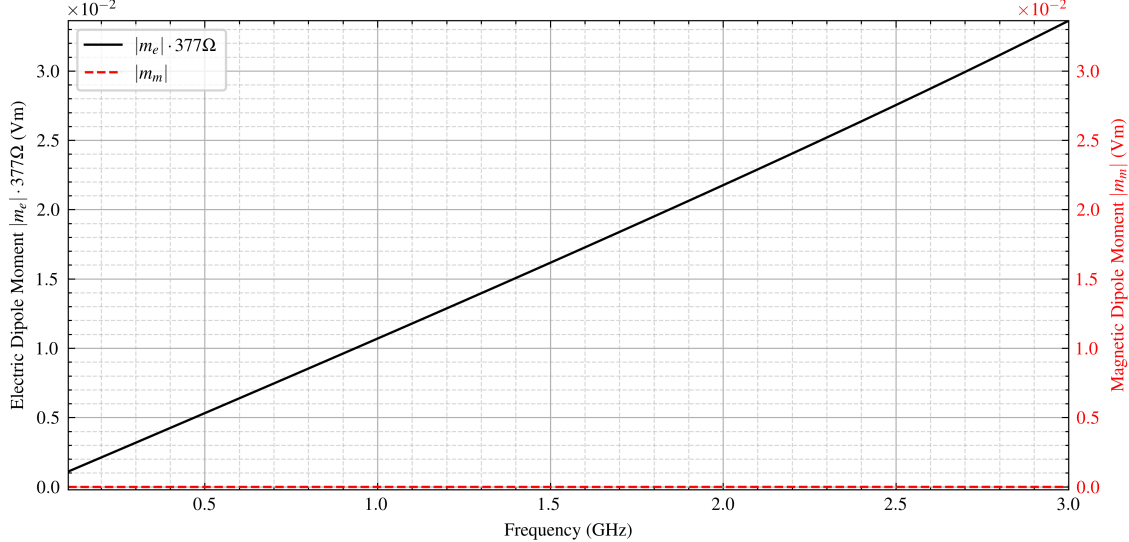


**Figure 5.6** The equivalent electric and magnetic dipole moments analytically calculated with Equations (3.46a) to (3.46b). To enable direct comparison with the magnetic dipole moment, the electric dipole moment is weighted with the free space impedance  $Z_0$ , as discussed in subsubsection 5.1.3.

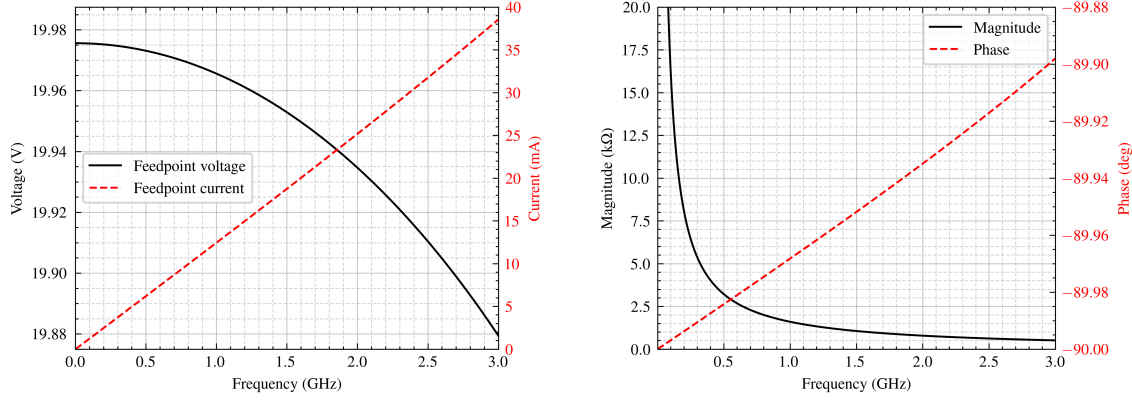
### 5.2.3 Electrical characteristics

The feedpoint voltage  $V$  of the antenna, shown in Figure 5.7a, remains largely constant over the investigated frequency range. Consequently, the voltage induced between the antenna and the septum is negligible. This observation is consistent with the absence of a magnetic dipole moment  $\mathbf{m}_m$ , which is directly related to the induced voltage according to Equation 3.50.

The feedpoint current  $I$ , shown in Figure 5.7a, increases linearly. The entire current contributes to displacement currents due to the absence of a return path. According to Equation 3.56,  $\mathbf{m}_e$  is proportional to the displacement current to the septum. The linear increase of  $\mathbf{m}_e$  and  $I$  are therefore related.

At low frequencies, the antenna impedance in Figure 5.7b shows a high magnitude, which rapidly decreases as frequency increases. Over the whole frequency range, it exhibits highly capacitive behavior, which is consistent with Equation 2.11 and the discussion in subsubsection 2.1.1.

Applying Equation 3.56 to determine  $\mathbf{m}_e$  requires knowledge of the magnitude of the displacement current to the septum. Another possibility of determining  $\mathbf{m}_e$  is the integration of the current  $I$  along the monopole antenna, as given in Equations (3.48a) to (3.48b). At a frequency of 3,GHz, this approach yields



(a) Voltage and current at feedpoint over frequency

(b) Antenna impedance over frequency

**Figure 5.7** Magnitude of the voltage and current applied at the feedpoint of the monopole antenna over frequency, derived through the S-parameters with Equations (5.5) to (5.6), with the respective magnitude and phase of the antenna impedance over frequency, derived through the S-parameters with Equation 5.7.

$$\mathbf{m}_e(f = 3 \text{ GHz}) = \int_{b/2-5 \text{ mm}}^{b/2} I(y, f = 3 \text{ GHz}) dy = 85.69 \mu\text{Am} \cdot \hat{\mathbf{a}}_z, \quad (5.8)$$

which corresponds to  $\mathbf{m}_e \cdot Z_0 = 3.23 \cdot 10^{-2} \cdot \text{Vm} \hat{\mathbf{a}}_z$  when normalized by the free-space wave impedance  $Z_0$ . This approximates  $\mathbf{m}_e$  in Figure 5.6 at 3 GHz reasonably well, therefore supporting Equations (3.48a) to (3.48b).

The derived equivalent dipole moments  $\mathbf{m}_e$ ,  $\mathbf{m}_m$  in the TEM cell produce the output power over frequency shown in Figure 5.8b, where they are compared with the output power produced by the monopole antenna. The equivalent dipole moment approximation of the monopole antenna loses precision when approaching the cut-off frequency of the first higher-order mode  $\text{TE}_{01}$ . Considering the coefficients  $a_{\text{TE}01}$  and  $b_{\text{TE}01}$  of the  $\text{TE}_{01}$ -moment increases accuracy, which is not done here.

The distribution of the current along the monopole antenna shown in Figure 5.11 is numerically derived by integrating the magnetic field intensity in a closed loop around the wire using Ampère's law,

$$\oint_1 \mathbf{H} \cdot d\mathbf{l}' = I. \quad (5.9)$$

The current distribution at 3 GHz (see Figure 5.9) approximates that of a small electric dipole, as described in subsubsection 2.1.2. It shows an approximately linear decrease towards zero.

The current distribution at 1 MHz, shown in Figure 5.10, also decreases linearly along the monopole antenna. It can be approximated with an infinitesimal electric dipole, as

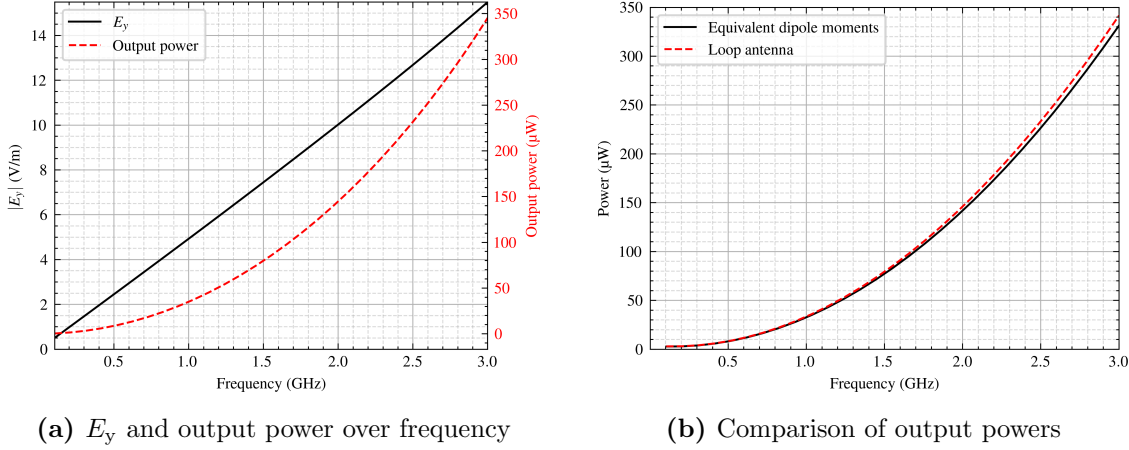


**Figure 5.8** Electric field in y-direction  $E_y$  at  $x = 0, y = b/4, z = \pm l/2$ , and power at one output port, derived with the S-parameters in Equation 5.3. The output power produced by the monopole antenna is compared to the output power produced by the equivalent dipole moments, to demonstrate validity of the model.

discussed in subsubsection 2.1.1.

A fine mesh resolution, as discussed in subsubsection 5.1.4, is important for accurate results delivered by Equation 5.9. Consequences of a rough mesh is non-linear behavior near the feedpoint at 0 mm in Figure 5.11, which becomes apparent due to significant displacement currents and numerical artifacts in this region. This causes the current to exhibit a steeper decline with non-physical oscillations.

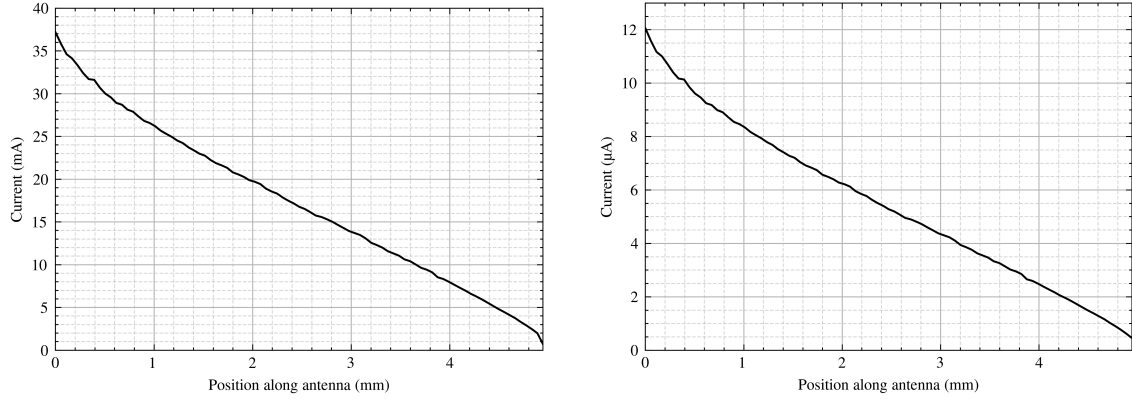


**Figure 5.9** Current distribution at 3 GHz

**Figure 5.10** Current distribution at 1 MHz

**Figure 5.11** The current distribution along the monopole antenna at 3 GHz and 1 MHz.

### 5.2.4 Equivalent circuit model

Equivalent circuit models of the antenna and the TEM cell are valuable tools for further analysis, as they enable analytical calculations and facilitate investigation and understanding of the observed coupling behavior. For the monopole antenna, the Chu equivalent circuit for a short electric dipole [13] is applied, as demonstrated in Figure 5.12, where  $R_A$ ,  $L_A$  and  $C_A$  represent the impedance behavior of the antenna.

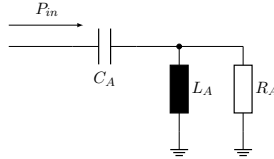


**Figure 5.12** The Chu equivalent circuit for a short electric dipole models the monopole antenna's behavior.

Although the resistance  $R_A$  generally represents conduction and radiation losses, it is omitted in this analysis. Conduction losses are non-existent due to the use of Perfect Electric Conductors (PEC). Additionally, the radiation resistance is disregarded because the radiation of the monopole on the free-space PEC plane in absence of the near-field coupling TEM cell is negligible. The antenna is therefore modeled as a lossless reactive network.

To determine  $L_A$  and  $C_A$ , the antenna model is placed on a PEC surface in an open space, as demonstrated in Figure 5.13. The inductance and capacitance are derived according to Equations (2.25a) to (2.25b), which leads to

$$L_A = 2 \frac{W_m}{I_{in}^2}, \quad (5.10a)$$

$$C_A = 2 \frac{W_c}{V_{CA}^2} = \frac{I_{in}^2}{2\omega^2 W_c}, \quad (5.10b)$$

where  $V_{CA} = I_{in}/(j\omega C_A)$  denotes the current through the capacitor  $C_A$ . The resulting capacitance equals  $C_A = 98.36 \text{ fF}$  the inductance amounts to  $L_A = 1.14 \text{ nH}$ .

The antenna equivalent circuit is extended in Figure 5.14 to incorporate the TEM cell's electrical characteristics. This cell is represented by a total inductance  $L_T = L_{T1} + L_{T2}$  and capacitance  $C_T = C_{T1} + C_{T2}$ , as derived in Section 5.1.2. To maintain structural symmetry, the model utilizes split components where  $L_{T1} = L_{T2}$  and  $C_{T1} = C_{T2}$ . It is important that this model is applied within the valid frequency range of the TEM cell equivalent circuit.

The equivalent circuits of the antenna and the TEM cell are coupled via  $C_k$ , which models the displacement current coupling, and the mutual inductances  $M_{A,T1}$  and  $M_{A,T2}$ , which account for coupling through induced voltages. The mutual inductances are given by

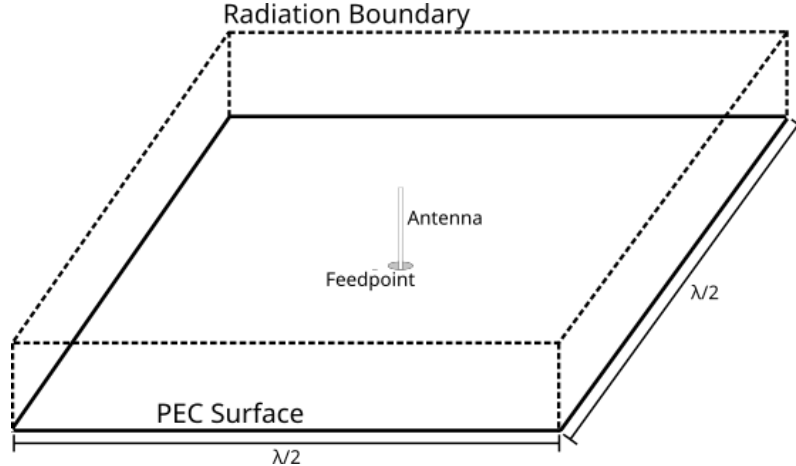


**Figure 5.13** Model of the monopole antenna connected to a feedpoint mounted on a PEC surface with a side length of  $\lambda/2$ , where  $\lambda$  corresponds to the free-space wavelength of the solution frequency. This configuration enables the investigation of the monopole antenna reactance without influence of the TEM cell.

$$\mathbf{V} = j\omega \begin{bmatrix} L_A & M_{A,T1} & M_{A,T2} \\ M_{T1,A} & L_{T1} & 0 \\ M_{T2,A} & 0 & L_{T2} \end{bmatrix} \mathbf{I}. \quad (5.11)$$

The near-field coupling between the antenna and the TEM cell is represented by the reactances  $C_k$ ,  $M_{A,T1}$ , and  $M_{A,T2}$ , which renders the inclusion of a radiation resistance  $R_A$  again unnecessary. The magnetic dipole moment  $\mathbf{m}_m$  is derived from the induced voltages across  $L_{T1}$  and  $L_{T2}$  in accordance with Equation 3.50. Similarly, the electric dipole moment  $\mathbf{m}_e$  is determined from the displacement current flowing through  $C_k$ , as defined in Equation 3.56.

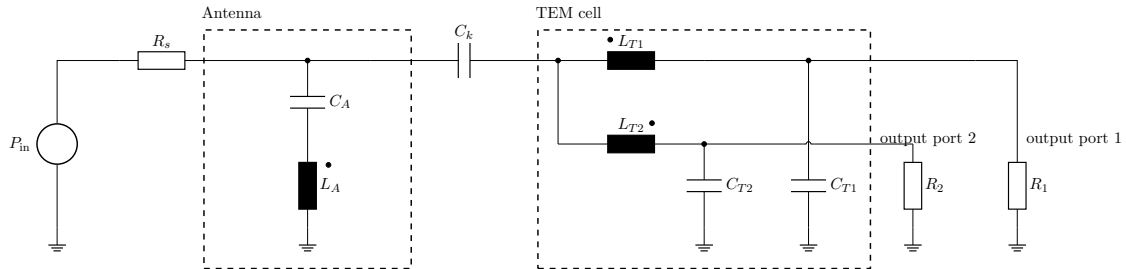


**Figure 5.14** Circuit representing the TEM cell and the monopole antenna, with the additional components  $C_k$  and  $M_{A,T1}$ ,  $M_{A,T2}$  modeling their near-field coupling behavior.

The resulting  $\mathbf{m}_e$  and  $\mathbf{m}_m$  of the monopole antenna are depicted in Figure 5.15, which qualitatively agree with the dipole moments derived by the simulator over the investigated frequency range.

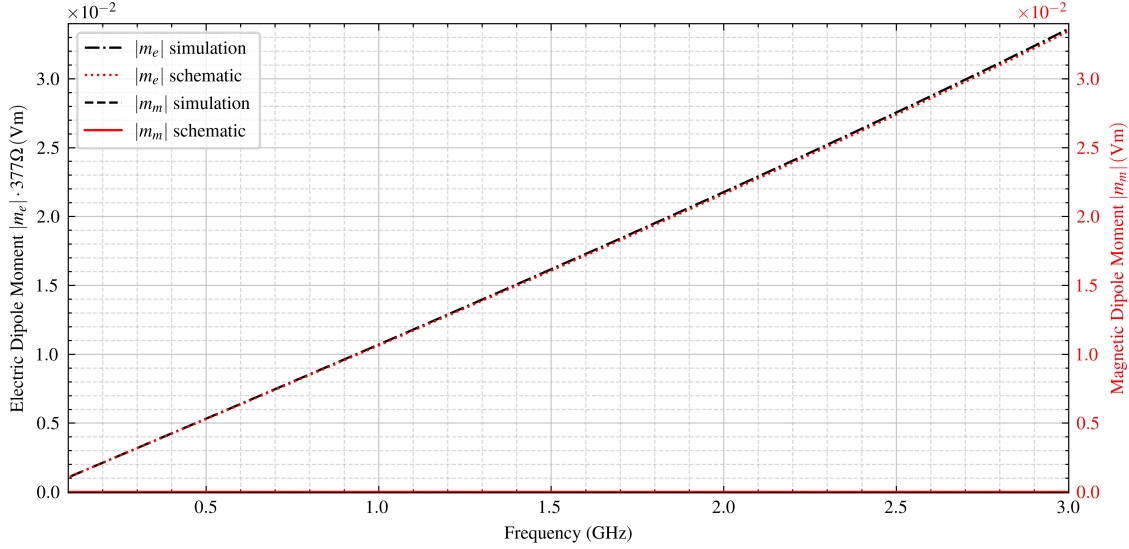
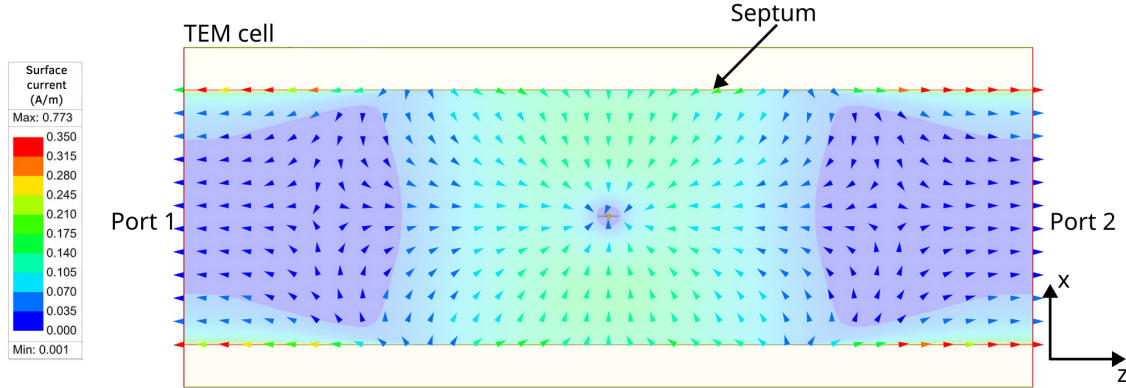


**Figure 5.15** Equivalent dipole moments derived by the equivalent circuit depicted in Figure 5.2, compared to the derived dipole moments of the monopole antenna, shown in Figure 5.6. The electric dipole moment  $\mathbf{m}_e$  is weighted with  $\eta_0$  for comparison purposes.

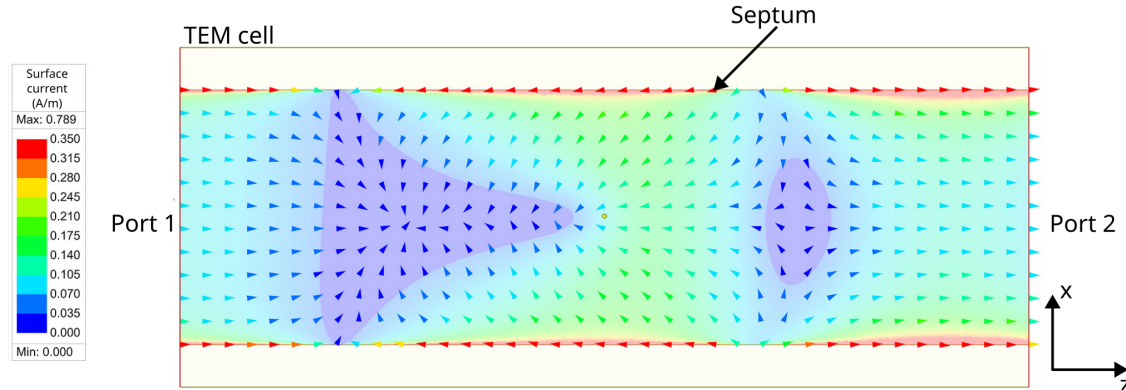
### 5.2.5 Current distribution on septum

Figure 5.16a shows the surface current density on the septum induced by the monopole antenna at 3 GHz. The current reaches both output ports in phase, confirming the absence of a phase shift between the output port powers.

Figure 5.16b shows the current density of the septum at 3.3 GHz, with the TEM-mode compensated at the output ports. Due to the magnetic fields propagating in the  $z$ -direction, the current on the septum forms a pattern of swirls. However, at a frequency of 3.3 GHz, this pattern is not as pronounced, as the current in the swirls negligible, as shown in Figure 5.16a. Furthermore, the phase shift of the induced power between the output ports is  $\pi$ . This results from the magnetic field intensities of the  $TE_{01}$ -mode being in-phase at the output ports, opposed to the magnetic field intensities of the TEM-mode.



(a) Current surface density at 3 GHz, where mostly the TEM-mode propagates.

(b) Current surface density of only the TE<sub>01</sub>-mode at 3.3 GHz with the TEM mode compensated.**Figure 5.16** Current surface densities at different frequencies, below and above the cut-off frequency of the TE<sub>01</sub>-mode.

### 5.2.6 Electromagnetic energy in the TEM cell

The monopole antenna generates electromagnetic fields within the TEM cell, resulting in stored electromagnetic energy. The frequency-dependent electric energy is shown in Equation 2.24. Its quadratic increase correlates with the output power in Figure 5.8a. The corresponding magnetic energy is several orders of magnitude smaller due to the capacitive behavior of the monopole antenna and is therefore neglected. From the stored electric energy, both the real and imaginary components of the power consumed by the antenna can be determined.

Moreover, the effective inductance and capacitance of the monopole antenna inside the TEM cell can be derived from the magnetic and electric energy expressions given in Equations (2.25a) to (2.25b). Using the peak value of the electric energy shown in Figure 5.17, the capacitance is estimated to be  $C \approx 108.55 \text{ fF}$ .

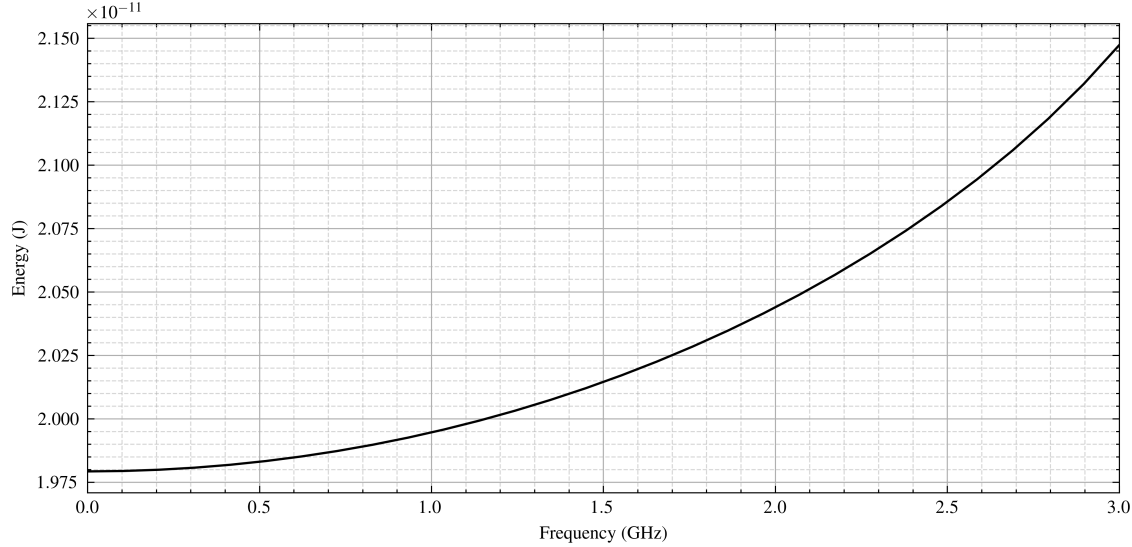


**Figure 5.17** Electric energy determined by integrating the electric field over the TEM cell volume, using Equation 2.24.

### 5.3 Loop antenna

#### 5.3.1 Setup

A loop antenna is the most basic form of an antenna generating a mangetic dipole moment.

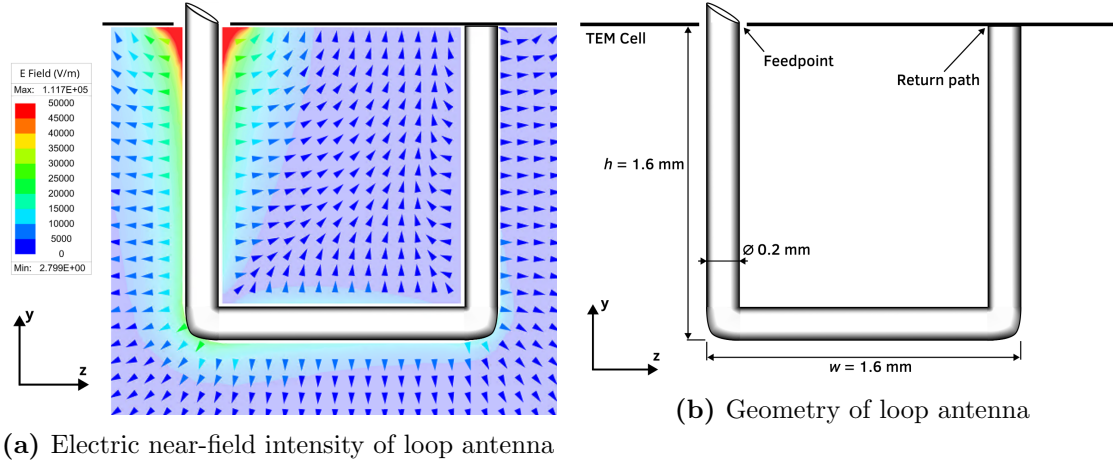
A square loop antenna is placed in the center of the TEM cell. It consists of four wires with a length of 1.6 mm each, and it is electrically short for frequencies up to 4.69 GHz. The square geometry is preferable to a round version in the numerical simulations, as it allows for more accurate meshes and enables a clearer investigation of the resulting dipole moments.

The normal vector of the loop surface points in x-direction, leading to a maximum coupling with the magnetic field of the TEM-mode. In contrast to the monopole antenna discussed in Section 5.2, a return path for the current exists, which generates a magnetic dipole moment.

#### 5.3.2 Equivalent dipole moments

The equivalent dipole moments of the loop antenna are plotted in Figure 5.19a. The magnetic dipole moment  $\mathbf{m}_m$  dominates over the electric dipole moment  $\mathbf{m}_e$ . Opposed to the case of a monopole antenna,  $\mathbf{m}_e$  and  $\mathbf{m}_m$  demonstrate non-linear behavior over frequency, which is investigated further in Section 5.3.3.

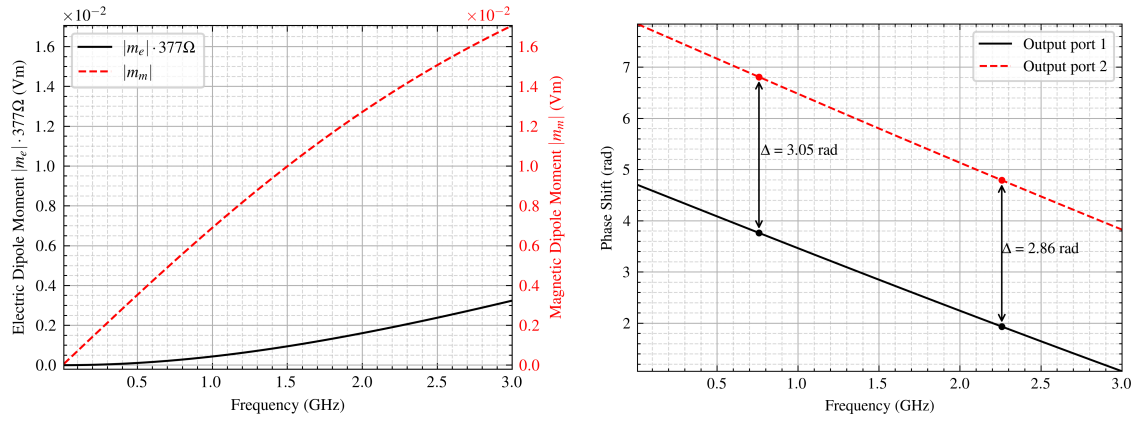
Furthermore, the phases of the powers at the output ports, shown in Figure 5.19b, differ from one another. The phase shift in the low-frequency range approaches  $\pi$ , but gradually decreases with increasing frequency. This agrees with the analysis presented in Section 3.5.2, which predicts a phase shift of  $\pi$  when only  $\mathbf{m}_m$  is present, and a reduced phase shift as  $\mathbf{m}_e$  increases, as is the case here.



(a) Electric near-field intensity of loop antenna

(b) Geometry of loop antenna

**Figure 5.18** The geometry of the loop antenna assimilates a square with round edges. The height and width of the antenna equal  $h = w = 1.6$  mm. The return path leads back to the PEC surface of the TEM cell. The electric near-field shows large a displacement current and voltage drop near the feed-point. It has been derived with a refined mesh on the antenna surface and near the feedpoint, according to the discussion in Section 5.1.4.



(a) Equivalent dipole moments

(b) Phase of the power at each output port

**Figure 5.19** The equivalent dipole moments of the loop antenna are derived analytically with Equations (3.46a) to (3.46b), where the electric dipole moment  $\mathbf{m}_e$  is weighted with  $Z_0$  to enable comparison with  $\mathbf{m}_m$ . The phases of the powers at output ports 1 and 2 are derived from the S-parameters, as discussed in Section 5.1.6. The analysis specifically focuses on the phase shift between the two ports, which provides information about the presence of  $\mathbf{m}_m$  and  $\mathbf{m}_e$ , as investigated in Section 3.5.2.

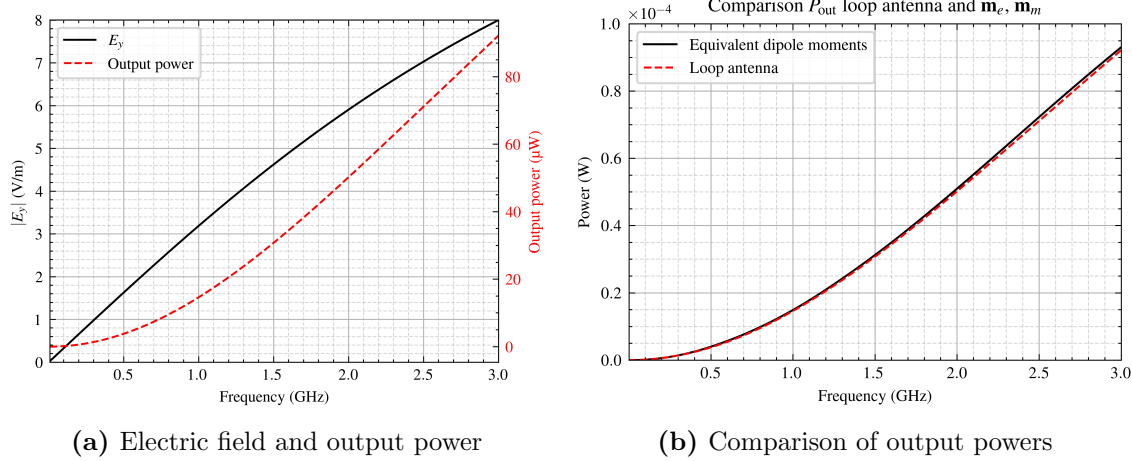


**Figure 5.20** Electric field in y-direction  $E_y$  at  $x = 0, y = b/4, z = \pm l/2$ , and the closely related power at one of the output ports, derived with the S-parameters in Equation 5.3. The output power produced by the loop antenna is compared with that generated by the equivalent dipole moments.

The power and  $E_y$  induced by the loop antenna at the output ports is shown in Figure 5.20a, and increases not as steeply as the output power of the monopole antenna exhibited in Figure 5.8a. This directly correlates with the decrease of  $\mathbf{m}_m$  with increasing frequency.

Figure 5.20b demonstrates the output power generated by the equivalent dipole moments  $\mathbf{m}_m$ ,  $\mathbf{m}_e$  and the loop antenna. Their similarity support the validity of the model used.

### 5.3.3 Electrical characteristics

Calculating the electric and magnetic energy in the radiation boundary, as discussed in Section 2.3.2.

The current  $I$  in the loop antenna changes along the antenna wire as shown in Figure 5.22a, indicating displacement current coupling to the septum and back to the feedpoint. The difference between the feedpoint and return path current increases over frequency, translating to rising displacement currents. Furthermore, the decrease in feed current over rising frequency, shown in Figure 5.22a, also hints to the presence of increasing displacement currents. Consequently,  $\mathbf{m}_e$  gains a significant magnitude according to Equation 3.56, increasing the electric coupling of the antenna to the TEM cell.

The feedpoint current is derived with Equation (5.9), through integration of  $\mathbf{H}$  in a closed loop of radius 0.11 mm, measured 0.17 mm above the feedpoint. The return path current is processed with the same loop integration at the same height above the PEC surface. The results vary with height above the PEC surface due to the displacement currents in the near-field.

Figure 5.22a demonstrates the voltage at the feedpoint of the antenna, which significantly rises over the frequency, signaling increased induced voltage  $V_n$ . According to Equa-

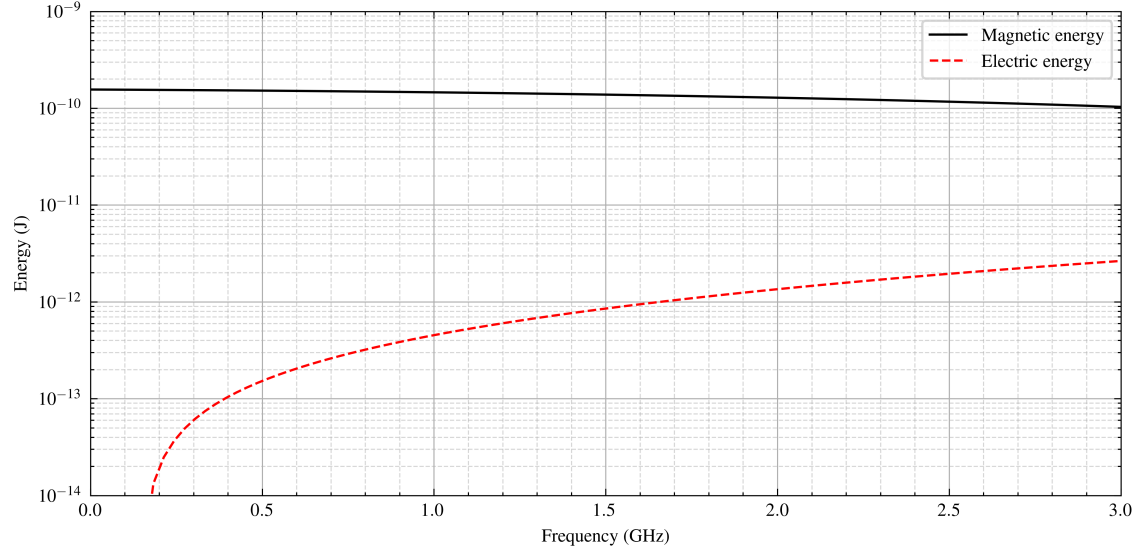


**Figure 5.21** Electric and magnetic energy produced by the loop antenna in the TEM cell, derived with Equation 2.24 in the TEM cell volume.

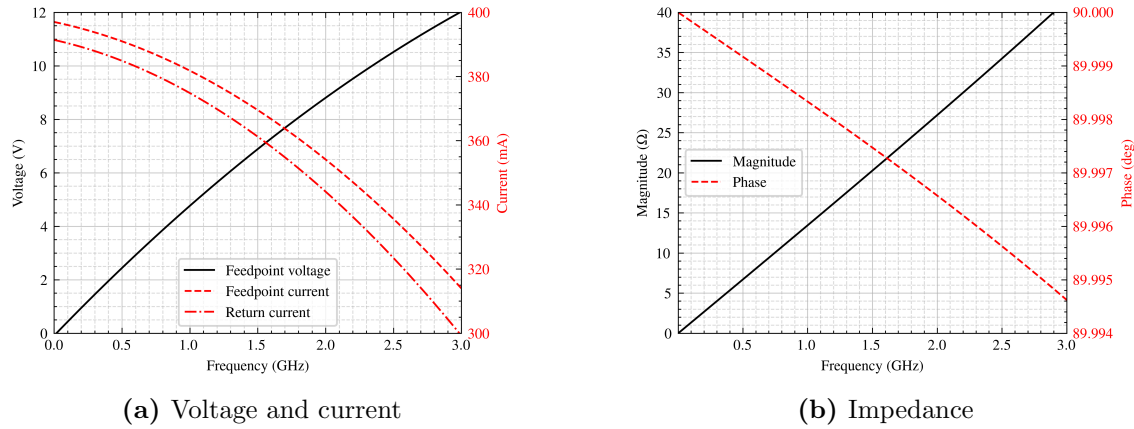


**Figure 5.22** This figure demonstrates the voltage, current and impedance characteristics of the loop antenna. The difference between the current near the feedpoint and that on the return path increases with frequency, indicating a growing occurrence of displacement currents. The current on those paths are determined through magnetic near-field intensity, using Equation 5.9. The voltage across the feedpoint is obtained using Equation 5.6. Magnitude and phase of the impedance of the loop antenna are determined with Equation 5.7.

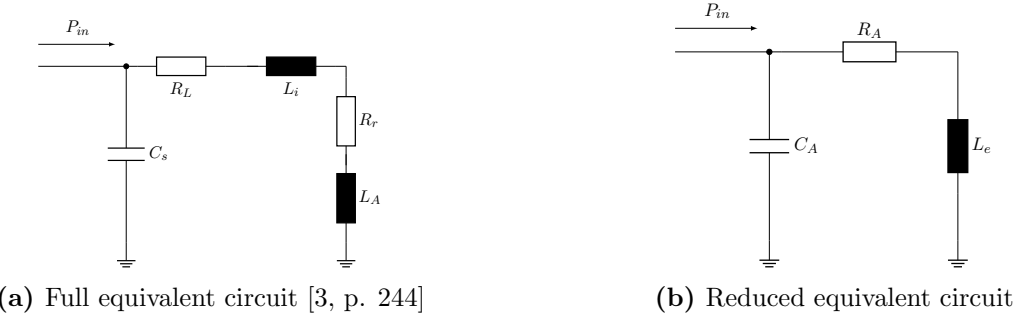


**Figure 5.23** Equivalent circuits of the small loop antenna.

tion 3.50, this directly correlates with  $\mathbf{m}_m$ , which furthermore becomes apparent when comparing their behavior shown in Figures 5.19a to 5.22a. The increase in voltage also correlates with the displacement current. It raises the potential on the loop antenna, therefore increasing the charge distributions and displacement currents.

The increases in voltage and decrease in current agrees with the impedance, depicted in Figure 5.22b. The loop antenna shows strongly inductive behavior.

### 5.3.4 Equivalent circuit model

Following the same approach established in Section 5.2.4, an equivalent circuit is derived for the small loop antenna. Figure 5.23a demonstrates the full equivalent circuit for the electrically small loop antenna in free space [3, p. 244], where

- $C_s$  Stray capacitance of the loop antenna
- $R_L$  Ohmic loss resistance of the antenna conductor
- $R_r$  Radiation resistance of the loop antenna
- $L_i$  Internal inductance of the loop antenna
- $L_e$  External inductance of the loop antenna

As discussed in Section 5.1.1, the antenna is modeled as a perfect electric conductor, therefore  $R_L$  and  $L_e$  are neglected. Instead, the simplified equivalent circuit in Figure 5.23b is applied, where  $R_A$ ,  $L_A$  and  $C_A$  represent the impedance behavior of the antenna.

To determine  $R_A$ ,  $L_A$  and  $C_A$ , the antenna model is placed on a PEC surface in an open space, as demonstrated in Figure 5.24. The inductance and capacitance are derived according to Equations (2.25a) to (2.25b), which leads to

$$L_A = 2 \frac{W_m}{I_{LA}^2} = \frac{V_{in}^2}{2\omega^2 W_m}, \quad (5.12a)$$

$$C_A = 2 \frac{W_c}{V_{in}^2}, \quad (5.12b)$$

where  $I_{LA} = V_{in}/(j\omega L_A)$  denotes the current through the inductor  $L_A$ . The resulting capacitance and inductance equal  $C_A = 38.2 \text{ fF}$  and  $L_A = 2.14 \text{ nH}$ .

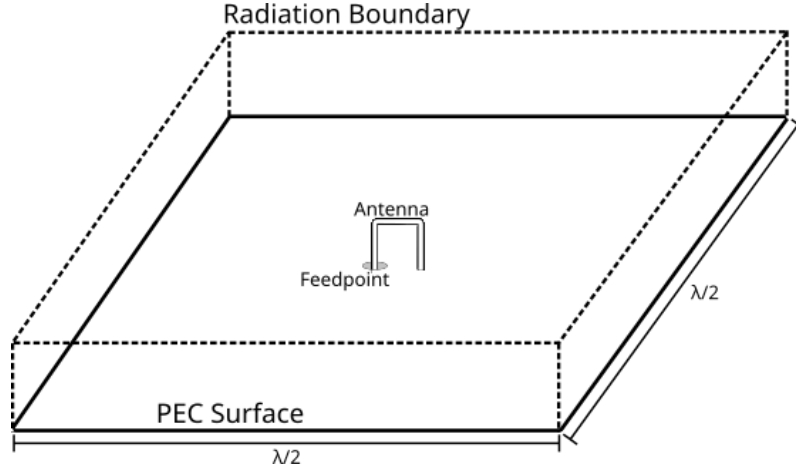


**Figure 5.24** Model of the loop antenna connected to a feedpoint mounted on a PEC surface with a side length of  $\lambda/2$ , where  $\lambda$  corresponds to the free-space wavelength of the solution frequency. This configuration enables the investigation of the loop antenna reactance without influence of the TEM cell.

The resulting  $L_A$  is compared with

$$L_{\text{sq}} = \frac{2\mu_0 l}{\pi} \left[ \ln\left(\frac{l}{w_r}\right) - 0.774 \right], \quad (5.13)$$

which provides an approximation for the inductance of a square loop antenna in free space [3, p. 245]. In this expression,  $l$  denotes the length of one side of the loop antenna and  $w_r$  the wire radius. For the loop antenna under investigation, Equation 5.13 yields  $L_{\text{sq}} = 2.32 \text{ nH}$ , which is comparable to the previously obtained  $L_A$ .

Check: Does this formula consider external inductances?

The antenna equivalent circuit is extended with the TEM cell coupling model introduced in Section 5.1.2, as shown in Figure 5.25. The coupling components  $C_k$ ,  $M_{A,T1}$  and  $M_{A,T2}$  are defined analogously to Section 5.2.4.

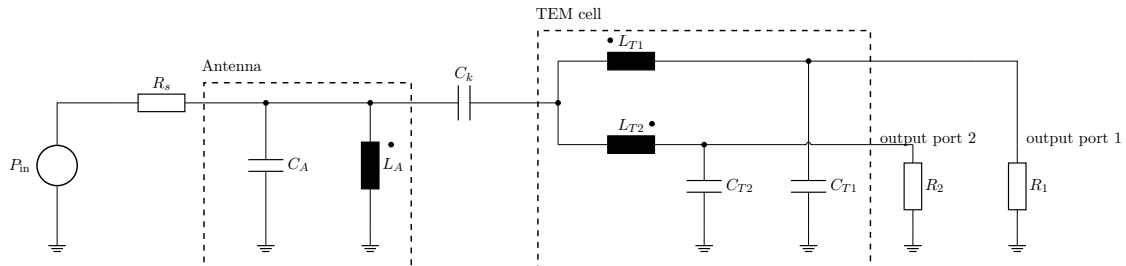


**Figure 5.25** Circuit representing the TEM cell and the loop antenna, with the additional components  $C_k$  and  $M_{A,T1}$ ,  $M_{A,T2}$  modeling their near-field coupling behavior.

The resulting  $\mathbf{m}_e$  and  $\mathbf{m}_m$  are depicted in Figure 5.26, which are similar to the dipole moments derived by the simulator in the higher end of the frequency range. However, accuracy recedes in the low-frequency range.

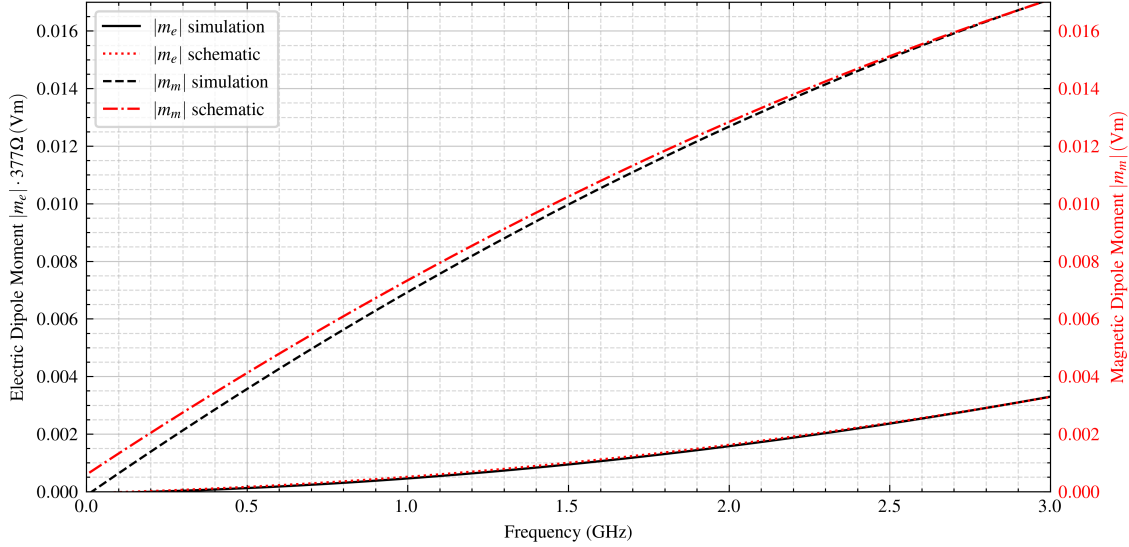


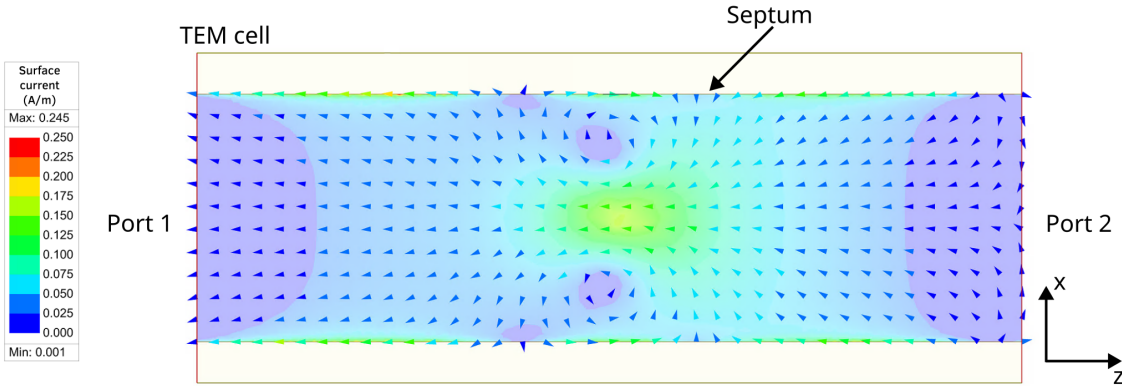
**Figure 5.26** Equivalent dipole moments derived by the equivalent circuit depicted in Figure 5.25, compared to the dipole moments of the loop antenna, shown in Figure 5.19a. The electric dipole moment  $\mathbf{m}_e$  is weighted with  $\eta_0$  for comparison purposes.

### 5.3.5 Current distribution on septum and higher order modes

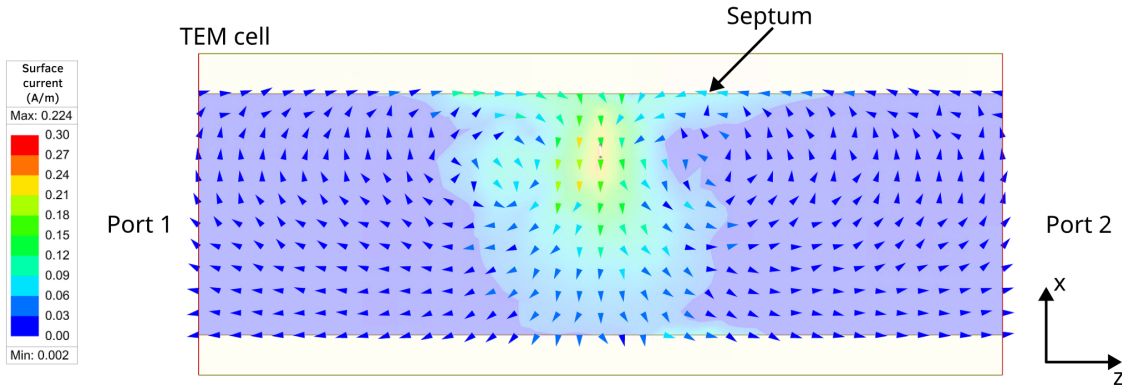
The radiating loop antenna induces surface currents on the septum of the TEM cell, as shown in Figure 5.27. At a frequency of 3 GHz, the currents reaching the output ports are out of phase, as illustrated in Figure 5.27a. This observation is consistent with the analysis in Section 3.5.2, which predicts a phase shift of  $\pm\pi$  between the output port powers in the presence of a magnetic dipole moment.

When the antenna is rotated by  $\pm\pi/4$  and offset by  $x = 7$  mm, power transmission at 3 GHz is insignificant. According to Equations (3.49a) to (3.49b) and Equation 3.50, efficient coupling requires the magnetic field intensity of the propagating TEM mode  $\mathbf{h}_{\text{TEM}}^\pm$  to be aligned with the vector normal to the antenna surface. The current distribution Figure 5.27b demonstrates no excited waves in this configuration. Instead, the power produced by the surface current remains reactive, forming closed circulation patterns around the induced magnetic fields.

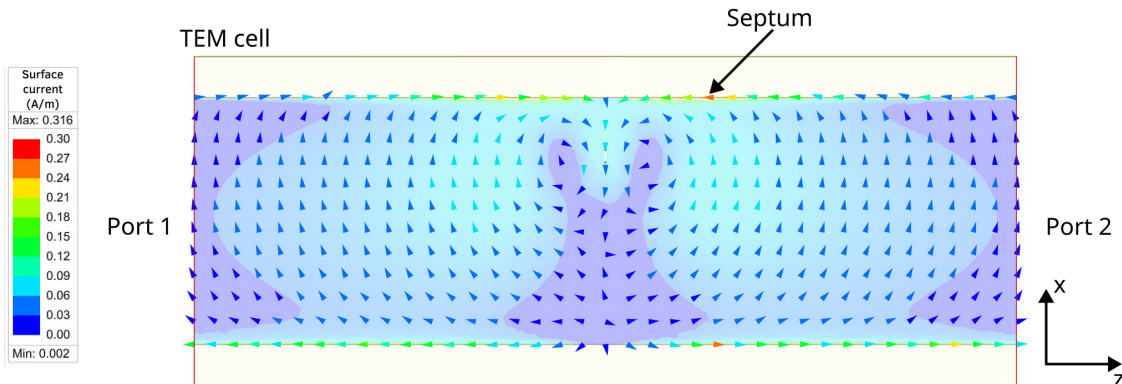
At a frequency of 3.3 GHz, the TE<sub>01</sub> mode propagates in the TEM cell. In this case,  $\mathbf{h}_{\text{TE}01}^\pm$  aligns with the normal vector of the offset and rotated loop antenna surface. As shown in Figure 5.27c, a significant proportion of the current now reaches the output ports, resulting in transmission of power. In contrast to the previous case, the output powers are in-phase, as discussed in Section 3.5.2. The output power transmitted by the TE<sub>01</sub> mode increases sharply with frequency, as demonstrated in Figure 5.28.



(a) The centrally located loop antenna without offset or rotation at a frequency of 3 GHz, where mainly the TEM mode propagates.



(b) Loop antenna with offset of  $x = 7$  mm and a  $\pi/4$  rotation angle at 100 MHz, where only the TEM mode propagates. The currents passing to the output ports are negligible.



(c) Loop antenna with offset of  $x = 7$  mm and a  $\pi/4$  rotation angle at 3.3 GHz, where the TEM and TE<sub>01</sub> modes both propagate. The currents passing to the output ports produce significant power, as shown in Figure 5.28.

**Figure 5.27** Surface current density on the septum induced by the loop antenna for different frequencies and positions of the antenna.

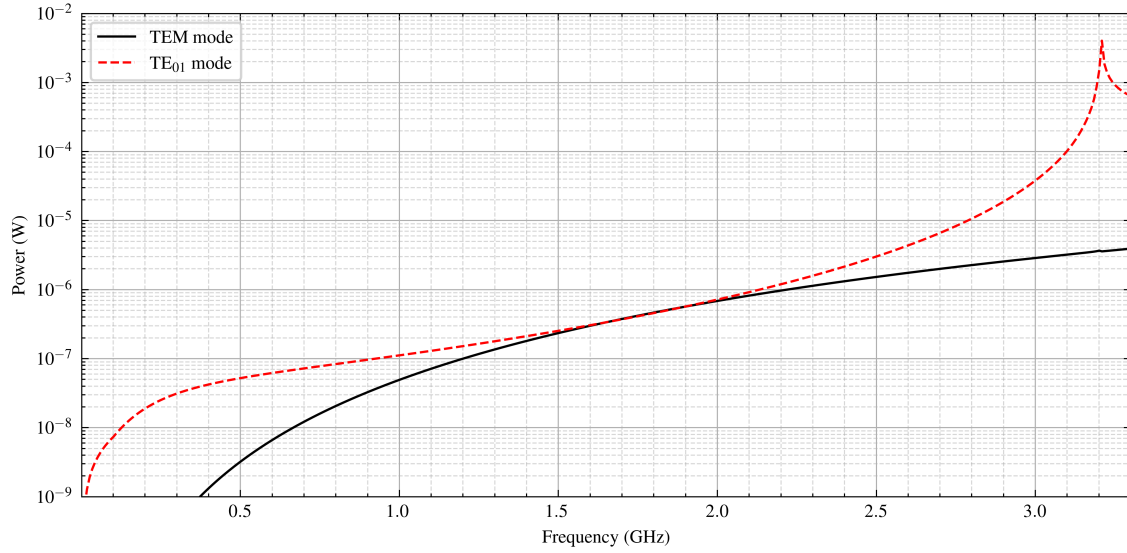


**Figure 5.28** Output power transmitted by the antenna to the output port through the TEM and TE<sub>01</sub> modes, separately over frequency, determined through the S-parameters with Equation 5.3. At a frequency of  $f = 3.21$  GHz a resonance in the TEM cell occurs, leading to the visible peak in the output power produced by the TE<sub>01</sub> mode.

### 5.3.6 Influence of antenna's geometry

The influence of the antenna's geometry on coupling behavior is investigated. The height  $h$  and width  $w$  of the loop antenna presented in Figure 5.18b is varied, and their dipole moments and power consumption compared in Figures 5.29a to 5.29b.

The loop area is identical in both configurations presented. Consequently, the behavior of the magnetic dipole moments  $\mathbf{m}_m$  are the same in both cases, which agrees with Equations (3.49a) to (3.49b). Nonlinear frequency dependence of  $\mathbf{m}_m$  persists in both configurations, due to the nearly constant capacitance of the antenna.

The electric dipole moment  $\mathbf{m}_e$  is strongly dependent on the antenna height  $h$ . The antenna with a height of  $h = 2.16$  mm generates an electric dipole moment  $\mathbf{m}_e$ , more than twice as large as that of the antenna with  $h = 1.2$  mm, as depicted in Figure 5.29a. This result supports validity of the used models and is consistent with Equation 3.56, which relates the displacement current between the antenna and septum to the electric dipole moment  $\mathbf{m}_e$ . Lastly, the output power produced by the antenna generating the larger electric dipole moment  $\mathbf{m}_e$  is also greater, as shown in Figure 5.29b.

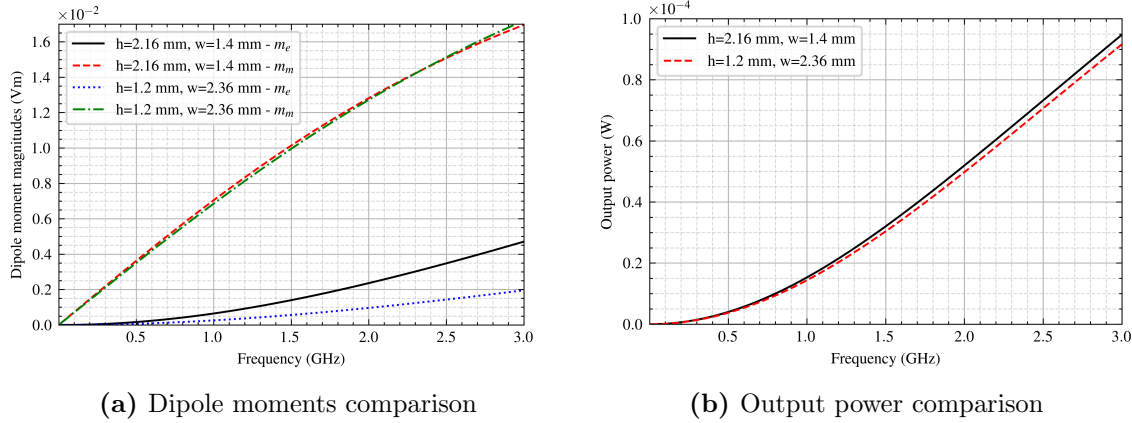


**Figure 5.29** Dipole moments and output power comparisons of two different loop antenna configurations presented, one with  $h = 2.16 \text{ mm}$ ,  $w = 1.4 \text{ mm}$  and the other with  $h = 1.2 \text{ mm}$ ,  $w = 2.36 \text{ mm}$ . The electric dipole moment  $\mathbf{m}_e$  is weighted with  $Z_0$  for comparison purposes.

## 5.4 Loop antenna with gap

### 5.4.1 Setup and geometrical analysis

The geometry of the loop antenna with a gap is similar to that of the loop antenna discussed in subsection 5.3. It is electrically short for frequencies up to 4.69 GHz. A gap with a height of 10  $\mu\text{m}$  is introduced in the return path, as shown in Figure 5.30b. The gap is intentionally kept small to emphasize specific coupling mechanics and to demonstrate the consistency of antenna analysis with the framework developed in this thesis, although such a small gap would be hard to implement in a physical antenna. Furthermore, manual mesh refinement is necessary around the gap region, as well as the feedpoint and the curved surfaces, as discussed in subsubsection 5.1.4.

The magnetic coupling is determined with Equations (3.49a) to (3.49b), just as is the case for the normal loop antenna. However, considering the gap region leads to

$$-\oint_C \boldsymbol{\tau} I(l) \cdot \mathbf{e}_n^\pm dl = - \int_{\text{wire}} \boldsymbol{\tau} I_{\text{wire}}(l) \cdot \mathbf{e}_n^\pm dl - \int_{\text{gap}} \boldsymbol{\tau} I_{\text{gap}}(l) \cdot \mathbf{e}_n^\pm dl. \quad (5.14)$$

The electric current across the gap is  $I_{\text{gap}} = 0 \text{ A}$ , while the current in the antenna wire  $I_{\text{wire}}$  is significantly reduced due to the interrupted current path. Consequently, the magnetic coupling between the loop antenna with a gap and the TEM cell is expected to be weaker than that of the loop antenna without a gap, but still more present than the monopole antenna discussed in subsection 5.2. Furthermore, reducing the gap height increases magnetic coupling and the magnitude of the magnetic dipole moment  $\mathbf{m}_m$ , attributable to the correlated increase of  $I_{\text{wire}}$ .

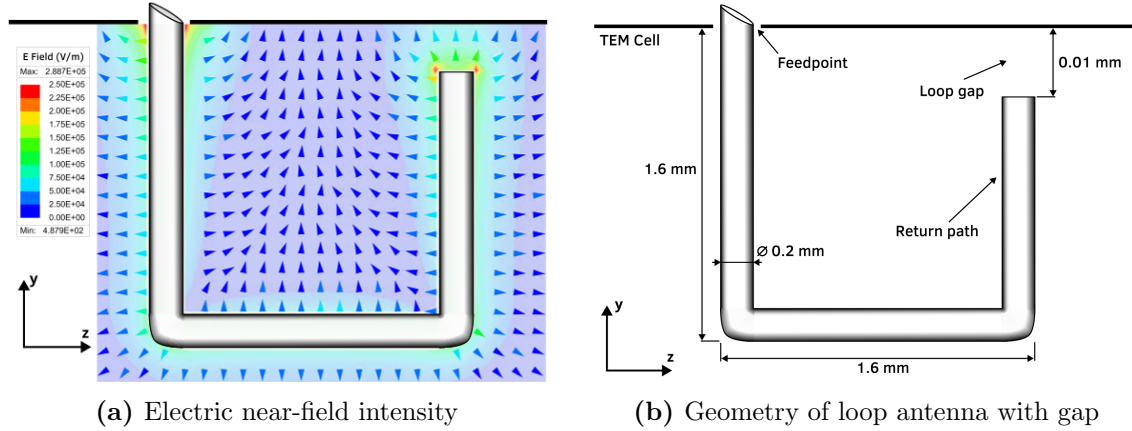


**Figure 5.30** Geometry of the loop antenna with a gap in the return path inserted in the TEM cell. The gap height is exaggerated for demonstration purposes.

The conductors adjacent to the gap behave as capacitors plates, accumulating charges on both either side. According to Equations (3.55a) to (3.55b), these accumulated charges lead to electric coupling with the septum. A smaller gap height increases the amount of accumulated charges, and consequently leads to an increase in the electric dipole moment  $\mathbf{m}_e$ . Lastly, the absence of a conductive return path for the current leads to expect capacitive behavior of this electrically small antenna, similar to the monopole antenna analyzed in subsection 5.2.

#### 5.4.2 Equivalent dipole moments

The equivalent dipole moments of the loop antenna with gap are shown in Figure 5.31a, where the electric dipole moment  $\mathbf{m}_e$  is larger than the magnetic dipole moment  $\mathbf{m}_m$ . The dipole moments behave non-linearly over the frequency.

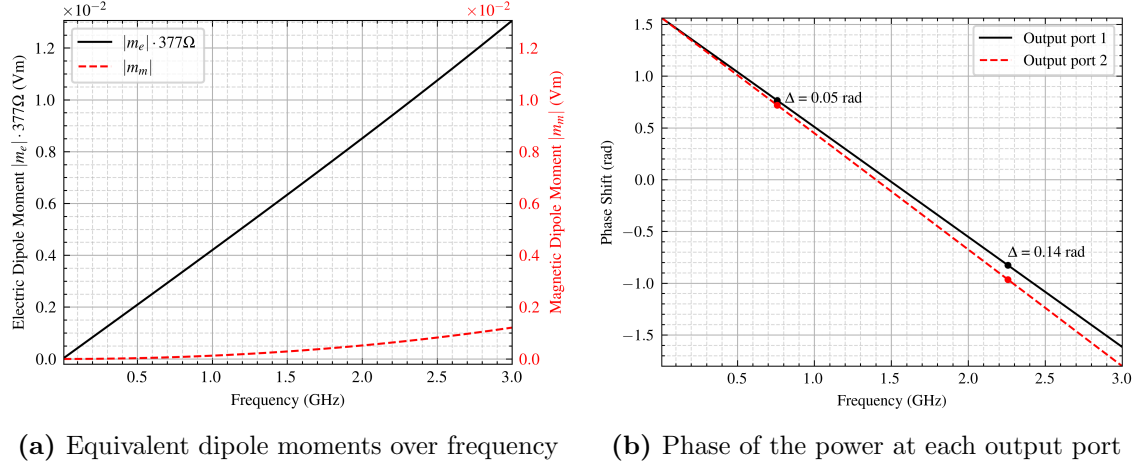
Figure 5.32a demonstrates the effect of the gap height on the dipole moment behavior. As discussed in subsubsection 5.4.1, the reduction of the gap height leads to an increase of both dipole moments,  $\mathbf{m}_e$  and  $\mathbf{m}_m$ . Their magnitudes correlate with the output power, as shown in Figure 5.32b.

An increase in gap height reduces the non-linearities in  $\mathbf{m}_e$  and  $\mathbf{m}_m$ . The voltage drop across the gap and the charge accumulation remains more stable over frequency.

#### 5.4.3 Electrical characteristics

The impedance of the loop antenna with gap is capacitive, shown in Figure 5.33b. The inductance of this antenna is not negligible, opposed to the case of the monopole antenna in subsection 5.2. This causes a significant magnitude of  $\mathbf{m}_m$  in Figure 5.31a and a stronger decline in impedance magnitude of the loop antenna with gap, compared to the monopole antenna's impedance, demonstrated in Figure 5.7b.

The feedpoint voltage decreases more rapidly over frequency compared to that of the monopole antenna, see Figures 5.33a to 5.22a. This behavior is a direct result of increased



(a) Equivalent dipole moments over frequency      (b) Phase of the power at each output port

**Figure 5.31** The equivalent dipole moments of the loop antenna with a gap, where the electric dipole moment  $\mathbf{m}_e$  is weighted with  $Z_0$  to enable comparison with  $\mathbf{m}_m$ . The phases of the powers at output ports 1 and 2 are derived from the S-parameters, as discussed in Section 5.1.6. The analysis specifically focuses on the phase shift between the two ports, which provides information about the presence of  $\mathbf{m}_m$  and  $\mathbf{m}_e$ , as investigated in Section 3.5.2.

induced voltage, which correlates with the pronounced magnetic dipole moment  $\mathbf{m}_m$ , according to Equation 3.50. Furthermore, the feed current increases more slowly, resulting in a slower growth of the electric dipole moment  $\mathbf{m}_e$  with frequency, according to Equation 3.56. The magnitude of  $\mathbf{m}_e$  is additionally smaller than that of the monopole in Figure 5.6.

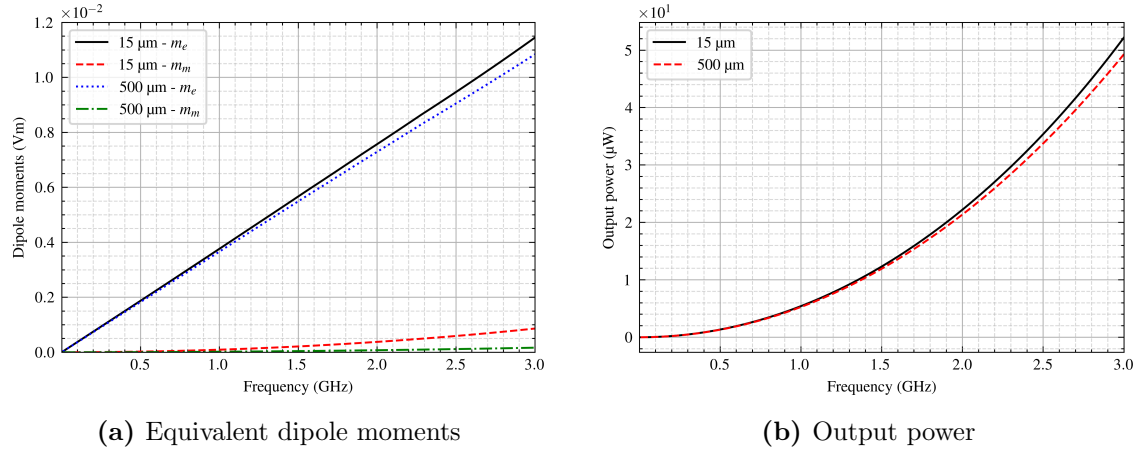


**Figure 5.32** Comparison of dipole moments, where the electric dipole moment  $\mathbf{m}_e$  is weighted with  $\eta_0$  to enable comparison with  $\mathbf{m}_m$ , and output power for different gap heights in the loop antenna.

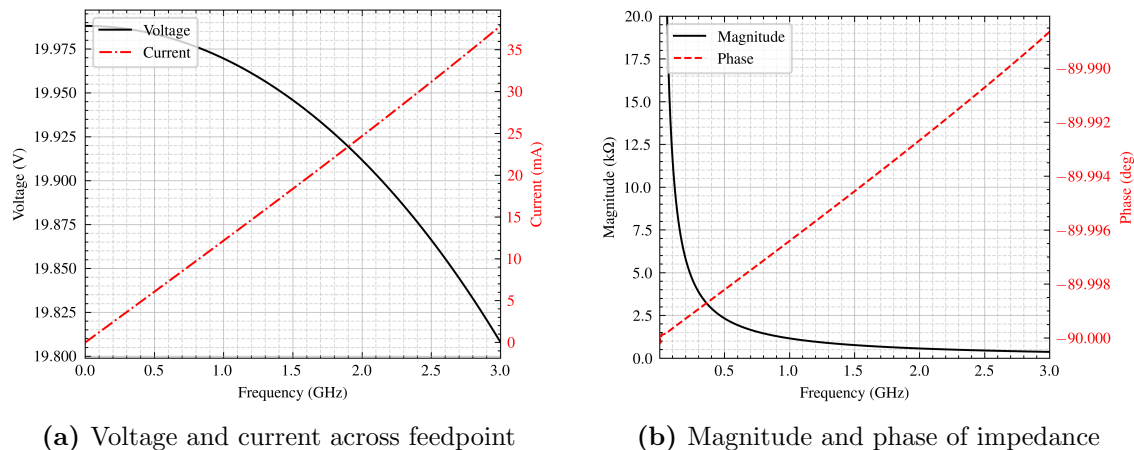


**Figure 5.33** The voltage and current across the feedpoint, together with the related impedance of the loop antenna with gap.

## 5.5 Inverted-F and center-fed monopole antenna

### 5.5.1 Setup and geometrical analysis

The inverted-F antenna (IFA) and center-fed monopole antenna (CFM), shown in Figures 5.34a to 5.34b, are presented here together, because of their related geometry and similar electromagnetic behavior. Both have a maximum dimension of 5 mm, and are electrically small at frequencies up to 6 GHz. They exhibit an inductive nature, hence a similar behavior as the loop antenna in subsection 5.3 is expected. Both antennas consist of a loop of identical area to the loop antenna discussed in Section 5.3, to which a linear arm is connected. In the CFM, this arm is oriented toward the TEM cell septum, whereas in the IFA it is directed toward an output port.

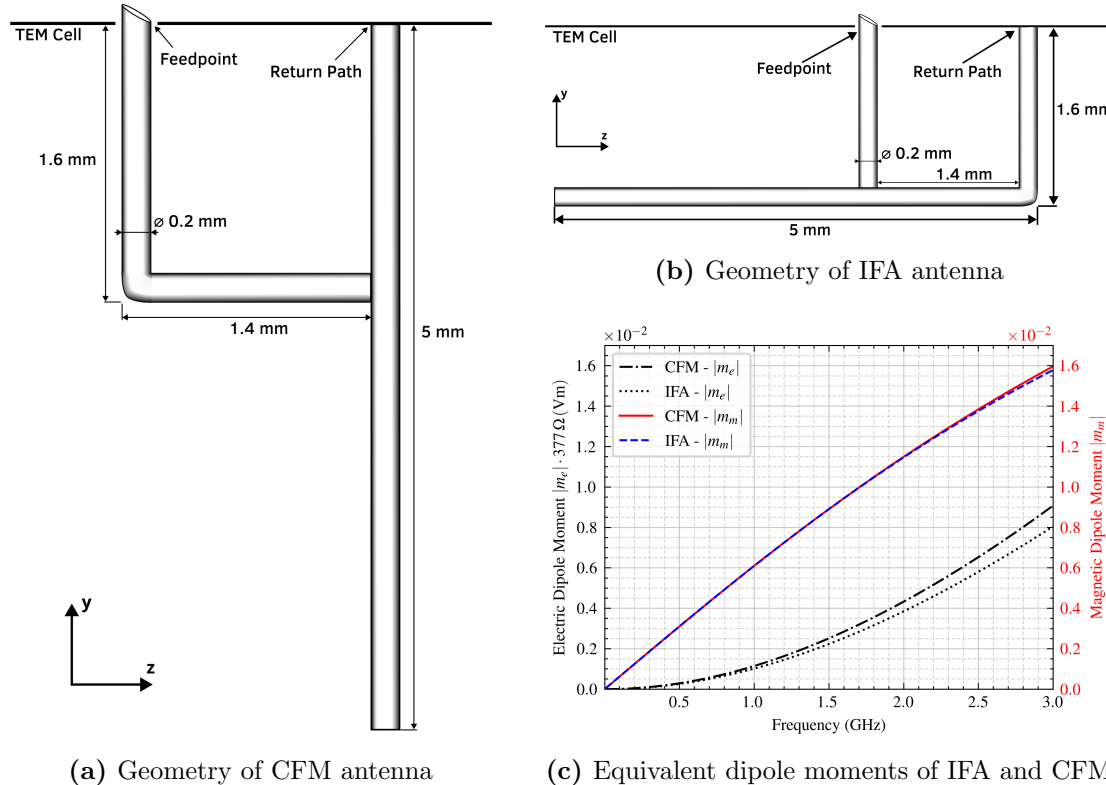


**Figure 5.34** Geometries of IFA and CFM antenna, together with their equivalent dipole moments. the electric dipole moment  $\mathbf{m}_e$  is weighted with the free space impedance  $Z_0$  to enable comparison with the magnetic dipole moment  $\mathbf{m}_m$ .

### 5.5.2 Equivalent dipole moments

The magnetic dipole moments  $\mathbf{m}_m$  of the CFM and IFA presented in Figure 5.34c are comparable to each other, but are smaller in magnitude than that of the loop antenna shown in Figure 5.19a. This reduction can be attributed to the linear arms of the CFM and IFA, which introduce additional capacitance. The increased capacitance enhances the displacement current while reducing the induced voltage. According to Equations (3.50)

to (3.56), this results in a decrease of magnetic dipole moment  $\mathbf{m}_m$  and an increase of the electric dipole moment  $\mathbf{m}_e$ .

Furthermore, for small loop and inductive antennas in general, ?? predicts that an increase in capacitance leads to a stronger non-linear frequency dependence of both  $\mathbf{m}_m$  and  $\mathbf{m}_e$ . This assumption is confirmed by comparing the dipole moments of the loop antenna with those of the CFM and IFA, shown in Figures 5.19a to 5.34c.

## 6 Application of Shielding Techniques in TEM Cells

### 6.1 ASTM ES7-83 method

A numerical model of a TEM cell is employed to determine the shielding effectiveness of barium titanate, ferrite, and silver, following the ASTM ES7-83 method described in Section 3.6.4. The electrical properties of these materials are listed in Table 6.1 and are chosen such that the individual contributions of high conductivity, lossy permeability, and lossy permittivity to the overall shielding performance can be investigated in isolation. Ferrite is additionally modeled with a magnetic loss tangent of  $\tan \delta_m = 0.05$  and barium titanate with an electric loss tangent of  $\tan \delta = 0.0095$ .

The shielding material is modeled as a thin sheet of thickness  $10\ \mu\text{m}$ , positioned at the center of the TEM cell at  $z = 0$ . To reduce computational cost, the sheet is represented using impedance boundary conditions, which are valid and an accurate representation for this material thickness as discussed in Section 5.1.5. The ASTM ES7-83 method requires the definition of a reference power to evaluate the shielding efficiency according to (3.66), which is set to  $P_{\text{ref}} = 1\ \text{W}$ . The transferred power  $P_{\text{load}}$  between the TEM cell ports in the presence of the shielding material is then determined numerically, from which the shielding effectiveness as a function of frequency is computed for each material. The resulting shielding effectiveness are presented against frequency in Figure 6.1.

Material	Rel. permittivity $\epsilon_r$	Rel. permeability $\mu_r$	Conductivity $\sigma$
Ferrite	$\approx 12$	$\approx 1,000$	$0.01\ \text{S/m}$
Barium titanate	$\approx 2,000$	$\approx 1$	$3.64 \cdot 10^{-11}\ \text{S/m}$
Silver	$\approx 1$	$\approx 1$	$6.10 \cdot 10^7\ \text{S/m}$

**Table 6.1** Electromagnetic properties of ferrite, barium titanate, and silver.

Silver, as a highly conductive material, exhibits a large reflection loss  $R_{\text{dB}}$  owing to the significant impedance mismatch between the material and the surrounding air. This mismatch decreases with increasing frequency, as the wave impedance of silver rises with frequency in accordance with (3.60). Simultaneously, the absorption coefficient  $A_{\text{dB}}$  grows with frequency, consistent with the reduction in skin depth at higher frequencies, as discussed in Section 3.6.3. At low frequencies, the multiple-reflection correction term  $B_{\text{dB}}$  is negative and partially offsets the reflection loss, as discussed in Section 3.6.1. As frequency increases, however, the sheet becomes electrically thicker, rendering  $B_{\text{dB}}$  negligible while the absorption term  $A_{\text{dB}}$  increases. Nonetheless, within the frequency range considered,

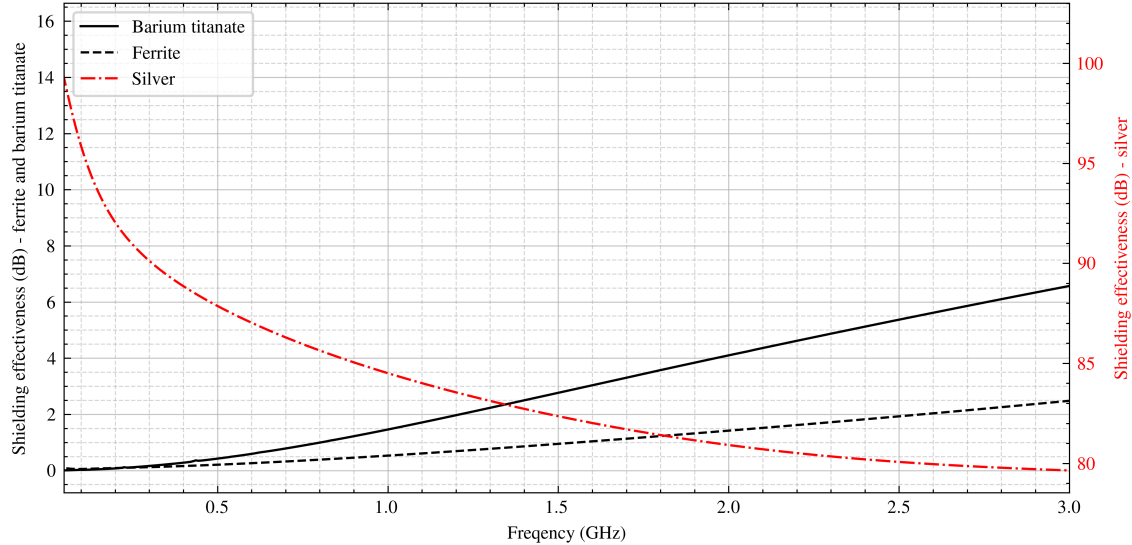


**Figure 6.1** Shielding effectiveness of a thin sheet of ferrite, barium titanate, and silver as a function of frequency, determined using the ASTM ES7-83 method.

the decrease in reflection loss is more pronounced than the increase in absorption, resulting in an overall reduction in shielding effectiveness with frequency.

Ferrite exhibits moderate shielding effectiveness over the investigated frequency range. Its high relative permeability  $\mu_r$  raises the material wave impedance in accordance with (3.60), increasing the impedance mismatch with air and thus the reflection loss  $R_{\text{dB}}$ . At low frequencies, the multiple-reflection correction term  $B_{\text{dB}}$  almost completely compensates the reflection loss. The absorption coefficient  $A_{\text{dB}}$  is limited by its low bulk conductivity  $\sigma$  and magnetic losses parameterized by  $\tan \delta_m$ , so that the shielding performance is primarily governed by reflection.

Barium titanate, with its very high relative permittivity and near-unity permeability, exhibits a comparatively low wave impedance and therefore a high reflection loss  $R_{\text{dB}}$ . Its negligible conductivity results in minimal absorption at low frequencies, while the multiple-reflection correction term  $B_{\text{dB}}$  almost completely compensates the reflection loss. As frequency increases, the growing electrical thickness of the sheet reduces the negative contribution of the multiple-reflections term  $B_{\text{dB}}$  while the dielectric loss tangent  $\tan \delta$  gives rise to an increasing absorption contribution  $A_{\text{dB}}$ , leading to a gradual improvement in shielding effectiveness with frequency.

## 6.2 Dual TEM cell

A simulation model of two coupled TEM cells, as shown in Figure 3.14, is constructed based on the individual cell model presented in Section 5.1.2. The aperture separating the two cells is modeled as an empty square opening with a side length of  $d = 10$  mm, ensuring that it remains electrically small up to a frequency of approximately 3 GHz. To achieve accurate results, sufficient mesh resolution in the aperture region is critical, as highlighted in Section 5.1.4. Accordingly, 10 to 15 mesh elements across the aperture

width are maintained throughout all simulations. Following the procedure outlined in Section 3.6.5, the electric and magnetic shielding effectiveness of ferrite, barium titanate, and silver are derived.

Port 1 excites the TEM cell with a constant input power of 1 W. The sum  $P_{\text{sum}}$  and difference  $P_{\text{diff}}$  of the powers received at ports 3 and 4 are then computed following [32] as

$$P_{\text{sum}} = (a + b)(a + b)^*, \quad (6.1a)$$

$$P_{\text{diff}} = (a - b)(a - b)^*, \quad (6.1b)$$

where  $a$  and  $b$  are the complex field amplitudes at ports 3 and 4, respectively. Evaluated for an empty aperture, these quantities serve as the reference values  $P_{\text{ref,sum}}$  and  $P_{\text{ref,diff}}$  required to compute the electric and magnetic shielding effectiveness according to (3.68a) and (3.68b). They are shown against frequency in Figure 6.2.

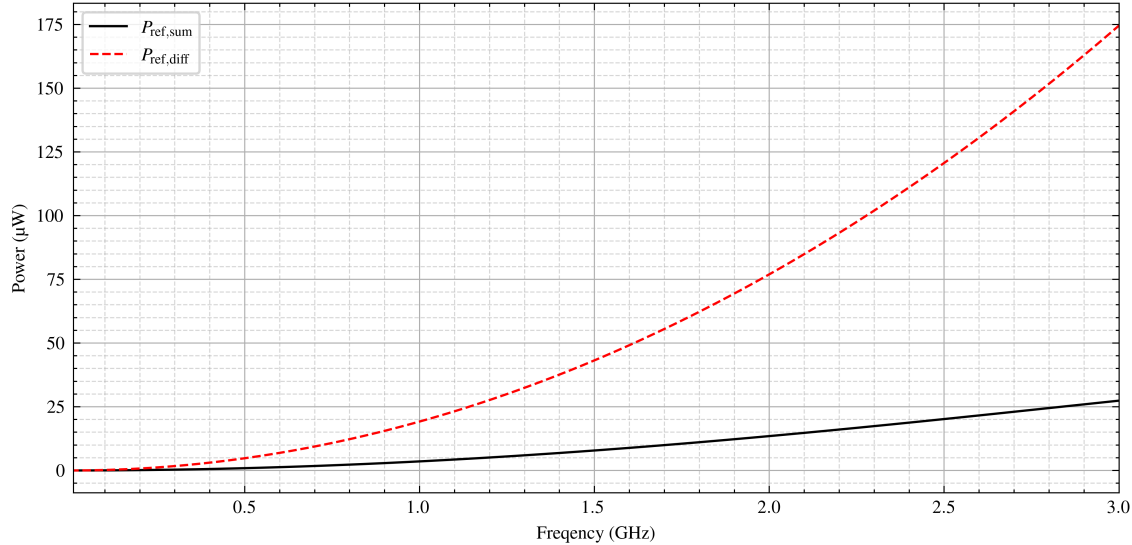


**Figure 6.2** The sum  $P_{\text{ref,sum}}$  and difference  $P_{\text{ref,diff}}$  of the reference power, measured with an empty aperture and calculated with phase information considered.

The aperture is then filled with each shielding material under investigation in turn, with a material thickness of  $t = 10 \mu\text{m}$ . The sum  $P_{\text{load,sum}}$  and difference  $P_{\text{load,diff}}$  of the powers at ports 3 and 4 are computed and used as the load power to derive the electric and magnetic shielding effectiveness of each material according to (3.68a) and (3.68b). The derived powers for all investigated materials are shown against frequency in Figures 6.3a and 6.3b.

The distinction between electric and magnetic shielding effectiveness is particularly significant in the near-field regime, where the wave impedance of the source field deviates substantially from the free-space impedance  $\eta_0$ . Electric near-field sources produce high-impedance fields, whereas magnetic near-field sources produce low-impedance fields, as mentioned in Section 3.6.1. The shielding performance of a material depends not only on its electric properties but also on the degree of impedance mismatch between the material and the incident near-field, as expressed by (3.59).

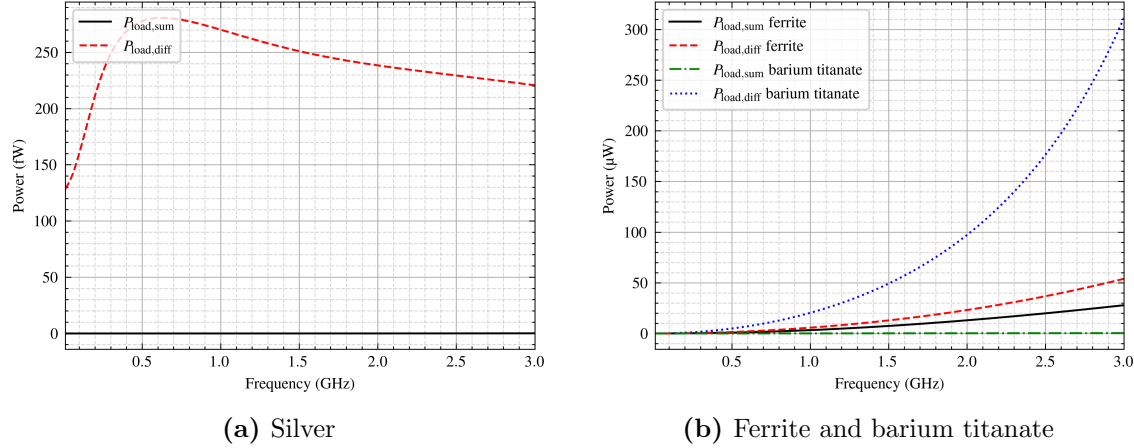


**Figure 6.3** The sum  $P_{\text{load,sum}}$  and difference  $P_{\text{load,diff}}$  of the output power measured at ports 3 and 4 with phase information considered.

Ferrite exhibits higher power transfer than barium titanate, indicating lower overall shielding effectiveness. For both materials, the power transfer increases with frequency, which can be attributed to their low bulk conductivity. Silver, by contrast, exhibits power transfer several orders of magnitude lower and is therefore presented in a separate plot for clarity. The resulting electric and magnetic shielding effectiveness spectra are shown in Figure 6.4.

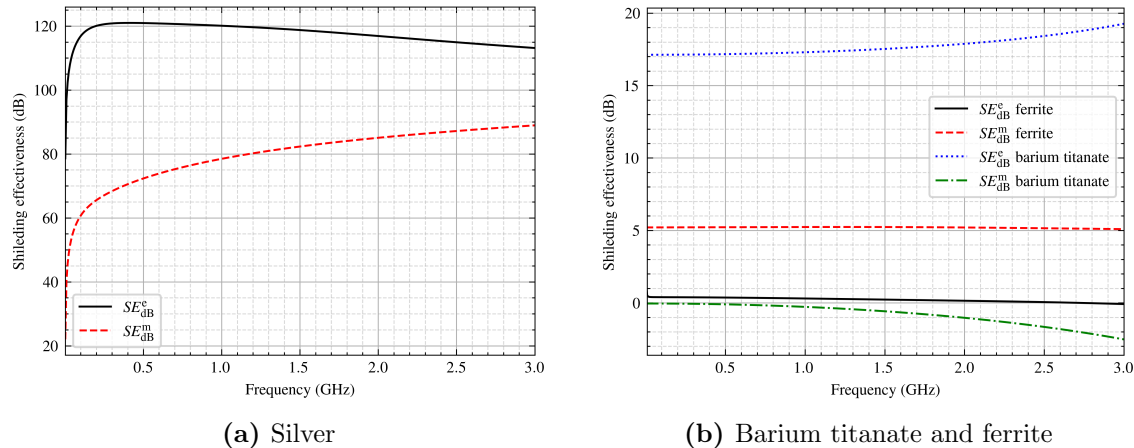


**Figure 6.4** Electric  $SE_{dB}^e$  and magnetic  $SE_{dB}^m$  shielding effectiveness of (a) silver and (b) barium titanate and ferrite, derived according to (3.68a) and (3.68b).

Barium titanate exhibits good electric shielding characteristics but a negative  $SE_{dB}^m$ , indicating poor magnetic shielding. Negative magnetic shielding effectiveness values are physically possible and arise from interference effects at the loaded aperture, which cause the field amplitude  $a$  and the received power at port 3 to increase [38, 16, p. 63]. The high relative permittivity of barium titanate lowers its material wave impedance (see (3.60)), increasing the impedance mismatch with high-impedance electric source fields

and thereby yielding a high electric shielding effectiveness. Conversely, this low material wave impedance reduces the mismatch with low-impedance magnetic near-field sources, which accounts for the poor and eventually negative magnetic shielding effectiveness with increasing frequency.

Ferrite, on the other hand, demonstrates a higher magnetic shielding effectiveness  $SE_{\text{dB}}^m$  but a low or negative electric shielding effectiveness  $SE_{\text{dB}}^e$ . Its high relative permeability raises the material wave impedance (see (3.60)), enhancing reflections of incident magnetic near-fields whose low wave impedance results in a large mismatch at the material surface. However, this elevated material wave impedance reduces the mismatch with high-impedance electric source fields, rendering ferrite a poor electric shield.

Silver demonstrates the highest overall shielding effectiveness among the materials investigated. Its high conductivity produces a very low material wave impedance, which leads to a strong impedance mismatch with electric near-field sources, as discussed in Section 6.1. At low frequencies, the magnetic shielding effectiveness increases monotonically across the inspected frequency range, driven by the growing absorption contribution as the skin depth decreases steeply (see (3.63)). The electric shielding effectiveness, by contrast, begins to decline at higher frequencies, as the wave impedance of the material surface increases toward that of the high-impedance electric source field, reducing the impedance mismatch and the associated reflection loss  $R_{\text{dB}}$  in accordance with (3.59).

### 6.3 Antennas in shield enclosure

Following the near-field shielding investigations, the loop and monopole antennas from Sections 5.2 and 5.3 placed inside a hollow cubic enclosure are examined, as shown in Figures 6.5a and 6.5b. The enclosure has a wall thickness of 10  $\mu\text{m}$  and a side length of 6 mm.

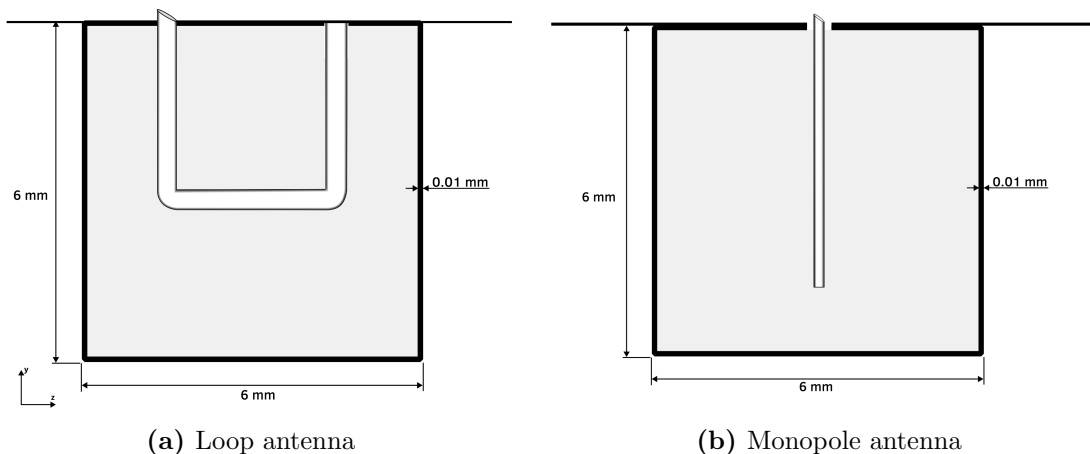


**Figure 6.5** Investigated antennas placed inside a hollow cubic enclosure within the TEM cell.

Figure 6.6a shows the radiated power from the antennas with and without a barium titanate enclosure. The output power of the loop antenna increases because the barium

titanate enclosure capacitively loads the antenna, resulting in a reduction of the resonance frequency. This effect shifts the antenna toward a more efficient operating point within the investigated frequency range, as discussed in Section 5.3. In contrast, the enclosure effectively shields the radiation of the monopole antenna. These results are consistent with the near-field of the monopole antenna being predominantly electric, as given in (2.11), while that of the loop antenna is predominantly magnetic, as given in (2.19), and are in agreement with the near-field shielding investigations presented in Section 6.2.

Figure 6.6b shows the corresponding radiated power for the ferrite enclosure. Here, the roles of the two antennas are reversed. The output power of the monopole antenna increases due to the ferrite enclosure inductively loading the antenna, while the loop antenna's radiation is attenuated.

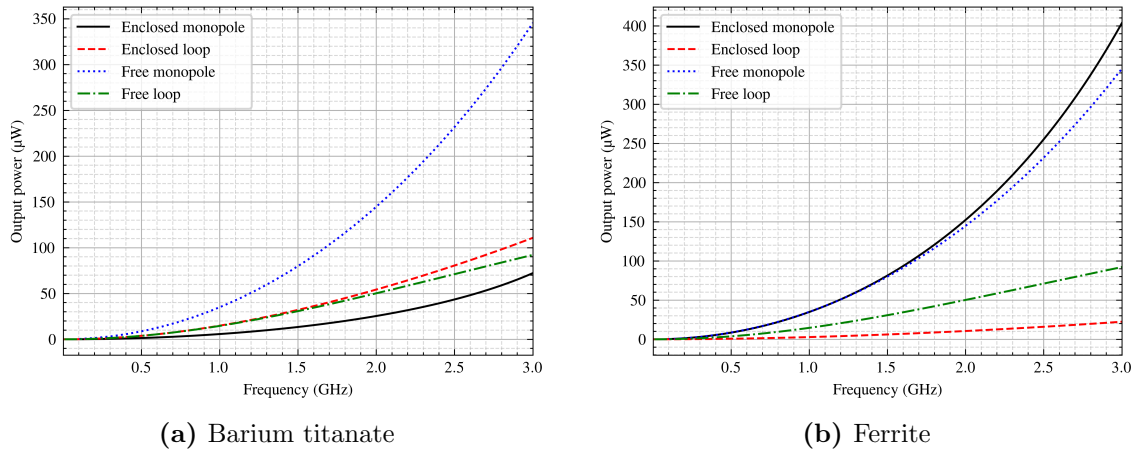


**Figure 6.6** Radiated power as a function of frequency for the loop and monopole antennas with and without enclosure.

The influence of enclosure wall thickness on the radiated power is examined in Figure 6.7, where silver is now additionally included as a shielding material. As expected, increasing the wall thickness reinforces the shielding effects observed in Figure 6.6. Silver yields the lowest power transfer among all investigated materials, consistent with the high shielding effectiveness found and discussed in Sections 6.1 and 6.2. The output power of the monopole antenna within the silver enclosure increases with frequency, which is associated with the declining electric shielding effectiveness at higher frequencies. Conversely, the loop antenna produces less output power with increasing frequency, consistent with the monotonically increasing magnetic shielding effectiveness of silver.

Additionally, resonances are observed for thick enclosures, manifesting as a pronounced peak in the transmitted power at approximately 2.5 GHz for the barium titanate enclosure with a wall thickness of 100  $\mu\text{m}$ . A similar trend is observed for the thickest ferrite enclosure, where the resonance frequency lies just outside the investigated frequency range. As shown in Figure 6.8, this effect corresponds to a half-wavelength resonance established within the enclosure cavity. The excitation of such resonant waves requires, among other things, that internal reflections are not fully suppressed. This proposition in turn demands that the multiple-reflection correction term  $B_{\text{dB}}$  remains sufficiently small in magnitude,

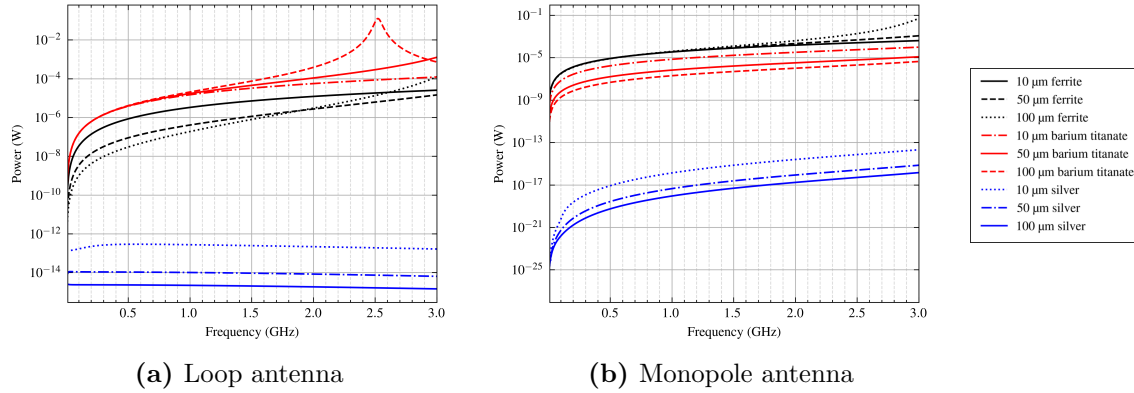


**Figure 6.7** Radiated power as a function of frequency for the loop and monopole antennas with varying enclosure wall thickness.

as discussed in Section 3.6.1. A larger wall thickness supports this condition by increasing the electrical thickness of the enclosure walls.

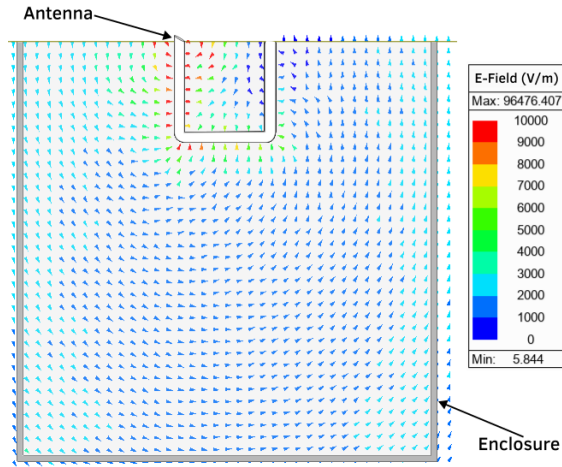


**Figure 6.8** Electric near-field distribution of the loop antenna at the resonance frequency of 2.5 GHz, with a barium titanate shielding enclosure of 100  $\mu\text{m}$  wall thickness.

## 6.4 Dipole moments in shield enclosure

Replacing electrically small antennas with equivalent dipole moments inside shielding enclosures enables investigation of shielding performance with reduced computational effort. For this purpose, the equivalent dipole moments of the monopole and loop antennas derived in Sections 5.2.2 and 5.3.2 are used in place of the full antenna models within the enclosures depicted in Figure 6.5. The radiated power produced by these dipole moments for different enclosure materials at a constant material thickness of  $10\text{ }\mu\text{m}$  is shown in Figure 6.9.

The dipole approximation agrees well with the full antenna model for the loop antenna in barium titanate and for the monopole antenna in ferrite. As the shielding effectiveness of

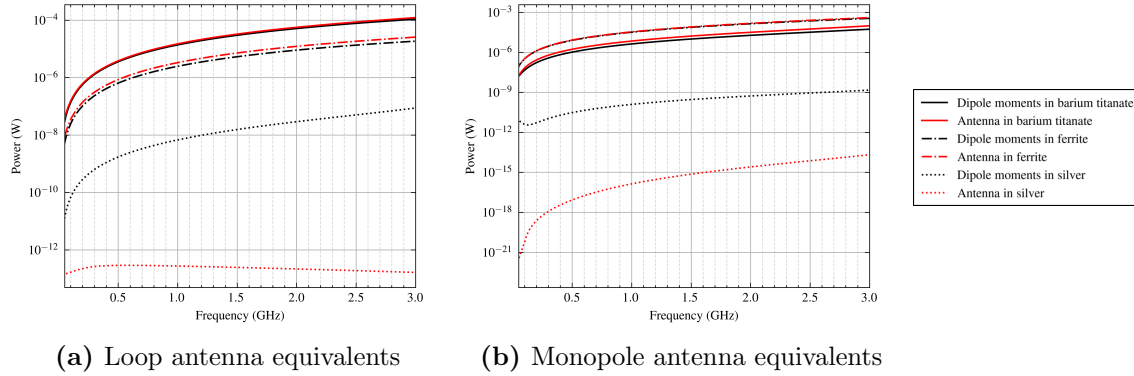


**Figure 6.9** Radiated power as a function of frequency for the loop and monopole antenna equivalent dipole moments in enclosures of different materials at a constant wall thickness of 10 µm.

the enclosure material increases relative to the respective antenna, however, the accuracy of the approximation decreases, indicating that the equivalent dipole moments must be adjusted accordingly to account for the interaction between the source and the enclosure.

## 7 Conclusion

This thesis presents investigations of electrically small antennas and their coupling with a TEM cell using the finite element method. It further discusses applications of the framework created.

In this thesis, dipole moments equivalent to the electrically small antennas are calculated, whose magnitudes directly correlate with the electric and magnetic coupling of the antenna with the TEM cell. It finds, that the electric dipole moment correlates directly to the displacement current towards the septum, and the magnetic dipole moment to the voltage induced on the septum. An equivalent circuit model, both for capacitive and inductive antennas coupling to the TEM cell, is developed.

The relation of different geometrical and electrical antenna parameters to the equivalent dipole moments is investigated. An increase in Q-factor or decrease in resonance frequency of the antenna has been found to increase non-linear dipole moments frequency-behavior. The electric dipole moment generated by an antenna increases primarily with its physical height, due to increased displacement currents toward the septum. The magnetic dipole moment increases with the loop area normal to the magnetic field intensity of a propagating mode in the TEM cell. If the loop is not closed, a magnetic dipole moment can still exist due to curling electric field intensities  $\nabla \times \mathbf{E} \neq 0$  forming perpendicular to the magnetic field intensity.

Further research could involve the measurement of such antennas with a real TEM cell, or the numerical analysis with other waveguides, such as the IC stripline. The framework in this thesis could be used to increase EMC of electronic systems containing electrically small, radiating structures, or represent them with dipole moments for less computational effort in complex simulation models.

## References

- [1] George B. Arfken, Hans-Jurgen Weber, and Frank Harris. *Mathematical methods for physicists*. Academic, 2013.
- [2] Constantine A. Balanis. *Advanced Engineering Electromagnetics*. John Wiley Sons, 2012.
- [3] Constantine A. Balanis. *Antenna theory: Analysis and design*. Buch Constantine A. Balanis. 3rd. Wiley, 1997.
- [4] C. Buccella et al. “Magnetic field computation in a physically large domain with thin metallic shields”. In: *IEEE Transactions on Magnetics* 41.5 (2005), pp. 1708–1711. DOI: 10.1109/TMAG.2005.846059.
- [5] Z. Cendes and D. Shenton. “Adaptive mesh refinement in the finite element computation of magnetic fields”. In: *IEEE Transactions on Magnetics* 21.5 (1985), pp. 1811–1816. DOI: 10.1109/TMAG.1985.1063929.
- [6] Z.J. Cendes. “Vector finite elements for electromagnetic field computation”. In: *IEEE Transactions on Magnetics* 27.5 (1991), 3958–3966. DOI: 10.1109/20.104970.
- [7] Z.J. Cendes and J.-F. Lee. “The transfinite element method for modeling MMIC devices”. In: 1988., *IEEE MTT-S International Microwave Symposium Digest* (1988), 623–626. DOI: 10.1109/mwsym.1988.22111.
- [8] Robert E. Collin. *Field theory of guided waves*. IEEE Press, 2015.
- [9] Saju Daniel and Sabu Thomas. “Shielding Efficiency Measuring Methods and Systems”. In: *Advanced Materials for Electromagnetic Shielding: Fundamentals, Properties, and Applications*. 2019, pp. 61–87. DOI: 10.1002/9781119128625.ch4.
- [10] Alexander V. Demakov and Maxim E. Komnatnov. “TEM cell for Testing Low-profile Integrated Circuits for EMC”. In: *2020 21st International Conference of Young Specialists on Micro/Nanotechnologies and Electron Devices (EDM)*. 2020, pp. 154–158. DOI: 10.1109/EDM49804.2020.9153508.
- [11] David J. Griffiths. *Introduction to electrodynamics*. Cambridge University Press, 2024.
- [12] C. Groh et al. “TEM waveguides for EMC measurements”. In: *IEEE Transactions on Electromagnetic Compatibility* 41.4 (1999), pp. 440–445. DOI: 10.1109/15.809846.
- [13] Robert C. Hansen and Robert E. Collin. *Small antenna handbook*. Wiley, 2013.
- [14] K.H. Huebner et al. *The Finite Element Method for Engineers*. A Wiley-Interscience publication. Wiley, 2001. ISBN: 9780471370789. URL: <https://books.google.at/books?id=f3MZE1BYq3AC>.
- [15] John David Jackson. *Classical Electromagnetism*. 2nd ed. Wiley.
- [16] Maciej Wladyslaw Jaroszewski, Sabu Thomas, and Ajay V. Rane. *Advanced materials for electromagnetic shielding: Fundamentals, properties, and applications*. Wiley, 2019.
- [17] J.P. Karst, C. Groh, and H. Garbe. “Calculable field generation using TEM cells applied to the calibration of a novel E-field probe”. In: *IEEE Transactions on Electromagnetic Compatibility* 44.1 (2002), pp. 59–71. DOI: 10.1109/15.990711.
- [18] M. Koch, C. Groh, and H. Garbe. “Exact Determination of Resonant Frequencies in TEM Cells”. In: *13th International Zurich Symposium and Technical Exhibition on Electromagnetic Compatibility*. 1999, pp. 653–658. DOI: 10.23919/EMC.1999.10791592.

- [19] Galen H Koepke. "Theory and measurements of radiated emissions using a TEM cell". In: (1989). DOI: 10.6028/nist.tn.1326.
- [20] Dominik Kreindl et al. "A Simulation Workflow for Predicting IC Stripline Radiated Emissions of Bond Wire-Based Systems". In: *2024 14th International Workshop on the Electromagnetic Compatibility of Integrated Circuits (EMC Compo)*. 2024, pp. 69–73. DOI: 10.1109/EMCCompo61192.2024.10742020.
- [21] Dominik Kreindl et al. "Evaluation of an analytical equivalent Hertzian dipole representation in tem cells applying the finite element method". In: *IEEE Transactions on Magnetics* 60.3 (2024), 1–4. DOI: 10.1109/tmag.2023.3324698.
- [22] Dominik Kreindl et al. "Measurement and Simulation Methodology for Characterizing the Shielding Effectiveness of Coating Materials for Optical Sensors". In: *2023 International Symposium on Electromagnetic Compatibility – EMC Europe*. 2023, pp. 1–6. DOI: 10.1109/EMCEurope57790.2023.10274360.
- [23] Ján Kruželák et al. In: *Electrical conductivity, EMI absorption shielding performance, curing process and mechanical properties of rubber composites* (2024). DOI: 10.20944/preprints202401.1547.v1.
- [24] J.-F. Lee, D.-K. Sun, and Z.J. Cendes. "Full-wave analysis of dielectric waveguides using tangential vector finite elements". In: *IEEE Transactions on Microwave Theory and Techniques* 39.8 (1991), pp. 1262–1271. DOI: 10.1109/22.85399.
- [25] J.F. Lee, D.K. Sun, and Z.J. Cendes. "Tangential vector finite elements for electromagnetic field computation". In: *IEEE Transactions on Magnetics* 27.5 (1991), pp. 4032–4035. DOI: 10.1109/20.104986.
- [26] M.F.N. Mohsen. "Some details of the Galerkin Finite Element Method". In: *Applied Mathematical Modelling* 6.3 (1982), 165–170. DOI: 10.1016/0307-904x(82)90005-1.
- [27] Cristian MORARI and Cristian BĂLAN. In: *Methods for determining shielding effectiveness of materials* (2015).
- [28] H. Taconi D. Gravino N. Disages K. Mojail H.R. Mira and P.K. Nestaris. "Understanding Capacitance and Inductance in Antennas". In: *National Journal of Antennas and Propagation* 4.2 (2022). DOI: 10.31838/njap/04.02.07.
- [29] Clayton R. Paul, Robert C. Scully, and Mark A. Steffka. *Introduction to electromagnetic compatibility*. Wiley, 2023.
- [30] S. A. Schelkunoff. "The impedance concept and its application to problems of reflection, refraction, shielding and power absorption". In: *Bell System Technical Journal* 17.1 (1938), 17–48. DOI: 10.1002/j.1538-7305.1938.tb00774.x.
- [31] D. Shenton and Z. Cendes. "Three-dimensional finite element mesh generation using Delaunay tessellation". In: *IEEE Transactions on Magnetics* 21.6 (1985), 2535–2538. DOI: 10.1109/tmag.1985.1064165.
- [32] Ippalapalli Sreenivasiah, David Chang, and Mark Ma. "Emission characteristics of electrically small radiating sources from tests inside a tem cell". In: *IEEE Transactions on Electromagnetic Compatibility* EMC-23.3 (1981), 113–121. DOI: 10.1109/temc.1981.303930.
- [33] GILBERT STRANG. *Analysis of the finite element method*. WELLESLEY-CAMBRIDGE Press, 2018.

- [34] John C Tippet, David C Chang, and Myron L Crawford. In: *An analytical and experimental determination of the cutoff frequencies of higher-order te modes in a Tem cell* (1976). DOI: 10.6028/nbs.ir.76-841.
- [35] C.M. Weil and L. Gruner. “High-order mode cutoff in rectangular striplines (short papers)”. In: *IEEE Transactions on Microwave Theory and Techniques* 32.6 (1984), 638–641. DOI: 10.1109/tmtt.1984.1132745.
- [36] Perry F Wilson. “Excitation of a tem cell by a vertical electric Hertzian dipole”. In: (1981). DOI: 10.6028/nbs.tn.1037.
- [37] Perry F. Wilson, David C. Chang, and Mark T. Ma. “Input Impedance of a Probe Antenna in a TEM Cell”. In: *IEEE Transactions on Electromagnetic Compatibility* EMC-26.4 (1984), pp. 154–161. DOI: 10.1109/TEMC.1984.304216.
- [38] Perry F. Wilson and Mark T. Ma. “Shielding-Effectiveness Measurements with a Dual TEM Cell”. In: *IEEE Transactions on Electromagnetic Compatibility* EMC-27.3 (1985), pp. 137–142. DOI: 10.1109/TEMC.1985.304277.
- [39] Perry F. Wilson and Mark T. Ma. “Simple approximate expressions for higher order mode cutoff and resonant frequencies in TEM cells”. In: *IEEE Transactions on Electromagnetic Compatibility* 28.3 (1986), 125–130. DOI: 10.1109/temc.1986.4307269.